The Sikkim flood of October 2023: Drivers, causes and impacts of a multihazard cascade

Ashim Sattar, Kristen Cook, Shashi Kant Rai, Etienne Berthier, Simon Allen, Sonam Rinzin, Maximillian van Wyk de Vries, Wilfried Haeberli, Pradeep Kushwaha, Dan Shugar, et al.

The Sikkim flood of October 2023: drivers, causes and impacts of a multi-hazard cascade

Ashim Sattar*[1], Kristen L. Cook[2,3], Shashi Kant Rai[4], Etienne Berthier[5], Simon Allen[6,7], Sonam Rinzin[8], Maximillian Van Wyk De Vries[9,10], Wilfried Haeberli[6], Pradeep Kushwaha[11], Dan H. Shugar[12], Adam Emmer[13], Umesh K. Haritashya[14,15], Holger Frey[6], Praful Rao[16], Kori Sanjay Kumar[17,18], Prabhakar Rai[19], Rajeev Rajak[20], Faruk Hossain[21], Christian Huggel[6], Martin Mergili[13], Mohd. Farooq Azam[22], Simon Gascoin[23], Jonathan L. Carrivick[24], Louie Elliot Bell[25], Rakesh Kumar Ranjan[20], Irfan Rashid[26], Anil. V. Kulkarni[27], Dave Petley[28], Wolfgang Schwanghart[29], C. Scott Watson[30], Nazimul Islam[31], Moushumi Das Gupta[32], Stuart N. Lane[31], Shahid Younis Bhat[26]

Affiliations:

[1]School of Earth, Ocean and Climate Sciences, Indian Institute of Technology Bhubaneswar, Odisha, India
[2]Institut de Recherche pour le Développement, University Grenoble Alpes, Grenoble, France
[3]Institut des Sciences de la Terre, University Grenoble Alpes, Grenoble, France
[4]Department of Environmental Sciences, Central University of Jammu, Jammu, Jammu and Kashmir, India
[5]Université de Toulouse, LEGOS (CNES/CNRS/IRD/UT3), Toulouse, France
[6]Department of Geography, University of Zurich, Zurich, Switzerland
[7]Institute of Environmental Sciences, University of Geneva, Geneva, Switzerland
[8]School of Geography, Politics, and Sociology, Newcastle University, Newcastle, UK
[9]Department of Geography, University of Cambridge, Cambridge, UK
[10]Department of Earth Sciences, University of Cambridge, Cambridge, UK
[11]Centre for Atmospheric and Oceanic Sciences, Indian Institute of Science, Bangalore, India.
[12]Water, Sediment, Hazards, and Earth-surface Dynamics (waterSHED) Laboratory, Department of Earth, Energy, and Environment, University of Calgary, Calgary, Alberta, Canada
[13]Institute of Geography and Regional Science, University of Graz, Graz, Austria
[14]Department of Geology and Environmental Geosciences, University of Dayton, Dayton, OH, USA
[15]Sustainability Program, University of Dayton, Dayton, OH, USA
[16]Save The Hills, NGO, Kalimpong, West Bengal, India
[17] Indo-Tibet Border Police, Ministry of Home Affairs, Government of India
[18] Department of Psychology, Banaras Hindu University (BHU), Varanasi, India
[19]Sikkim State Disaster Management Authority, Government of Sikkim, Sikkim, India
[20]Department of Geology, Sikkim University, Gangtok, Sikkim, India
[21]Geological Survey of Bangladesh, Segunbagicha, Dhaka, Bangladesh
[22]Department of Civil Engineering, Indian Institute of Technology Indore, Indore, India
[23]Centre d'Etudes Spatiales de la Biosphère (CESBIO), CNES/CNRS/INRAE/IRD/UT3-Paul Sabatier, Toulouse, France.
[24]School of Geography and water@leeds, University of Leeds, Leeds, UK
[25]Scott Polar Research Institute, University of Cambridge, Cambridge, UK
[26]Department of Geoinformatics, University of Kashmir, Srinagar, India
[27]DST Centre for Excellence in Climate Change, Divecha Centre for Climate Change, IISc, Bangalore, India

[28]School of Environmental Sciences, University of Hull, Hull, UK
[29]Institute of Environmental Science and Geography, University of Potsdam, Potsdam-Golm, Germany
[30]COMET, School of Earth and Environment, University of Leeds, Leeds, UK
[31]Institute of Earth Surface Dynamics (IDYST), University of Lausanne, Switzerland
[32] Journalist, The Print, New Delhi, India

*Corresponding author. Email: ashim.sattar@gmail.com; ashimsattar@iitbbs.ac.in

Abstract: On 3 October 2023, a multi-hazard cascade in the Sikkim Himalaya, India, was triggered by 14.7 million m^3 of frozen lateral moraine collapsing into South Lhonak Lake, generating ~20 m a tsunami-like impact wave, breaching the moraine, and draining ~50 million m^3 of water. The ensuing Glacial Lake Outburst Flood (GLOF) eroded ~270 million m^3 of sediment, which overwhelmed infrastructure, including hydropower installations along the Teesta River. The physical scale and human and economic impact of this event prompts urgent reflection on the role of climate change and human activities in exacerbating such disasters. Insights into multi-hazard evolution are pivotal for informing policy development, enhancing Early Warning Systems (EWS), and spurring paradigm shifts in GLOF risk management strategies in the Himalaya and other mountain environments.

Main Text: Catastrophic water release from glacial lakes can cause far-reaching Glacial Lake Outburst Floods (GLOF), with impact up to hundreds of kilometers downstream (*1–5*). GLOFs often involve complex, cascading multi-hazard processes [c.f. (*6*)] and are particularly evident in steep mountainous regions like the Himalaya. These impacts and reach may be further extended by interaction with entrained and relocated deposits, leading to debris flows and debris floods (*7–11*).

South Lhonak Lake (SLL) in Sikkim, India is located at 5200 m above sea level (asl) in the Upper Teesta basin. It is one of the largest, fastest-growing, and most hazardous lakes in Sikkim with potential to cause significant downstream damage in the event of a GLOF (*12–17*). On 3 October 2023, SLL experienced an outburst, triggering a devastating flood cascade that killed 55 people, left 74 missing (*18*), and destroyed the 1200-megawatt (MW) Teesta-III hydropower dam. The flood cascade (3-4 October) impacted Sikkim, West Bengal, and had transboundary implications in Bangladesh (Fig. 1A).

This paper presents a collaborative effort involving scientists, non-governmental organizations, and diverse stakeholders to investigate the SLL GLOF and the subsequent multi-hazard cascade. Our motivation is not only to understand this event but also to identify major findings of wider relevance given rapid climate warming in mountain regions worldwide. We analyze the drivers, causes, and downstream impacts of the hazard cascade using high-resolution satellite imagery, seismic data, meteorological data, field observations, and numerical modeling. We explore the triggers of the GLOF, prevailing meteorological conditions, long-term climatological influences, glacier mass balance, permafrost conditions, and reconstruct the hydraulic dynamics of the GLOF. Downstream implications are evaluated from the GLOF source to the confluence of Teesta and Brahmaputra rivers in Bangladesh at 385 km downstream, including (i) mapping of damaged infrastructure (buildings, roads, bridges, and hydropower plants) and agricultural land; (ii) erosion and deposition by the flood; (iii) impact of secondary triggered landslides; and (iv) transboundary impacts. Finally, we evaluate the long-term impact of the event on future hazards within the Teesta River system. The assessment indicates that the high hazard level arises not only from the flood itself but also from the series of subsequent processes it triggers. The hazard increases the vulnerability of Teesta valley to

future events. Understanding these cascading and enduring effects is essential for developing effective strategies to manage GLOF risks in the Himalaya and similar mountainous regions worldwide.

The Himalaya contains more than 2,400 lakes larger than 0.1 km^2, and many of these are growing rapidly (*19*). The rivers draining High Mountain Asia also have a hydropower potential of 500 gigawatts (*20*), 80% of which remains untapped (*21*). Increasing demands for stable and renewable energy have driven a surge in hydropower development with >650 projects planned or under construction in High Mountain Asia (*20*). However, these hydropower installations are susceptible to a wide range of hazards, including GLOFs and their associated multi-hazard chain (e.g. (*20*, *22–26*). Recent disasters include the 2016 Gongbatongsha/Upper Bhotekoshi GLOF in Nepal (*9*), and the 2021 Chamoli rock-ice avalanche in India (*27*), both of which destroyed hydropower plants. Through our analysis of this flood disaster, we aim to identify key insights to reduce risks and enhance multi-hazard management strategies for GLOFs across High Mountain Asia and similar regions around the world.

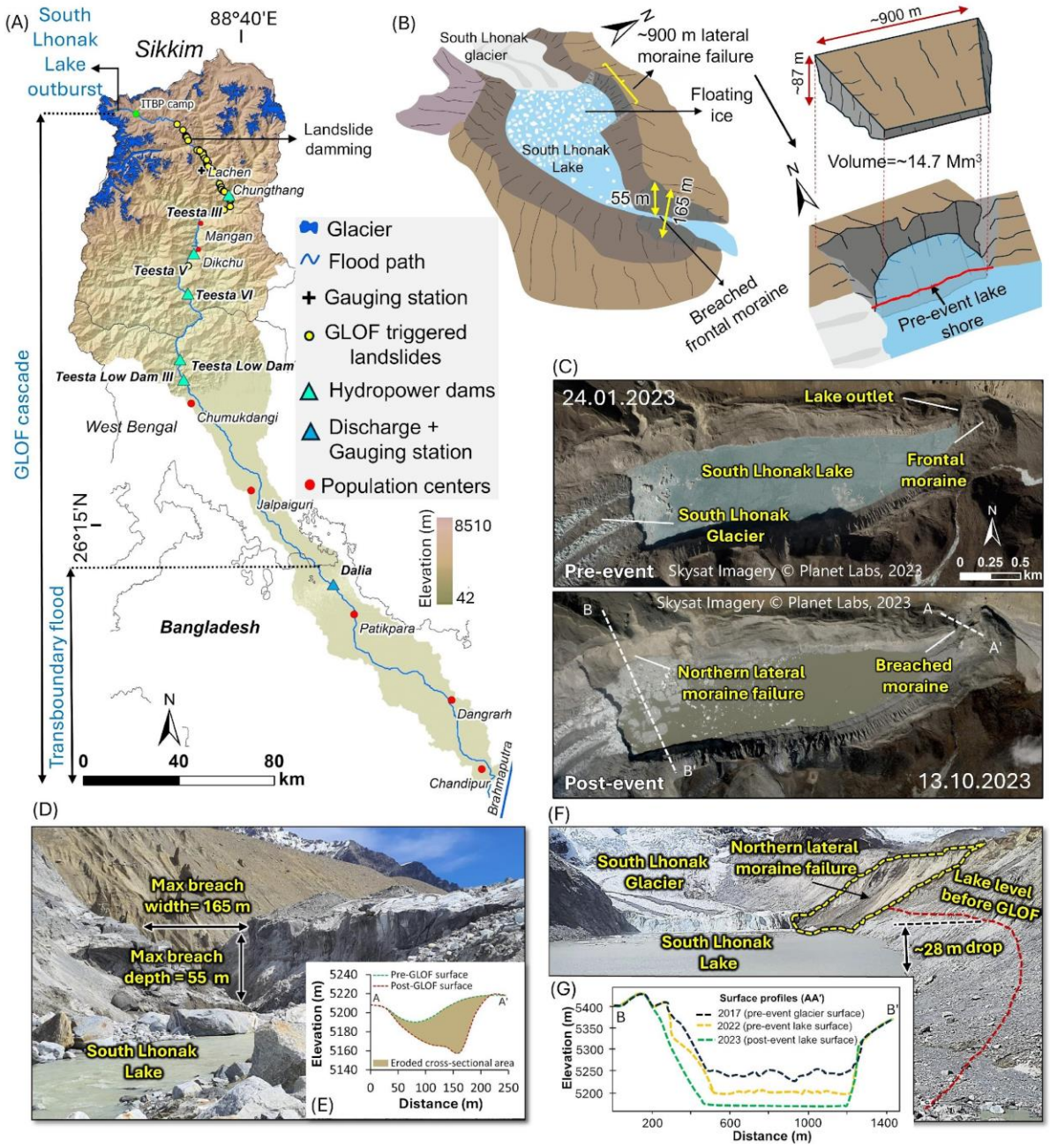

Fig. 1. Overview of the 3-4 October 2023 GLOF cascade from South Lhonak Lake (SLL). (A) Flood-impacted stretch of the Teesta River showing the location of SLL (27°54′20″N and 88°10′20″E) and the dominant flood processes along the channel (lake outburst, GLOF cascade), as well as the impacted hydropower plants, flood-triggered landslides, major population centers, discharge, and gauging stations. (B) Schematic showing the SLL outburst including the lateral moraine that collapsed into the lake and the breaching of the frontal moraine. (C) Pre- and post-GLOF high-resolution SkySat imagery (imagery © Planet Labs, 2023) showing the lake, failure zone of the northern lateral moraine, and the breached frontal moraine. Field photographs show (D) the breached frontal moraine; pre- and post-surface along AA′ and the eroded cross-sectional area shown in panel E, and (F) the northern lateral moraine failure zone, and the post-GLOF lake level drop. (G) Pre- and post-GLOF surface along cross-section BB′. Cross-section locations of AA′ and BB′ are shown in panel C. Photo credits: KSK and ITBP.

Drivers and causes of the 3 October 2023 GLOF from South Lhonak Lake

On 3 October 2023, the hazard cascade began with the collapse of ~14.7 × 10^6 m^3 of lateral moraine into SLL lake (Figs. 1B and 1C) at 22:12:20 Indian Standard Time (IST) [~16:42:20 Universal Time Coordinated (UTC)] which caused a tsunami (Figs. 2B and 3A). The wave overtopped and eroded the frozen frontal moraine with a maximum wave run-up ~15 m over the frontal moraine. This resulted in a breach 165 m wide (top width) and 55 m deep (Figs. 1D, 1E, and fig. S1C) that released ~50 × 10^6 m^3 of water, approximately half of the total SLL volume (see Methods sections 1 and 4 for GLOF volume calculations and uncertainty). We calculated the observed GLOF volume from the lake level drop (~28 m) and the volume of collapsed moraine material deposited in the lake (Figs. 1F and 1G, figs. S1B and S8). The breach exposed massive buried dead ice embedded within the permafrost of the frontal moraine (fig. S1A).

The moraine slide, measuring ~900 m in width and ~88 m in thickness, occurred on the North flank of the lateral moraine, close to the South Lhonak Glacier terminus (Fig. 1B). The dimensions and volume of this moraine collapse, as well as the frontal moraine erosion, were calculated from DEMs of Difference (DoD) created by differencing high-resolution (4 m resolution) pre- and post- Digital Elevation Models (DEMs), (section 1). SPOT-6 (1.5 m) and Pléiades (0.7 m) stereo-pairs were used to create the pre-GLOF (1 December 2018) and post-GLOF (29 October 2023) DEMs respectively. To quantify the pre-and post-GLOF lake level and moraine changes, we computed DEMs at 1 m resolution for 18 October 2022 and 29 October 2023, both from Pléiades stereoscopic images (*28*). We also obtained a 16 July 2017 DEM from the High Mountain Asia 8 m DEM Mosaics (*29*) (Fig. 1G).

We computed the displacement of the SLL northern lateral moraine using optical feature tracking (*30*, *31*), applied to 257 satellite image pairs between January 2016 and September 2023 (section 2). The moraine had a maximum coherent displacement >15 meters per annum (m a^{-1}) between 2016 and 2023 (Fig. 2A and fig. S2) (median velocities are shown in fig. S3). We distinguish two primary displacement zones, one up-glacier from the 2023 glacier terminus (Zone 1; see Fig. 2A) and a second to the east of the terminus (Zone 2). The fastest slope velocities are found in Zone 1 (>10 m a^{-1} since 2016) while Zone 2 accelerates from ~1 m a^{-1} to ~10 m a^{-1} from 2016 to 2023, with the most rapid speed immediately preceding the failure on 3 October (fig. S2). The two zones coalesce in 2022 to form a continuous complex of fast moraine displacement centering on the failure zone.

Seismic waveforms and spectrograms, from broadband stations near Mount Everest (EVN; 135 km away), Kathmandu (KKN; 286 km away), and Lhasa (LSA; 349 km away), indicated a potential landslide signal (section 3) (fig. S4). Seismic data force inversion pinpointed the moraine failure timing (*32*, *33*) (Fig. 2B and fig. S5). We used the inverted force history and a mass of 2.875 × 10^{10} kg, based on a volume of 12.5 × 10^6 m^3 (failure mass above the lake surface) and an estimated density of 2300 kg m^{-3} (considering it to be a mixture of ice and rock mainly comprising of Phyllite and Biotite-Gneiss) (*34*), to estimate the slide trajectory (Fig. 2C), which suggests a runout distance of 690 m, and movement to the southeast, consistent with the moraine collapse into the lake. The total maximum force was 2.8 × 10^{10} N, oriented largely N-S.

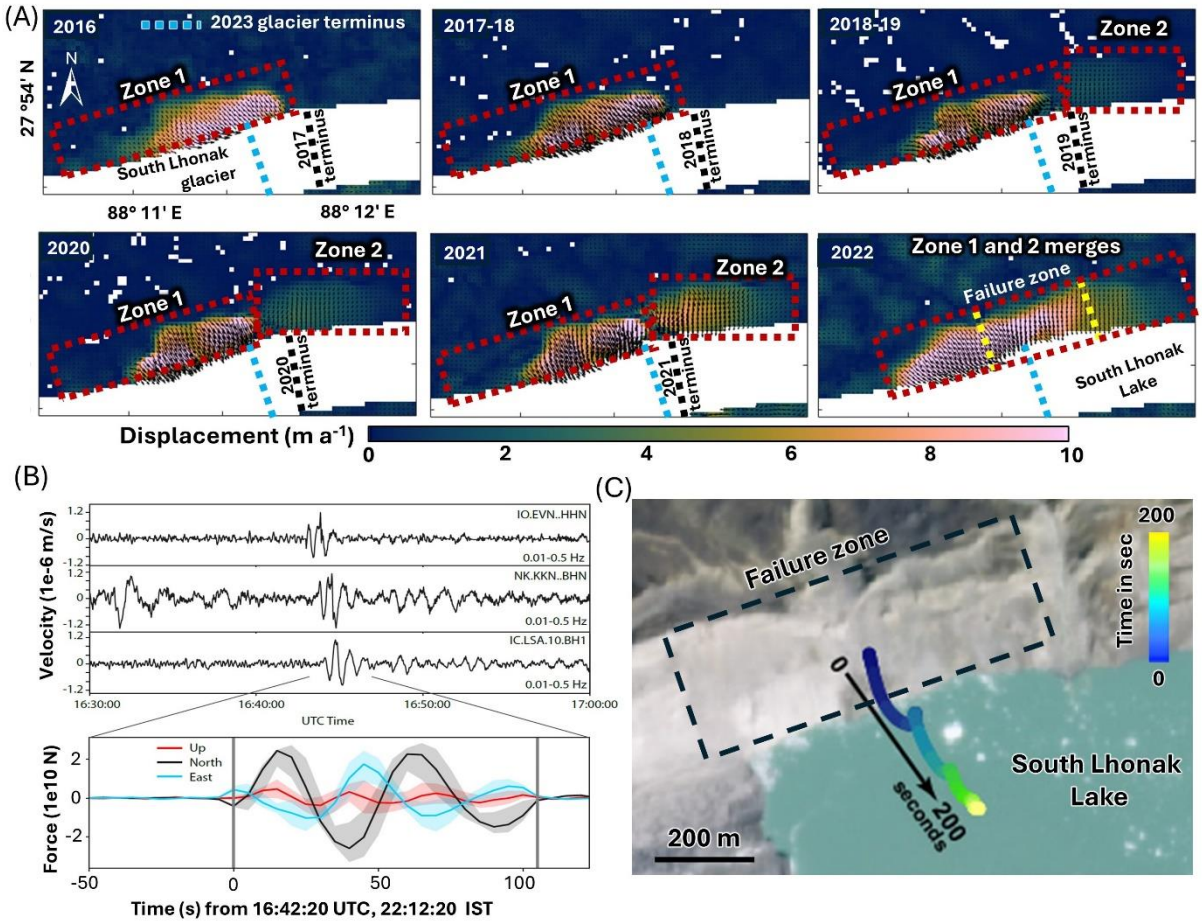

Fig. 2. Details of the moraine collapse. (A) Displacement of the perennially frozen northern lateral moraine from 2016-17 to 2022-23; the moraine failure zone is marked on the displacement map of 2022-23. (B) Seismic waveforms and inverted force history of the lateral moraine collapse into the lake. (C) Trajectory of the mass movement (collapsed northern lateral moraine) for the first 200 s, from the force history inversion of the seismic signals.

We employed a multiphase numerical model to reconstruct the SLL GLOF process chain (section 4) that propagates as debris flood based on the mixture of the lake's water and eroded moraine debris (*35*). We ran a simulation ensemble, varying the erosion coefficient and basal friction angle, and comparing this to reference datasets including flood arrival time, seismic records, observed GLOF inundation, and moraine erosion to identify the most suitable parameter combinations (fig. S7) (section 4). The modeled collapse of the north lateral moraine, starting at 22:12:20 IST (as per seismic data in Fig. 2B), generated a tsunami ~20 m high at the impact site. The resulting overtopping wave initiated erosion of the frontal moraine until the maximum breach depth of 55 m (observed erosion, Fig. 3B) was reached at ~22:24:00 IST (Fig. 3C). Our model predicts up to ~16 m of moraine sediment accumulation at the bottom of SLL following the collapse (fig. S8). The reconstructed outflow water discharge (fluid phase, P_L) immediately downstream of the lake (at cross-section CS-1 shown in Fig. 3A) peaked at 4.85×10^4 m^3 s^{-1} (Fig. 3D), with the eroded sediment discharge (solid phase, P_s) from the frontal moraine peaking at 1.03×10^4 m^3 s^{-1}. The GLOF peak discharge at CS-1 vastly exceeds meteorological flood magnitudes, suggesting that it is a rare event in the historical context of this region, equivalent to a return period exceeding 200 years *(3)* (Fig. S9). The outflow hydrograph (at CS-1) revealed the GLOF process chain, where the initial impulse wave immediately after impact lasted for ~3 minutes, causing progressive erosion of the frontal moraine. This was followed by slow breaching of the moraine for ~13 minutes, revealed by the

decreasing sediment discharge of the eroded frontal moraine (P_S) and gradually increasing water discharge (P_L). Thereafter, erosion further slowed until full breaching of the moraine was reached. The water discharge from the lake became constant after ~18 minutes. Modeled maximum flow depth and velocity of P_L at CS-2 (located 1 km downstream of the breached moraine) are 11 m and 26 m s^{-1} respectively (Fig. 3E). The reconstructed GLOF reached the Indo-Tibetan Border Police (ITBP) camp, 7.12 km downstream, at ~22.30:00 IST, consistent with the reported arrival time from ITBP officials (personal communication). The GLOF reached Chungthang (location of the 1200 MW Teesta-III hydropower, at CS-6, Fig. 3F) at ~00:30:00 IST (4 October), in line with the reported arrival time (~00:35:00 IST on 4 October). The discharge peaked at 5340 m^3 s^{-1} at Chungthang within ~6 minutes of the GLOF's first arrival with ~1.0×10^6 m^3 and ~3.5×10^6 m^3 of water accumulating in the first 5 and 10 minutes, respectively (Fig. 3F). The flow depth and velocity at Chungthang reached a maximum of 9 m and 9 m s^{-1} respectively (Fig. 3F). The GLOF inundation reconstruction showed good agreement with observations mapped using 2 m resolution Pléiades multi-spectral post-GLOF imagery acquired between 21 - 31 October 2023 and seismic flood signals (Figs. 3A and 3F, fig. S6).

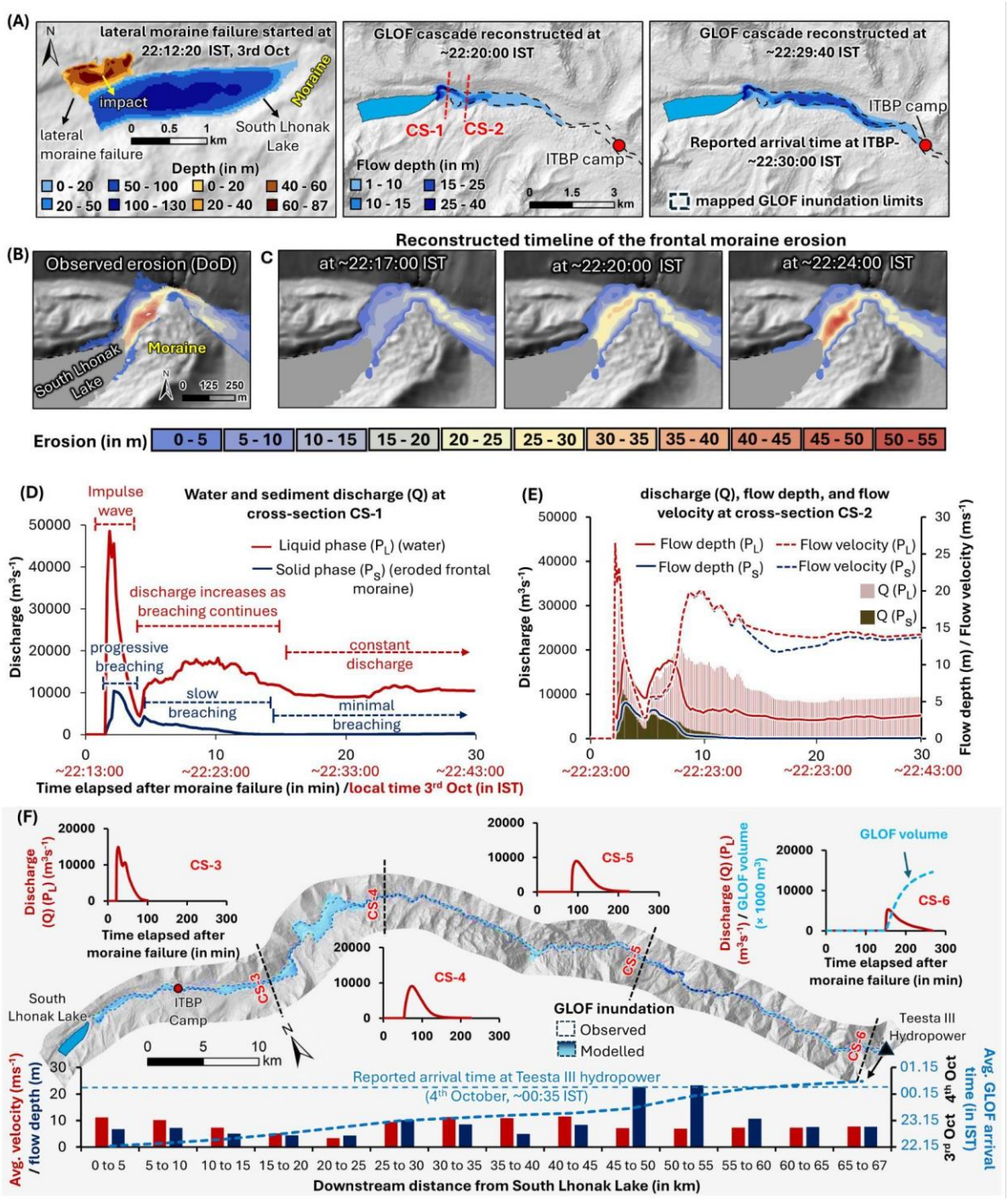

Fig. 3. Summary of the reconstructed GLOF process chain. (A) (left panel) Depth distribution of the collapsed moraine and the lake bathymetry immediately before the initial collapse of the northern lateral moraine (at 22:12:20 IST, reconstructed from the seismic data); maximum flow height and the reconstructed timing of the GLOF process chain; the reconstructed GLOF is compared to the observed inundation limits and arrival flood time at the ITBP camp located 10 km downstream of the lake. (B) Observed maximum erosion of the frontal moraine derived using DoD is compared to the (C) reconstructed timeline of the frontal moraine erosion. (D) Reconstructed GLOF process inferred from the modeled discharge (Q) vs. time plot of the two phases: lake water (P_L) and eroded sediments of the frontal moraine (P_S) at a cross-section CS-1 located immediately below the lake (see panel A for location). (E) Discharge (Q) and flow depth/flow velocity vs. time of P_L and P_S at cross-section CS-2. (F)

Routed P_L from SLL to Teesta-III hydropower at Chungthang; subplots show discharge at four cross-sections along the flow channel (red hydrographs); at CS-6 the time vs. accumulated GLOF volume is shown (blue). Reconstructed average flow depths, velocity, and time of GLOF arrival every 5 km along the flow path are shown at the bottom and matched with the reported GLOF arrival time at the Teesta-III hydropower.

Moraine failure conditioning factors

South Lhonak glacier has undergone rapid mass loss in recent decades (figs. S12 and S19), in common with many Himalayan glaciers (*36*, *37*). This mass loss is driven by both long-term climate warming and local topographic and glaciological forcings such as glacier-lake interactions [e.g. (*38*, *39*)]. As there are no local meteorological observations, we use ERA5 Land to determine climatic trends and reconstruct the mass balance of South Lhonak Glacier since 1951 (section 6). Annual mean temperature has warmed 0.08 °C per decade (fig. S10A), with monsoon/summer temperatures in June, July, August, and September (JJAS) increasing at a slower rate of 0.04 °C per decade (fig. S10B) whereas JJAS total precipitation increased by 8.26 mm per decade since 1950 (fig. S11). The modeled mean mass balance of South Lhonak Glacier was -0.45 ± 0.33 m w.e. a^{-1} from 1950 to 2023 (fig. S12, section 6). Over the past four years, mass loss increased to -0.58 ± 0.33 m w.e. a^{-1}, coinciding with lake expansion up to 100 m a^{-1}. The three warmest summers on record occurred in 2020, 2022 and 2023 (fig. S10B) (*40*).

Large-scale deformation of the northern lateral moraine is consistent with our understanding of other steep, frozen, and warming mountain permafrost slopes (*41–43*). Models incorporating climate data, incoming solar radiation, and ground truth from viscous creep features (rock glaciers) all predict permafrost occurrence within the SLL moraines (*44–46*), of which we assess the properties and implications (figs. S13 - S18, section 7). Estimated near-surface temperatures and permafrost depths are -1 to -3°C and around 100 m for the northern lateral moraine (failure zone) and -3 to -6°C and >200 m for the shaded southern moraine. We estimate permafrost warming reaching about 100 m below the surface, close to the slide detachment depth of 85 m (likely near the local permafrost base) (section 7). Field investigations reveal exposed dead ice and ductile deformation on the exposed scarp of the breached frontal moraine, indicating ice-supersaturated morainic material (fig. S1). The final collapse of this northern moraine was connected to glacier retreat and lake growth (fig. S19), as well as water input from a stream draining adjacent glacierized basins. Pre-GLOF mapping of the collapsed moraine surface (1 January to 28 September 2023) exhibited mass movement scars depicting small-scale slope failures (fig. S20). In these circumstances, slopes can progressively evolve towards a critical threshold, or an external event can trigger slope failure (*11*). Velocity mapping shows that the slope exhibited extensive, rapid deformation for years preceding the collapse (Fig. 2A; figs. S2 and S3).

A low-pressure cyclonic system, bringing heavy rainfall to Bangladesh, West Bengal, and Sikkim on 3 and 4 October, was proposed as one potential trigger for this collapse (Fig. 4; figs. S21 and S26; section 8). ERA5 reanalysis shows 29-39 mm of rainfall was recorded over SLL from 28 September - 5 October, with modest amounts of ~5 mm and ~14 mm on 3 October and 4 October, respectively (fig. S23). Also, ERA5, CPC, and IMERG rainfall pattern and amount all showed good agreement over the rainfall gauging stations, over SLL, and for the region 10°N-30°N, 70°E-100°E, with the available data providing no evidence of a triggering cloudburst event in the vicinity of SLL (figs. S22- S27, section 8, and table S9). The rainfall intensities observed are typical for this region and season, which suggests that the impact of the event has been conditioned by processes that have increased sensitivity of the hazard cascade to landscape and extreme rainfall events.

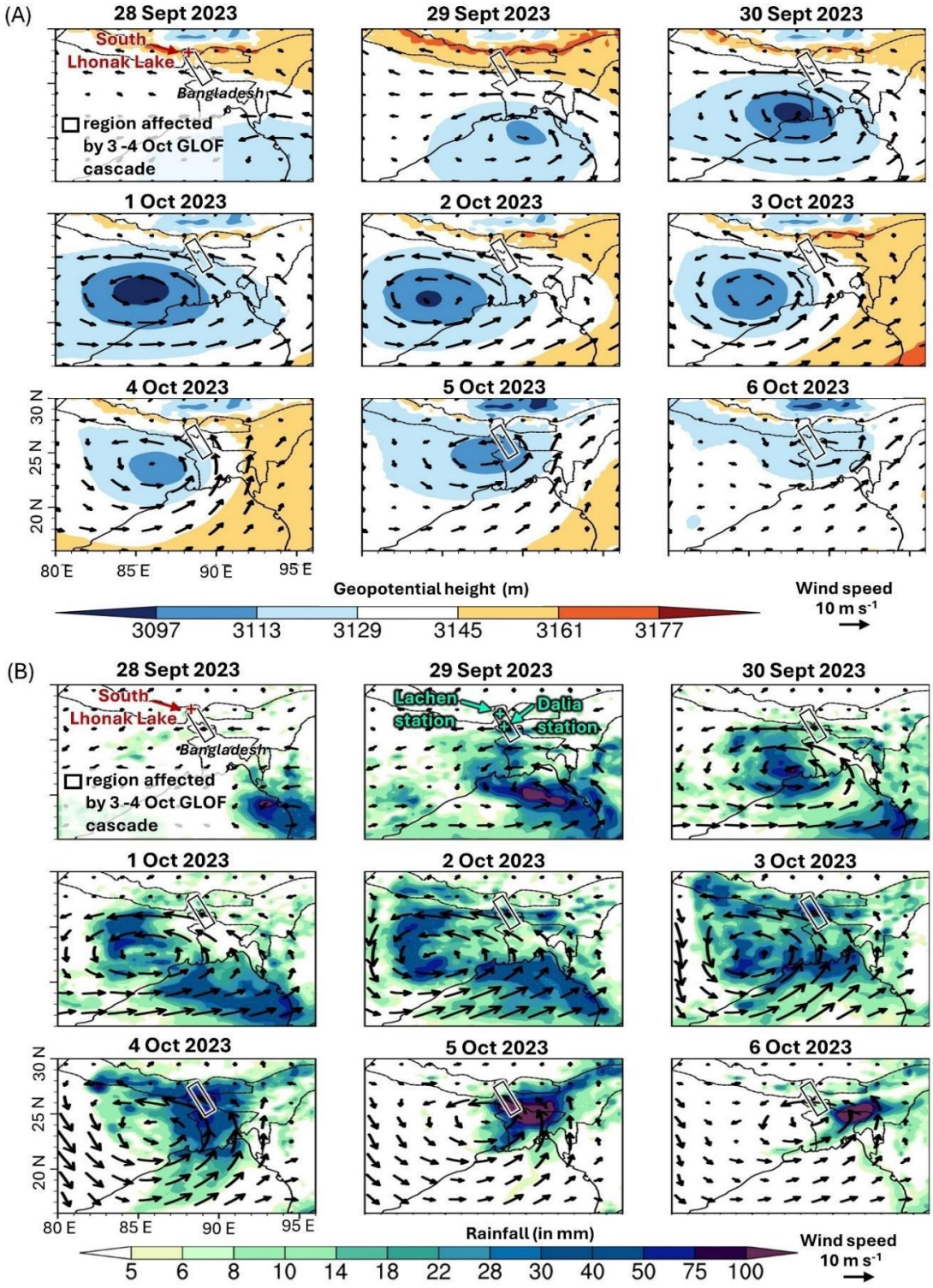

Fig.4. Meteorological conditions before, during, and after the GLOF. (A) Spatial distribution of daily geopotential height with winds at 700 hectopascals (hPa) isobaric surface over eastern India and Bangladesh from 28 September to 6 October 2023. (B) Spatial Distribution of daily ERA5 rainfall with winds at 700 hPa isobaric surface over eastern India and Bangladesh from 28 September to 6 October 2023. The ERA5 rainfall was compared to two station datasets: Lachen (in Sikkim) and Dalia (in Bangladesh) (figs. S22, S24 and S25). Spatial distribution of ERA5 daily specific humidity is shown in fig. S21.

GLOF-induced erosion, channel aggradation, and landslides

A total of 45 secondary landslides (noted L1-L45) were observed, triggered by the GLOF cascade (fig. S28). We mapped the landslides using 0.7 m resolution post-event Pléiades imagery (acquired on 24, 29, and 31 October and 5 November 2023) in the first 67.5 km downstream of SLL (figs. S28A, S30, and S31, table S1) and used 3 m PlanetScope imagery (acquired between 9 to 19 October 2023) further downstream. Landslides mapped from satellite imagery were cross-referenced with field evidence (figs. S28 B-J). No co- or post-GLOF landslides were detected beyond 108 km downstream of the lake (520 m a.s.l). Erosion and deposition volumes and their uncertainty along the Teesta Valley were calculated using DoD of pre- (1 and 8 December 2018) and post-GLOF (24, 29, and 31 October and 5 November 2023) DEMs (section 1). At 35 km downstream, the Teesta River was dammed by a series of landslides (L6-L8) (fig. S28M). We mapped the area of this landslide-dammed lake at ~8.185 x 10^3 m^2 from 24 October 2023 Pléiades imagery. Results showed that the L6 deposits created a dam with a maximum height of 19 m and volume of ~5.8 x10^4 m^3. The lake persisted as of 24 May 2024. Partial drainage of the lake occurred through a channel cutting through the landslide deposits (fig. S29). Most landslides resulted from lateral erosion of the valley walls by the GLOF, destabilizing slopes and leading to their failures.

Between 35 km downstream of SLL and Teesta III, the flood wave eroded both vertically and laterally (Fig. 5). Elevation differences measured before and after the flood indicate lateral channel shifts of up to 100 m. Many of the landslides were deep-seated, with depths up to 150 m (Fig. 5A). Lateral erosion of the valley caused slumping in L43, where roads and concrete walls were offset by several meters (fig. S34). The sustained geomorphic impact of the flood along this part of the river can be attributed to channel steepness, which generally increases shear stresses at the channel bottom, and prevents attenuation of the flood peak (hydrographs in Fig. 3 for CS-4 and CS-5) (*47*). Also, downstream of 35 km, valley side walls (within 500 m around the river) have average slopes between 30-40°. These values are consistent with the effective angle of internal friction controlling hillslope stability (*48*), suggesting that this part of the river runs through a valley prone to mass wasting. Valley cross-sections (Fig. 5F) moreover show that landslides mostly led to a slope-parallel retreat of the topographic surface, rather than decline in hillslope angle, suggesting that hillslopes instantaneously adjusted to undercutting by lowering to a threshold hillslope angle.

The total eroded volume is estimated at ~270 × 10^6 m^3, of which combining GLOF erosion and triggered landslides occurred upstream of Chungthang is ~233 × 10^6 m^3 (in the first 67.5 km stretch) (Fig. 5A, table S3). In terms of volume of material, this would be equivalent to basin-wide erosion of 9 cm across the entire catchment (area = 3021 km^2) upstream of the Lachung-Teesta confluence.. Only 7% of the total eroded volume is observed in the first 30 km of the channel where GLOF-triggered landslides are absent (Fig. 5A). The erosion volume increases in the landslide-dominated stretch from 30 km downstream of the lake to Chungthang (Fig. 5A). Maximum erosion of 66.5 × 10^6 m^3 occurred 40-45 km downstream (table S3), where reconstructed GLOF flow velocity is maximum (fig. S36). The triggered landslides can be attributed to river erosion induced by high flow velocities with substantial lateral and vertical erosion observed in the field and remotely at various locations downstream along this stretch (fig. S37). Field observations suggest that the transition from erosion to aggradation occurred downstream of the Lachung-Teesta confluence (near Mangan) (Fig. 6). The town of Rangpo, ~135 km downstream of the lake, was severely impacted by the debris, burying buildings and automobiles (Figs. 6C and 6D). Other severely impacted areas include Geli Khola, Teesta Bazaar, and Bardang (Figs. 6B, 6E and 6F).

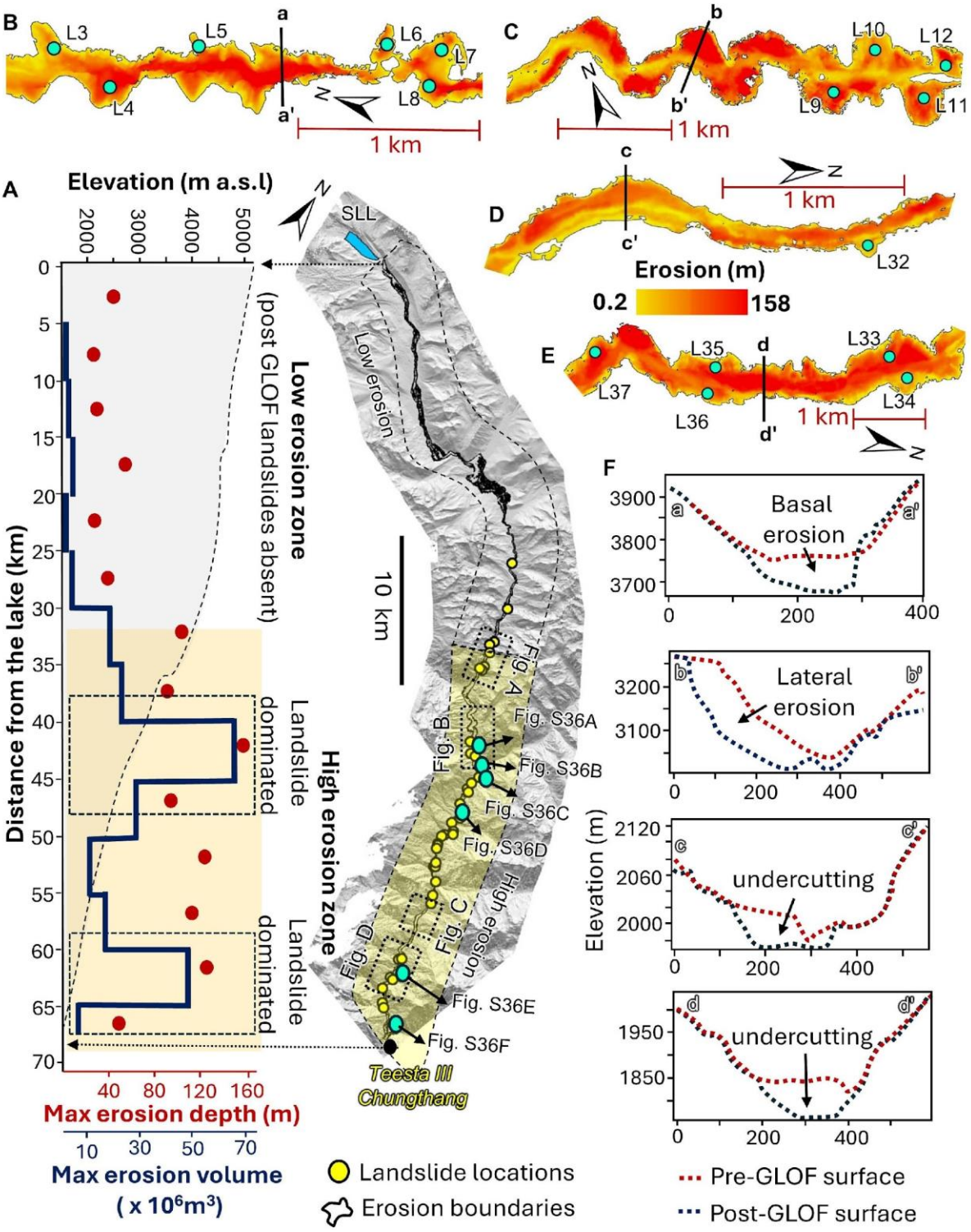

Fig. 5. Summary of the GLOF-induced erosion (observed). (A) (left) Distance from the lake (in km) vs. elevation (along GLOF flow channel), maximum erosion depth, and maximum erosion volume; (right) the GLOF valley showing the erosion zones in the 67.5 km stretch from the lake to Chungthang; marked are the co- or post-GLOF landslides and field observations (fig. S37). (B-E) Spatially distributed erosion depth of different sections from upstream to downstream along the Upper Teesta Valley; the co- or post-GLOF landslides are marked. (F) Pre- and post-GLOF elevation vs. distance plots across cross-sections showing undercutting

and lateral erosion at different locations along the Teesta valley; the locations of the cross-sections (a-a' to d-d') are shown in panels B to E.

Fig. 6. Field evidence of sediment aggradation. Photographs taken along the Teesta River show the aggradation of the sediments transported by the flood cascade and its impact. Latitude, longitude, and elevation (in m a.s.l) are at top right; locality name and distance from SLL are at bottom right. Photo credits: Praful Rao (co-author).

Impacts on population, infrastructure, agricultural land, and transboundary implications

The flood cascade damaged ~25,900 buildings, 59% built in the last decade (Fig. 7A, table S4, and section 9). Most affected buildings are located below Chungthang, within 200-385 km of the lake, with the most heavily inundated zone between 290 and 385 km downstream in Bangladesh. Similarly, ~276 km^2 of agricultural land was flooded (Fig. 7B, table S5). A total of 31 major bridges made up of Reinforced Cement Concrete (RCC) or steel (Bridges: B1-

B31) (*18*) along the Teesta River were damaged, including 14 upstream of Chungthang (Fig. 7C, figs. S39 and S40, table S6). Moreover, ~20 small pedestrian bridges in Sikkim were also affected (*18*). A road length of ~18.5 km was damaged, ~6.4 km of which was due to secondary landslides (fig. S32, table S7). Approximately 200 buildings were impacted by these triggered landslides, 90 % of which were caused by the two largest adjacent landslides, L33 and L35, located 60 km downstream of SLL (figs. S28K, S28L, and S33, table S1). A total of 10 landslides damaged the road network (fig. S32, table S2), L43 (known as the Naga landslide) causing maximum damage in terms of road length (fig. S34).

The GLOF and associated erosion volumes destroyed the 1200 MW Teesta-III hydropower dam at Chungthang. The cascading flood continued downstream, affecting another four dams: Teesta V, Teesta VI, Teesta Low Dam III, and Teesta Low Dam VI (Fig. 7C and fig. S38). Field visits to assess the impact of the flood were undertaken along the Teesta Valley (figs. S38 – S40). Post-disaster surveys by a multi-stakeholder team constituted by the Sikkim State Disaster Management Authority (SSDMA), including sector experts, government representatives, international organizations, and others (*18*) revealed that the GLOF impacted 100 villages in Mangan, Pakyong, Gangtok, and Namchi districts, causing 55 deaths, 74 missing persons, over 7025 displaced individuals, and significant livestock losses, including 547 cattle, 62 sheep, 664 goats, 586 pigs, 7252 poultry, 51 calves, and 200 rabbits (*18*). Transboundary flood impacts included infrastructure damage in Bangladesh, particularly in Rangpur district (fig. S41, section 10). Other affected districts were Lalmonirhat, Kurigram, Gaibandha, and Nilphamari before the floodwaters discharged into the Brahmaputra River. Water levels in the Teesta River in Bangladesh rose around noon on 4 October, ~16 hours after the initiation of the GLOF. Rainfall, water level, and sediment discharge data from 17 September 2023 to 29 October 2023, collected by the Bangladesh Water Development Board (BWDB) at the Dalia station (26.1758°N, 89.0505°E, in Dimla Upazila Nilphamari District) (section 10), which is the first station to encounter the flood along the path of Teesta in Bangladesh (see Fig.1 for location), indicated that water levels on 4 October 2023 reached ~52 m, perilously close to the dangerous threshold of 53.15 m. Despite minimal rainfall on 4 October, the water levels mirrored those of 24 September, when Dalia Station recorded substantial rainfall (~150 mm), suggesting that the elevated discharge on 4 October was primarily due to the upstream flood cascade.

Post-flood, weekly suspended sediment discharge at the Dalia station between 8 October and 15 October 2023, reached 6587.5 kg s^{-1} (on 15 October 2023), which is respectively 5 times and 2.8 times higher than the average and maximum discharge in the preceding month (September 2023) (fig. S41D). This spike in sediment discharge was 17 times higher than in the week preceding the flood event. An increase in the river turbidity also occurred upstream of Dalia and at the confluence of Teesta and Brahmaputra rivers (figs. S42 and S43). The coarse sediment discharge peaked on 8 October 2023 and was respectively 8 times and 6.5 times higher than the average and maximum discharge in the preceding month.

The analysis shows that more than ~17,000 buildings in Bangladesh were impacted by the flood, with ~50% built in the last decade (Fig. 7A). The total agricultural land inundated in Bangladesh was 168 km^2 (Fig. 7B). The easterly movement of the low-pressure system caused heavy rainfall, exceeding 300 mm per day in several places, in Bangladesh, and 75 mm at Dalia station (Fig. 4B, figs. S25 and S26), from 5 to 7 October (Fig. 4B), contributing to the flooding impact. Thus, the effects in Bangladesh were due to both the GLOF cascade on 4 October and the intense rainfall that followed immediately on 5 October 2023.

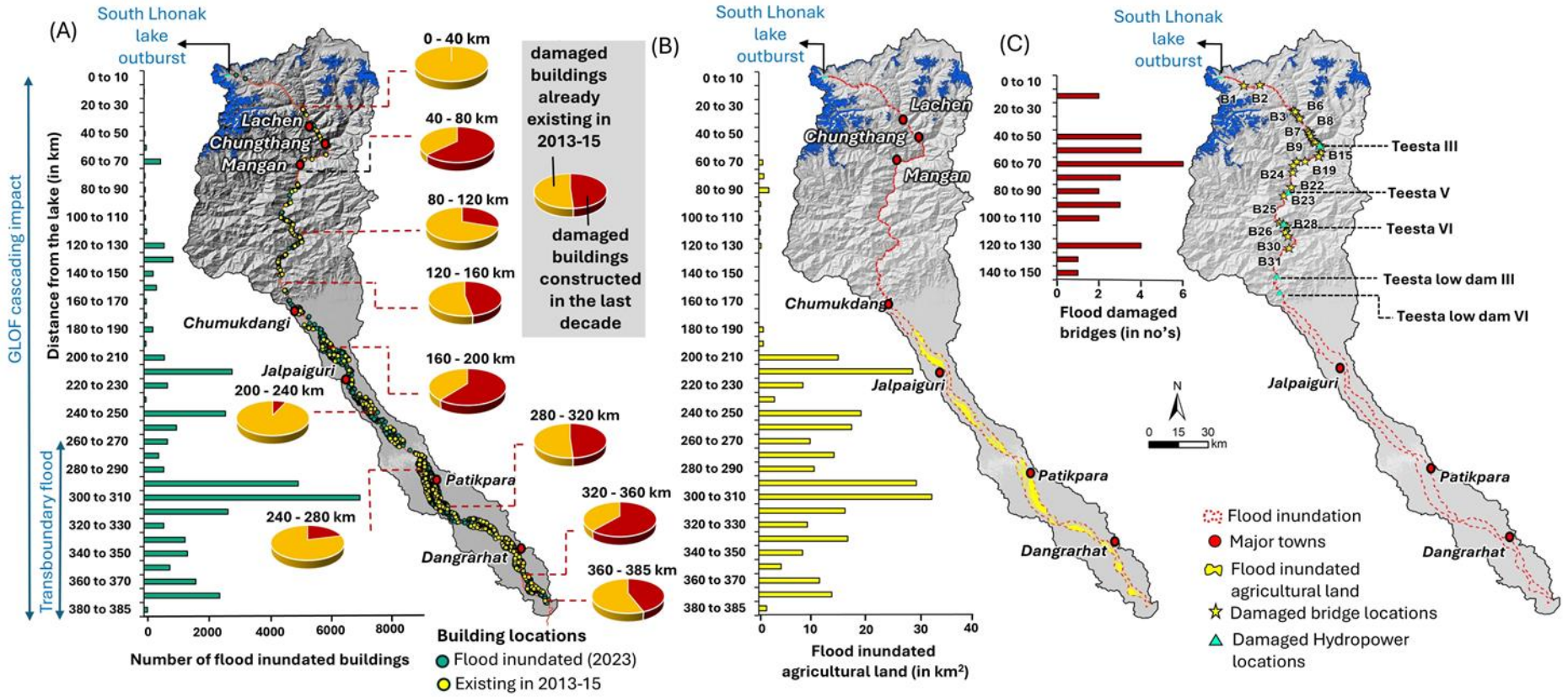

Fig. 7. Summary of the damage assessment. (A) Flood inundated buildings along the entire stretch of the Teesta valley; Bar-plots show the number of inundated buildings in every 10 km stretch along the flood path; Pie-charts show the percentage of damaged buildings existing in 2013-15 and the damaged buildings constructed in the last decade in every 40 km stretch along the flood path. (B) Flood inundated agricultural land; bar plot shows inundated agricultural land for every 10 km stretch along the flood path. (C) Flood-damaged major bridges (B1 - B31) and hydropower plants; bar plot shows the number of bridges damaged in every 10 km stretch along the flood path.

Future GLOF hazard in the Teesta Valley

SLL remains highly susceptible to future GLOF events, including repeat triggers from northern lateral moraine failures. Despite the 3 October failure and associated slope changes, the northern moraine still comprises a large and rapidly deforming zone. We computed post-event surface velocities using 1635 satellite image pairs between October 2023 and June 2024, revealing that a ~0.5 by 0.3 km region of the collapse scarp is deforming at rates up to 15 m a^{-1} (fig. S44). The modified slope geometry following the collapse may cause further failures, with moraine curvature at the crest now higher than before the 2023 failure. Small-scale mass movements are visible on the failure slope (fig. S45, section 2).

Debuttressing due to glacier surface lowering and glacier retreat must be considered a primary factor for slope destabilization, increasing outward and downward forces in the frozen moraine. SLL is expected to grow by another ~1 km in length as the glacier retreats (*14*, *49*). With continued retreat of the calving front, debuttressing will affect frozen moraine slopes up-glacier (zone 1), which already show slow downslope movement post failure (fig. S44B, section 2). Lateral stress coupling must have induced load removal on the up-glacier part, causing it to slow down. A GLOF could potentially be triggered by exposure of Zone 1 on the northern lateral moraine, particularly the eastern flank, due to loss of lateral support following the 3 October collapse. As well as this slope debuttressing, steep slopes surrounding the lake are potential avalanche source zones and thus potential GLOF triggers at moraine-dammed lakes (*14*, *50*). The southern moraine appears stable. However, continued warming, glacier retreat, and permafrost decay could initiate instability in the northern moraine. Downwasting of exposed dead ice on the breached frontal moraine could lower the lake's outlet channel, increasing outflow during future GLOF events.

The GLOF eroded the riverbanks laterally, weakening them and making them susceptible to future collapse, particularly near roads and settlements. For instance, post-GLOF landslide (L17) and slumping below Lachen (see fig. S35) show widened riverbank scarps encroaching closer to settlements. The Naga landslide (L43) also showed slumping in the months after the GLOF (fig. S34). Significant lateral erosion damaged the national highway (NH-10) in multiple locations (fig. S32), blocking major trade routes and isolating mountain communities. The ongoing deterioration of roads months after the 3 October GLOF event, exacerbated by subsequent monsoon floods, further eroded the valley walls, posing a hazard to infrastructure and disruption to transport (fig. S47).

Flood deposits along the Teesta Valley remain exposed to further erosion and transport, potentially triggering future debris flows (Figs. 5 and 6). Moreover, aggradation has raised the riverbed by several meters, heightening the risk of early onset of bank-full conditions during future floods, increasing the probability of flooding in adjacent floodplains, and exposing populations and infrastructure to greater risks (fig. S46). This concern extends to future GLOFs and high discharge, monsoonal flood events. Crucially, even though the landslide-dammed lake (L6) formed after the GLOF event partially drained, the landslide deposits still present a continuing hazard, potentially amplifying the impact of future GLOFs originating upstream (figs. S28M and S29). These eroded sediments are rarely considered in the analysis of GLOF risks.

Summary and perspectives

The multi-hazard cascade and consequent disaster of 3 October 2023 underscore challenges in GLOF and multi-hazard assessments that often underestimate the potential intensity and impacts in mountain regions where the hazard from the GLOF itself is significantly conditioned, and in this case, exacerbated, by the downstream geomorphic system (*51*). The SLL triggering was not remarkable in terms of rainfall; rather, the situation was significantly

exacerbated by the effects of climate warming on the drivers of GLOF. On 3 and 4 October, the Teesta Valley experienced heavy rainfall, which saturated the soil and increased the vulnerability of slopes to failure. This preconditioning effect primed the landscape, leading to numerous landslides triggered by the GLOF event. These secondary landslides added to the sediment volume in the floodwaters and contributed to the overall devastation along the downstream flow paths. Rainfall fueled the flood cascade downstream. This additional influx of water intensified the volume and velocity of the floodwaters, leading to more severe impacts on infrastructure, communities, and agricultural lands in Sikkim, West Bengal, and Bangladesh.

The sheer volume of water (~50×10^6 m^3) released from the lake, together with the sediment (~270×10^6 m^3) entrained along the valley drove the primary impacts that overwhelmed infrastructure and developmental activities along the Teesta River, exacerbating the human and economic toll. Despite the Teesta-III hydropower reservoir contributing 5×10^6 m^3 of water (assuming it was at full capacity), which is 10% relative to the initial SLL outburst volume, the GLOF's volume and especially its eroded sediment load dominated downstream impacts. Prevailing GLOF modeling and assessment approaches insufficiently account for processes of erosion and sediment transport, as well as hillslope-channel interactions such as riverbank collapses and landslides triggered by toe-undercutting as well as the impact of sediment transport on local bed elevations and hence water levels. The latter is of particular importance in large river basins because water waves move faster than sediment waves (*52*), with eventual deposition therefore driven by not only changing exogenic forcing (e.g. reductions in valley slope) but also endogenic processes where water outruns sediment. These processes alter flow rheology along GLOF tracks and thus flow behavior and geomorphic impact (*53*, *54*), yet adequate tools are lacking to support modeling, simulation, and prediction. Based on our calculation from DoD and GLOF volume, the ratio of the mobilized sediment to the water released from SLL and the Chungthang reservoir reaches 0.83 at the downstream end of the erosion zone. The calculated lake outburst volume and sediment entrainment along the flow path indicate a bulking factor of about 5 (i.e. a 5 times increase in flow volume) which is at the upper end of comparable large debris-laden flows (such as GLOFs, debris flows, lahars) (*55*, *56*). Erosion rates averaged over 70 km to SLL are ~3850 $m^3 m^{-1}$ (Fig. 5) which is three orders of magnitude higher than observed for granular alpine debris flows. There, intense precipitation the days prior to the GLOF has likely played an important role in the very high erosion and entrainment processes by wettening and saturating the soil along the flow path, as flow conditions and bed wetness are decisive factors to control erosion (*57*). Neglecting intense sediment entrainment and subsequent bulking (and dilution) can lead to inaccuracies in flood models, potentially underestimating the hazard posed by GLOFs and meaning that design standards for infrastructure may not be appropriate. Hence, comprehensive and integrative approaches to GLOF hazard assessment (*3*) are urgently needed, considering not only the lake and outburst potential but also downstream landslide susceptibility along the flow path and potential for cascading processes. Also evaluating geomorphic work induced by these GLOF events relative to normal monsoonal floods has scope for future assessments.

This Sikkim flood event is a reminder of some much wider implications including the urgent need for Early Warning Systems (EWS) in the Himalaya, recognizing the complex technical, practical, institutional, and social dimensions that need to be addressed. Expanding and enhancing these systems across the Himalaya is critical for timely hazard detection and effective response, as well as reducing the impact of future GLOFs on communities and infrastructure [c.f. (*58*)]. Addressing these complexities requires robust infrastructure, advanced technology, and effective coordination among stakeholders (*59*) to ensure the reliability and effectiveness of EWS in the Himalaya and other challenging mountain environments. In terms of transboundary GLOF impact, this event demonstrates the complex and interconnected nature of natural hazards in mountainous regions and their far-reaching

damage, highlighting the importance of regional cooperation and coordinated efforts among countries sharing river basins to enhance resilience and preparedness against the increasing risks posed by GLOFs (*26*, *58*, *60*). Moreover, the significant impact of intense precipitation on flood dynamics and downstream effects observed during this event, particularly in Bangladesh, highlighted the urgent need to integrate response planning and enhance preparedness from a transboundary perspective.

Efforts to mitigate the hazard posed by SLL have been ongoing before the catastrophic flood. An initial lake bathymetric survey was conducted in August 2014, and the first mitigation measures began in September 2016 through the installation of siphons to lower the lake level (*61*). The most recent expedition was in September 2023, just before the lake's outburst on 3 October, when repeat bathymetric measurements were conducted, and an automated weather station and cameras were installed at the lake site (*62*). The expedition also recommended additional mitigation measures, such as constructing check dams, retention walls, deflection dams, and implementing an EWS (*34*) in the valley. In light of the consistently high hazard levels in SLL and valley conditions following the October 3 GLOF event, which has caused rapid remobilization of flood sediments, urgent risk mitigation and management plans are required. These plans must address the altered conditions of both the lake and valley and prepare for potential future scenarios. Comparable conditions were noted right after the Chamoli event (*63*). While the 3 October disaster has placed the immediate focus on SLL, broader attention, and high priority also needs to be given to the various potentially dangerous lakes identified across High Mountain Asia region. The need for enhanced basin-scale EWS, adaptive infrastructure planning, and cross-border collaboration in hazard management is evident to mitigate the socio-economic and environmental consequences of future GLOF events.

Strengthening regulatory frameworks is crucial to mitigate the increasing risks posed by the proximity of hydropower projects to glacier lakes and in high mountain environments in general. The trend of high GLOF susceptibility in the Himalaya indicates a greater likelihood of future GLOFs, exacerbated by the growing number of hydropower projects moving closer to these hazard-prone areas, thereby increasing exposure. With 47 hydropower projects and an installed capacity of >5300 MW, the Teesta basin has the highest density of such projects in the Himalayan region (*64*). These numbers are likely to increase and thus, comprehensive risk assessments, stringent building standards, and adaptive management practices are essential to ensure safety and sustainability in these vulnerable regions. This is crucial for safeguarding both infrastructure investments and the communities reliant on these developments in the Himalaya and other mountain ecosystems. Events of the magnitude of the South Lhonak GLOF, Chamoli ice-rock avalanche of 2021 (*27*), or Kedarnath flooding of 2013 (*23*) highlight potential limits to adaptation in the Himalaya, with even the most diligent and comprehensive suite of disaster risk reduction strategies unlikely to entirely prevent losses and damages occurring from such events. This calls for adequate assessment and communication of residual risks, and effective risk transfer mechanisms, such as insurance and governmental support, to ensure sustainable mountain development. This study highlights the necessity to establish specific guidelines and standards for GLOF risk reduction in the Himalaya and similar high-mountain regions. Structural and non-structural GLOF mitigation strategies should be prioritized, using advanced technology to address risks in extreme climate regimes.

The 3 October 2023 GLOF from SLL highlights the urgency of a paradigm shift in numerical modeling and observational techniques for GLOFs. This urgency extends to improving GLOF risk management and infrastructure development in high mountain regions. These shifts in approaches should help safeguard against the devastating impacts of GLOFs, thereby facilitating sustainable development in hazard-prone environments globally. We contend that improved EWS coupled with enhanced infrastructure resilience and rigorous land-use management practices are essential to mitigate GLOF risks. Furthermore, robust community

preparedness and education programs are crucial for effective emergency responses. This multi-hazard cascade exhibits the complex interactions between climate change, glacier mass loss, and human infrastructure in mountainous regions. Understanding and addressing multi-hazard cascades in similar vulnerable environments requires interdisciplinary approaches, robust monitoring systems, and proactive measures to minimize devastating consequences and enhance resilience.

Methods

1. DEM of Difference (DoD) and uncertainty

We generated pre- and post-GLOF Digital Elevation Models (DEMs) from 1.5 m SPOT6 and 0.7 m Pléiades stereo-pairs (all high-resolution data used in the study are listed in table S11). SPOT6 images were acquired on 1 and 8 December 2018, Pléiades images on 24, 29, and 31 October, and 5 November 2023 in emergency mode after the GLOFs. All DEMs were generated at a ground sampling distance of 4 m using the semi-global matching algorithm of the Ames Stereo Pipeline (*65*, *66*) and the processing parameters from (*67*). Both SPOT6 pre-event DEMs were first coregistered and vertically adjusted to the Copernicus 30 DEM, masking out glacierized areas using the Randolph Glacier Inventory (*68*) and then mosaicked to build the pre-event DEM. The Pléiades post-event DEMs were coregistered to this pre-event DEM. Next, we corrected spatially coherent biases in the elevation difference between each Pléiades DEM and the pre-event DEM using a polynomial fit across-track and a spline fit in the along-track direction (*69*). The post-event DEM was then subtracted from the pre-event DEM to map the elevation difference from the South Lhonak Lake (SLL) down to 67.5 km to Chungthang along the Teesta River. The topographic changes in the lake area were computed from two 1 m resolution Pléiades DEMs (tristereo of 18 October 2022 and the same stereopair of 29 October 2023) computed in Formaterre and aligned together on the GLO30 (table S11). The uncertainty on the mean elevation change is calculated using the patch method. This approach aims to empirically determine the uncertainty associated with the mean elevation change by sampling patches (or tiles) of the stable terrain of various sizes, in order to constrain the decay of the error with the averaging area [see Supplementary material of (*70*, *71*) for details]. The stable terrain is defined here excluding glaciers and a 1 km buffer around the river channels where erosion/deposition occurred. The 1-sigma (68^{th} percentile error) and the 2-sigma (95^{th} percentile error) were calculated to be ±0.69 m and ±1.42 m respectively. These uncertainties translate to erosion volume estimates with 1-sigma and 2-sigma errors of ±3.3% and ±6.9%, respectively. The downstream erosion and deposition estimates refer to all topographical changes between 2018 (1 and 8 December 2018) and 2023 (24, 29, 31 October, and 5 November 2023). We can reasonably assume that most of these observed topographical changes in this period are associated with the 3 October GLOF event, but we note that the derived values are upper bound estimates, as some changes might have occurred after 2018 and before the SLL GLOF event. The lake level changes, elevation changes at the collapsed northern moraine, and the frontal moraine erosion were calculated using the DoD created from DEMs of 18 October 2022 and 29 October 2023 (table S11).

2. Pre- and post-GLOF dynamics of the lateral moraine

Here, we employed an optical feature tracking workflow adapted from the Glacier Image Velocimetry (GIV) toolbox (*30*), originally designed for mapping glacier flow speeds. While glacier displacement typically ranges from 10^1 to 10^3 m a^{-1}, slow-moving landslides exhibit much slower rates, ranging from 10^{-2} to 10^2 m a^{-1}. To accommodate these differences, adjustments were made to the feature tracking workflow, allowing for longer temporal baselines between images, the utilization of multiple subpixel displacement algorithms, and the stacking of multiple velocity maps to distinguish actual deformation from background noise,

for instance from georeferencing errors between images or topographic distortion (*31*). We applied feature tracking to band 8 [833 nm wavelength; near-infrared; (*31*)] of Sentinel-2 L1C imagery with a 10 m spatial resolution.

Fundamentally, feature tracking involves comparing the properties of two images to identify the best-fit location of a pattern ('feature') in one image within the other. We employ frequency domain matching to determine displacement, overcoming challenges presented by varying glacier features, satellite imaging conditions, and the temporal spacing of images. Prior to running the feature-tracking algorithms, satellite images were filtered, and pre-processed. The images were filtered using the near anisotropic orientation filter (NAOF), which is particularly effective at enhancing feature contrast and removing contrast differences between clouded, shadowed, and clear areas (*30*). We assembled all image pairs with a temporal baseline greater than 9 months and ran the feature tracking with a single-pass chip-wise, frequency domain cross-correlation algorithm. Displacement maps were then post-processed, converting displacement to velocity vectors, filtering out low peak ratio pixels, applying local gap-filling, and correcting for systematic georeferencing errors. Post-processing primarily involved outlier filtering to improve the accuracy of resulting surface velocity maps. These methods were tailored for application to the northern lateral moraine of the SLL where we used 31 cloud-free Sentinel-2 L1C images from January 2016 to September 2023, for a total of 257 image pairs (Figs. 2A; figs. S2, and S3). Similarly, we computed post-GLOF surface velocities over the northern lateral moraine using 1635 satellite image pairs between October 2023 and June 2024 (fig. S44).

The extended vector field [Fig. 2A, fig. S3 (pre-GLOF) and fig. S44 (post-GLOF)] documents coherent deformation with large-scale stress coupling. Such coherent deformation is characteristic of perennially frozen debris with high ice content (supersaturation, excess ice) and related strong cohesion and reduced internal friction (see section 7 and figs. S13- S19 for permafrost and related aspects). The here-observed extending flow regime relates to the increasing slope inclination and related increasing driving stresses towards the lake. A maximum post-GLOF moraine deformation of 0.54 m a^{-1} was measured using InSAR (*72*). However, these velocities are relative to the satellite line-of-sight, which is most sensitive to east-west motion, and not the north-south motion that dominates the failure.

Further, to understand the dynamics of the northern lateral moraine, the surface of the 3 October 2023 failure zone was mapped using a time series of 3 m PlanetScope imagery before and after the GLOF event (figs. S20 and S45). For pre-GLOF mapping, monthly images from January to September 2023 were analyzed, whereas, for the post-event period, daily images from 6 October 2023 to 17 April 2024 were used (table S10). Manual delineation was executed at a scale of 1:4000 to ensure detailed mapping of the failure slope. Analysis of the pre-event images showed visible scoured ground on the northern moraine over the failure zone, indicative of small-scale mass movements (fig. S20). Following the GLOF event, the failed slope was mapped in detail. The numerous mass movements on the surface of the post-failure zone were marked (fig. S45). The analysis indicated that the failed slope is active even months after the GLOF event, also confirmed by the displacement velocity assessment (fig. S44).

3. Seismic records and GLOF signals

The displacement of a large mass on the earth's surface generates low-frequency (long period) seismic waves that attenuate slowly with distance from the source. As a result, the seismic signals of large landslides can be detected at distances of 100 s to 1000 s of kilometers from the landslide location, or even globally (*73*). When the seismic signal of a landslide event can be identified, the extremely high temporal resolution of the seismic data enables the precise timing of detected landslides to be determined (*27, 74*). For the SLL GLOF, identifying and

confirming the seismic signature of the lateral moraine failure provided the precise timing of the GLOF triggering process.

We used data from three publicly available broadband seismic stations, EVN, KKN, and LSA respectively located near Mount Everest, Kathmandu, and Lhasa at 135, 286, and 349 km from SLL (fig. S4). Data were downloaded from the IRIS Data Management Center (IRISDMC). Visual inspection of the waveforms and the spectrograms of the data indicated a possible landslide signal at 16:43 UTC depicting the northern lateral moraine collapse of SLL. We filtered the data to 0.1-0.5 Hz and performed a signal migration using the R package eseis (*75*) in order to locate the source of the signal. The N-component for each station had the highest signal-to-noise ratio, so was used for the signal migration. A seismic velocity of 3580 m s^{-1} yielded a best-fit location 7 km from SLL. Because EVN and KKN stations are at a similar azimuth relative to the source, the station geometry does not allow for a more precise location estimate. However, the estimated location probabilities indicate that the seismic signal is consistent with a source at SLL (fig. S4).

***Force inversion*:** In order to further investigate the moraine failure, we used the python library lsforce v. 1.1 (*32*, *33*) to perform a force inversion on the seismic data. This process assumes that the failure can be treated as a point-source moving mass that exerts a single force on the earth's surface and inverts the seismic data to obtain the best-fit force-time function, or force history for the moving mass (*76–80*). We followed the workflow outlined in (*32*) and in the lsforce documentation. For the inversion, we used all three components from each station, and for LSA station selected the 40 Hz (BHx) channels with location code 10. Data were filtered to a period of 15-80 s (0.0125-0.067 Hz). Forces were calculated using the triangle approximation with a half-width of 5s, using greens functions from the IRIS syngine service with model 'iasp91_2s'.

The best-fit force time function (Fig. 2B) yields dominantly horizontal forces, with a limited component of vertical force, consistent with the small drop height of the moraine failure. The total maximum force was 2.8e10 N, oriented largely N-S. With the force history and a known failure mass, a point-source trajectory can be estimated for the northern moraine failure of SLL by calculating acceleration from the force and mass and then integrating the acceleration twice for velocity and then displacement (*32*). We used a mass of 2.875e10 kg, based on a volume of 12.5 million m^3 (failure volume of the northern lateral moraine of SLL calculated from DoD, see section 1 and Fig. 1B) and an estimated density of 2300 kg m^{-3}. The trajectory calculated for the first 200 s of the event (Fig. 2C) suggests a runout distance of 690 m, and movement to the southeast, consistent with the failure of the moraine into the lake.

The force inversion also allows us to more precisely identify the initiation of acceleration of the collapsed mass. We can therefore conclude that the GLOF-triggering failure began at 16:42:20 UTC, or 22:12:20 Indian Standard Time (IST) (see Fig. 2B and fig. S5).

***Seismic signal of flood*:** While the northern lateral moraine collapse generated a clear seismic signal visible at stations >300 km distance, the seismic signal of the flood is less clear (fig. S5). GLOFs generally produce relatively high-frequency seismic noise (>1 Hz), which attenuates rapidly with distance from the source (*9*, *74*, *81*). At station LSA, we do not observe any potential flood signal following the moraine failure. At both KKN and EVN stations, we observe a small, but sustained increase in seismic noise at 1-3 Hz beginning around 18:30 UTC and lasting for at least 5.5 hours. The start and end of the signal are difficult to precisely constrain due to gaps in the EVN data. The similarity in the onset and envelope of the signal at the two stations suggests that both stations are recording the same seismic source. The observed signal has a higher magnitude and is visible at higher frequencies (up to 10 Hz) at EVN than at

KKN, indicating that the source of the signal is closer to EVN station (fig. S6). Thus, the observations are consistent with the GLOF as the source of the seismic signal; however, with only two stations at a very similar azimuth to the flow origin and path, they provide little information about the location of the observed signal. The lag between the moraine failure and the appearance of a potential GLOF signal is likely due to the evolution of flow properties and a related increase in seismic wave generation during GLOF propagation. While the GLOF was traversing only the low gradient and broad channel in the initial stages of the flood, it likely did not generate sufficient seismic noise to be detectable above the background noise at EVN and KKN stations (fig. S6). As the GLOF propagated through Teesta Valley, where it recruited coarse sediment from landslides and was contained in a narrow and steep channel, we expect the seismic noise generation to increase. Similarly, the disappearance of the signal at EVN and KKN stations does not necessarily represent the end of the GLOF, but rather a reduction in signal amplitude below the background noise at these stations. Seismic stations located closer to the flow path should provide a more complete record of the entire GLOF. Based on the seismic signals from the three stations, no earthquakes were observed immediately before the collapse.

4. Reconstruction of the GLOF cascade

The reconstruction of the 3 and 4 October 2023 South Lhonak GLOF cascade was conducted in two parts: first, reconstructing the sequence of events from the lake to a point 10 km downstream, where the arrival time at the Indo-Tibetan Border Police (ITBP) camp was known for model validation; and second, routing the cascade further downstream to Chungthang, located 67.5 km from the lake, where arrival times were further validated. For the first part, we back-calculate the South Lhonak GLOF process chain cascade by employing state-of-the-art mass movement modeling code r.avaflow (*82*, *83*). r.avaflow is a comprehensive GIS-based open-source computational framework for modeling mass movement from one or more release areas over the defined basal topography (*82*). It considers phase interactions along with erosion and deposition dynamics to provide a holistic understanding of GLOF dynamics (*82*). The mass movement model, r.avaflow, has served as an excellent model to construct well-documented mass movement events in the near past such as the 2021 rock-ice avalanche of Chamoli, Uttarakhand state in India (*27*) and the 2020 landslide-triggered GLOF event of Jinwuco in the southeast Tibetan Plateau (*84*). The model comprehensively simulates the complete sequence and interaction of processes involved in GLOF, beginning with avalanche or landslides, the dynamic interaction between the avalanche or landslides and lake water, impulse wave generation, overtopping at the frontal moraine, progressive erosion of the frontal moraine dam, and the downstream evolution of the resulting flow.

We used an enhanced version of the multi-phase flow model within the r.avaflow (*35*) considering two phases of matter. The solid phase (P_s; lateral and frontal moraines), and the fluid phase (P_L; lake water) (Fig. 3). Major initial model inputs and conditions include terrain data representing the basal topography, the release heights of the collapsed moraine (P_s), the bathymetry of the lake before the GLOF (P_L) [extracted from (*14*)], and friction and erosion parameters. To represent the terrain, we used high-resolution (4 m) pre-GLOF DEM from 2018 generated using SPOT 6 stereo images from 1st and 8th December 2018 (see section 1). We modeled the GLOF process cascade for the first 10 km downstream of SLL mainly to understand the initial process chain including the impact of the collapsed moraine, overtopping wave, erosion of the frontal moraine, water and sediment discharge immediately downstream of the lake, and arrival time at the ITBP camp located 10 km downstream of the lake (for validation). The model, set up with a mesh resolution of 30 m, was computationally efficient and reasonable for us to simulate various GLOF process chain scenarios with varied combinations of erosion coefficients and basal friction angles (fig. S7). Based on permafrost

assessment and possible presence of ice within the moraine (see section 7), we assumed the collapsed lateral moraine entering the lake and the frontal moraine that breached to be a mixture of two solid phases comprising of a rock component (75%) and ice component (25%) with an average density of 2300 kg m^{-3}. Assuming that flow at the initial stage is mostly dominated by the solid phase, we set the basal friction angle and internal friction angle at 10° and 25°, respectively. However, we acknowledge that there might be possible parameter value combinations other than what we determined here. All other parameters were held at default values largely following (*82*). We employed a simplified entrainment model, where the amount of entrainment is computed dynamically by multiplying the user-defined entrainment coefficient (CE) with the total momentum of the flow at the given raster cell and time step. We performed a total of 6 model runs by changing CE between $10^{-6.75}$ and $10^{-6.25}$ with a decrement of $10^{-0.10}$ and keeping basal and internal friction constant (fig. S7). The total process time to be simulated was set to 30 minutes, sufficient to cover the entire GLOF process chain for the first 10 km downstream of SLL. The model outputs were compared to various proxies to identify the best fit, including (i) seismic records that determined the timing of the moraine collapse (22:13:00 IST) (section 3; Fig. 3 and fig. S5), (ii) reported flood arrival time at the ITBP camp (22:30:00 IST; known by personal communication with ITBP officials), (iii) observed erosion of the frontal moraine [calculated from DoD; see section 1], (iv) observed GLOF inundation [(mapped using post-GLOF high -resolution Pléiades multispectral imagery (2 m spatial resolution) acquired on 21 – 31 October 2023] and (v) total observed volume released from the lake (~50×10^6 m^3). Here, the volume of water released during the GLOF was calculated based on the drop in lake level and the amount of moraine material that collapsed into the lake using the DoD (see section 1). We determined the level drop by averaging the change in water levels across the central part of the lake (28 meters). The change in lake volume post-GLOF, ~43×10^6 m^3, was calculated by averaging the lake's area before and after the GLOF, excluding the new area formed at the moraine collapse site (Fig. 1B and 1 C), and multiplying the level drop. Despite uncertainty about the depth at the new lake area formed after the northern lateral moraine collapse (area of 43,500 m^2), we estimated the water volume here to be between 0.5 to 1×10^6 m^3, resulting in a lost volume of 42 to 42.5×10^6 m^3 after subtracting this volume of the new lake area. Adding the volume of collapsed moraine (14.7×10^6 m^3), considering 70% debris (10.3×10^6 m^3), the total GLOF released volume is estimated between 52.3 and 52.8×10^6 m^3. If considering 60% debris in the collapsed moraine, the estimated volume would range from 50.8 to 51.3×10^6 m^3. Therefore, the total estimated GLOF released volume is calculated to be 50×10^6 m^3, with an uncertainty of $\pm 1.8 \times 10^6$ m^3. Among the results from six different GLOF process chain models, the model with an erosion coefficient (CE) of $10^{-6.25}$ showed good validation in terms of erosion of the frontal moraine, total GLOF released volume, and arrival time at the ITBP camp (Figs. 3A and 3B, fig. S7). The validated model was used to calculate discharge hydrographs of lake water (P_L) and eroded sediments of the frontal moraine (P_S) at a cross-section (CS-1) located immediately downstream of the lake (see Figs. 3A and 3D).

For the second part, we performed GLOF routing of the validated outflow hydrograph from part 1 above (fluid phase; P_L), calculated at CS-1 (at the frontal moraine). This routing extended downstream to Chungthang (CS-6; Fig. 3F), where the Teesta III hydropower (see Fig. 1 for location) is situated, spanning a distance of 67.5 km from the lake. To further validate the GLOF process chain modeled in part 1 above we compare the arrival time of the routed GLOF at Chungthang, where GLOF arrival timing was known (~ 00:35:00 IST on 4th October) (Fig. 3F). We employ the HEC-RAS (version 6.3.1) for hydrodynamic routing of the GLOF. HEC-RAS has been used widely for routing outburst floods from glacial lakes (*14*, *85*, *86*). A Manning's *n* value of 0.05 was considered based on previous GLOF modeling for SLL (*86*). A high-resolution (4 m) pre-GLOF DEM from 2018 generated using SPOT6 stereo images was used to represent the terrain along 67.5 km of the flow channel (see section 1, table 11). Considering the enormous volume eroded by the GLOF (233×10^6 m^3) with erosion depth reaching over 100 m resulting from undercutting and lateral erosion at places along the channel

till Chungthang (see Fig. 4 eroded volume and depth), it is challenging for the existing dynamic numerical model to handle such extreme cases. Therefore, we use only the fluid phase to obtain flow hydraulics, including flow depth, velocity, arrival time, and GLOF inundation. The outputs were compared with the observed arrival time at Chungthang and the observed inundation extents along the channel [mapped using post-GLOF high-resolution Pléiades multispectral imagery (2 m spatial resolution) acquired on 21 - 31 October 2023]. The reconstructed GLOF parameters show good agreement with the observed parameters including arrival time at Chungthang, and observed GLOF inundation along the flow path (Fig. 3F). We also see a good agreement between GLOF flow velocity and GLOF eroded volume, where higher erosion volumes are observed in regions with higher reconstructed flow velocity (fig. S36). We further calculate the time series of GLOF volume accumulated at Chungthang (Fig. 3F).

5. Comparison of the SLL GLOF and floods return-periods in the Upper Teesta valley

Peak discharges retrieved from SLL GLOF modeling suggest a rapid downstream attenuation of the outburst flood, leading to flattening of the flood hydrograph (Fig. 3). In general, GLOF peak discharges decrease in downstream direction at a rate primarily determined by river gradient and outflow volume (*47*). Conversely, peak discharges of meteorological floods commonly increase as drainage area grows downstream. As time series of discharge are unavailable, we calculated meteorological flood estimates using Dicken's formula adapted by UPIRI (Uttar Pradesh Irrigation Research Institute) for Himalayan rivers (*87*, *88*). In a water-only event, the SLL GLOF would have been equivalent to a 1-100 year meteorological flood at Chungthang, but owing to the huge volume of eroded sediment, the resulting total discharge was significantly higher. Our simulations show that the downstream stretch from SLL within which the water-only component of the 2023 event had higher discharges than meteorological floods (*9*, *24*) extends for ~ 50 km, depending on which return period is used to estimate flood discharge (Fig. S9). This comparison, however, neglects the role of sediment, in particular of large, transported boulders which exert a strong impact force on structures such as dams or bridge foundations (*89*). We observe that the peak discharge at the SLL outlet, which is 50,000 m^3s^{-1}, is towards the upper range of GLOF peak discharges estimated for the Eastern Himalaya (including Sikkim) *(3)*, indicating that the SLL GLOF is, in the historical context of this region, a rare event, equivalent to a return period exceeding 200 years.

6. Climatological drivers

In response to atmospheric warming and widespread glacial retreat, glacial lakes have been increasing in size and number globally (*90*), including in the Indian Himalayan region where South Lhonak, in particular, has been recognized as one of the most rapidly expanding lakes (*14*). While lake expansion and the destabilization of the lateral moraine wall are the most visible and direct climate-related drivers of the South Lhonak GLOF, we argue that the warming of permafrost has likely also played a decisive role (see section 7 for permafrost and related aspects).

6.1. Long-term trends in air temperature, precipitation, and modeled mass balances

No long-term climate data is available near South Lhonak Glacier; therefore, we analyzed ERA 5-Land reanalysis data using a 0.1° grid cell over the lake (*91*). Following well-established approaches in climatology, the Mann–Kendall non-parametric test was used in combination with Sen's slope estimator to calculate the trend and magnitude of any change over time. Over the 71-year (1951 – 2023), the annual mean temperature has warmed by around 0.56 °C (0.08

°C decade^{-1}) (fig. S10A). If only the monsoon/summer period [June, July, August, and September (JJAS)] is considered, the warming has been about half this rate, with a total warming of 0.28 °C (0.04 °C per decade^{-1}) (fig. S10B). Despite a moderate warming rate, the past four years have been characterized by anomalously warm summers – with 2020, 2022, and 2023 being the three warmest summers on record (*40*). While regional attribution studies are lacking, there is a strong anthropogenic signal seen in general warming over Asia since around the 1950's (*92*).

The mean annual precipitation is ~1150 mm w.e. over 1950-2023 with a maximum contribution of 48% during monsoon months (JJAS), followed by 28% from winter months (DJFM) and almost equal contributions of ~12% from pre- [May and June (MJ)] and post-monsoon [October and November (ON)] months. The maximum precipitation in summer months (MJJAS) suggests that South Lhonak Glacier is a summer-accumulation type glacier where accumulation and ablation occur concurrently. The mean long-term trend over mean annual precipitation sums suggested an increasing precipitation trend of ~21 mm w.e. over 1950-2013 (fig. S11). The mean total precipitation for JJAS is around 560 mm w.e. a^{-1} for the reference period of 1991 - 2020, with a statistically significant increasing trend of 8.6 mm decade^{-1} over 1951 - 2023. The 2023 monsoon was not remarkable, bringing near-average conditions (fig. S11).

The annual glacier-wide mass balances of South Lhonak Glacier were estimated by applying a temperature-index model (*93*) using the ERA5-Land data over 1950-2023 (fig. S12). This model is specially tailored for the data-scarce Himalayan region and has been successfully applied on several glaciers. For the South Lhonak Glacier, the model was calibrated using the threshold temperature and precipitation gradient against the available geodetic mass of -0.49 ± 0.05 m w.e. a^{-1} over 2000-2019 (*37*). The other model parameters (melt factors for snow and ice, threshold temperature for snow/rain, and temperature lapse rates) were adopted from Dokriani Bamak Glacier, which is a monsoon-dominated glacier similar to South Lhonak. The uncertainty in annual mass balances is estimated following the procedure in (*94*).

The mean annual glacier-wide mass balance was estimated to be -0.45 ± 0.33 m w.e. a^{-1}, corresponding to a cumulative mass loss of -33.16 ± 2.82 m w.e. over 1950-2023 (fig. S12). This mass wastage is similar to the observed wastage at the regional scale (*36*, *95*). An increased mass wastage of -0.52 ± 0.33 m w.e. a^{-1} was observed post-2000 compared to -0.42 ± 0.33 m w.e. a^{-1} over the pre-2000 period, which is in line with continued warming (fig. S12), the continued lake expansion (section 2.2) and the previous studies (*95*, *96*). The wastage (-0.58 ± 0.33 m w.e. a^{-1}) has increased significantly over the past four years, marked by unusually warm summers, with 2020, 2022, and 2023 being the three warmest summers on record (fig. S12).

6.2 Expansion of South Lhonak Lake

SLL was first noted as a small supraglacial lake in the 1960s (*12*, *14*), expanding dramatically from an area of around 0.15 km^2 in 1975, to 1.68 km^2, in September 2023, just before the outburst event on 3 October 2023 (fig. S19A; table S8). This equates to an average rate of areal expansion of 0.032 km^2 a^{-1} from 1975 – 2023. There has, however, been a notable doubling in the rate of expansion over the past 2 decades, from a rate of 0.023 km^2 a^{-1} over the period 1975 - 2004, compared to a rate of 0.046 km^2 a^{-1} since 2004. While the initial formation of glacial lakes is directly linked with the thinning and retreat of the parent glaciers from their little ice age moraines in response to 20th-century climate warming (*90*), calving processes and feedbacks decouple lake expansion from the climate signal over time (*97*, *98*). Hence, a continuous expansion of SLL is observed despite fluctuations in the overall long-term warming trend.

While this expansion has dramatically increased the water volume of SLL and thereby increased the potential volume and intensity of the outburst event, the lake expansion and associated glacial retreat have also played a major role in destabilizing the lateral moraine and eventual collapse of the northern (orographic left) moraine on 3 October 2023. Along this moraine, the lake has expanded, and the glacier retreated at an average rate of 47 m a^{-1} (fig. S19B). However, there was a period of enhanced calving and retreat at a rate of 130 m a^{-1} between 2010 and 2013, when the subsequent failure zone began to lose the buttressing support of the glacier and became exposed to lake water. It cannot be excluded that a subaqueous toe of the glacier extended further out into the lake and remained in contact with the base of the moraine within this zone for some years thereafter. Again between 2019 - 2020 and 2021 - 2022, glacial retreat/lake expansion along the 3 October 2023 failure zone exceeded 100 m a^{-1} (fig. S19B).

7. South Lhonak Lake: Permafrost and related aspects

We examine the permafrost occurrence pattern, thermal conditions, depth range, geotechnical properties, mechanical implications, hydraulic and hydrological effects, evolution over time, relationships with glaciers and lakes, and its impact on surface processes. This analysis is based on landform interpretations using high-resolution Maxar imageries (Google Earth), and approximate quantitative assessments.

Located at an elevation of 5200 m asl, permafrost is widespread at this altitude and in the surroundings of SLL. Permafrost exists in the wider surroundings of the lake (*45*, *46*) except for the bottom of deeper lakes, which cannot freeze through in wintertime, and of topographic depressions where thermally insulating snow accumulates in wintertime. The lateral moraines to both sides of the lake and the frontal moraine can be assumed to be perennially frozen.

The thermal condition of the permafrost can be inferred from the lowest viscous creep features (rock glaciers) in the valley below the lake (figs. S13 and S14) and by applying an environmental lapse rate of 0.6°C 100 m^{-1}. The mean near-surface permafrost temperature can be estimated at ~ -1 to -3°C for the sun-exposed northern lateral moraine (orographic left) and also the terminal moraine, and to ~ -3 to -6 °C for the southern lateral moraine (orographic right) in mountain shadow and oriented away from the sun.

The paleoclimate effect from atmospheric temperature rise since the end of the Little Ice Age causes a reduction of vertical heat flow and temperature gradient by about a factor of two to three down to 100 m depth (*99*). Within this depth range, a temperature gradient of about 1°C 100 m^{-1} can be assumed to estimate permafrost depths at unmeasured sites. Below 100 m depth, 2 - 3°C 100 m^{-1} is appropriate for high mountain sites with topographically reduced heat flow. Thus, permafrost at the sun-exposed northern lateral moraine (orographic left lateral moraine that collapsed on 3 October 2023) may reach tens of meters and even more than 100 meters deep (see below for glacier and lake influence). Permafrost depth at the southern moraine (orographic right) is estimated to be around 200 meters.

Subsurface freezing processes during millennial time scales and affecting materials containing frost-susceptible silts and fine sands – as commonly existing in morainic material – create large amounts of ice. Ice contents by volume often by far exceed the pore volume of the affected material in unfrozen condition. Ice segregation thereby produces massive lenses of ice from the millimeter to the meter scale. This ice-supersaturation or “excess ice” induces strong cohesion by tightly relating individual rock components and at the same time reduces internal friction by reducing rock-to-rock contacts. Similar properties are visible in the exposed scarp of the breached frontal moraine of the SLL (fig S1A).

Full saturation and supersaturation of originally porous/permeable debris and talus drastically reduces the hydraulic permeability of subsurface materials. Hydrologically, therefore, the

surroundings of SLL must be considered to be essentially impermeable except for the thin, decimeters to meters deep active layer, which thaws at the surface during the warm season. Besides seasonal water in the active layer, groundwater in such terrains exists as sub-permafrost groundwater at depth and in cases as intra-permafrost groundwater where unfrozen zones (taliks) exist.

Glaciers existing in continental-type climates and ending in permafrost regions are not temperate but polythermal to cold. Glaciers descending from very high altitudes can thereby have complex thermal structures (*100*, *101*). The highest firn area of South Lhonak glacier at about 7,000 m a.s.l is probably ~ -10 to -15°C cold. Due to percolating and refreezing meltwater, firn areas further down, closer to the mean altitude (equilibrium line) of the glacier near 6,000 m a.s.l. could be temperate but most of the largely impermeable ablation area at lower elevations could be cold again. The thick and active glacier may nevertheless be warm-based, at least in parts. Englacial temperatures of the glacier tongue must have had an impact on, or the interaction with the permafrost conditions in the lateral moraines. This influence is difficult to assess. It can, however, not be excluded that the margins of the glacier were – and up-valley of the calving front still are – frozen to the lateral moraines. Where the thickness of the debris cover on glaciers reaches or exceeds the thermally controlled active layer thickness, melting comes to a complete stop. Dead ice buried in permafrost can, therefore, be preserved for extended time periods but remains vulnerable to thermokarst processes where its debris cover becomes thinner than the local active layer depth. The breaching process at the lake outlet as a consequence of the collapse of the northern lateral moraine into the lake deeply eroded into massive, buried glacier ice embedded within the permafrost of the frontal moraine.

Complex interactions must take place between lake water and the permafrost in the moraines. Due also to the contact with the calving front of the glacier, the lake is likely to have a "polar" temperature regime (temperatures not reaching the density maximum at 4°C). Lake water is nevertheless likely to exert a slight warming effect to the lower parts of the lateral moraines. The lake bottom itself should presently be unfrozen and rather close to 0°C. The possibility cannot be excluded, however, that some permafrost remains from Little Ice Age conditions with a cold glacier tongue occupying the now developing lake may still exist underneath the lake bottom.

Ice-supersaturated frozen debris tends to slowly creep. Morphological indications of resulting ground movements – lavastream-like surface structures, freshly exposed debris at local detachment zones, and over-steepened/destabilized fronts [cf. (*102*)] – are indeed widespread around the SLL (figs. S13 and S14). Visible expressions of slow cumulative-coherent deformation exist at the outside of the southern (orographic right) moraine (fig.S15), at the terminal moraine (fig. S16), and in a somewhat less distinct way also from outside towards the northern lateral moraine (fig. S17). The SLL lateral moraine failure was a slow creep process of the frozen slope (northern lateral moraine) for many years (Fig. 2 and fig. S3), that eventually failed. Permafrost (see permafrost occurrence in Fig. S13 to S18) degradation is a slow process at depth, thus failures of permafrost slopes can happen irrespective of its timing in a day. Strong surface erosion at the over-steepened southern (orographic right) moraine, large deep-seated and rapidly moving block detachments at the northern (orographic left) moraine, and more diffuse instabilities at the site of the 3 October 2023 lateral moraine failure zone and up-valley of it can also be observed (fig. S18).

8. Short-term meteorological drivers

8.1 Data

(a) ERA5 and ERA5-Land

This study utilized the ERA5 and ERA5-Land reanalysis datasets, produced by the European Centre for Medium-Range Weather Forecasts (ECMWF) as part of the Copernicus Climate Change Service (C3S). ERA5, the fifth generation of ECMWF reanalysis, provides comprehensive global climate data by combining model output with a vast range of observations (*103*). ERA5-Land is a downscaled version of the ERA5 reanalysis, focusing specifically on land surface variables with enhanced spatial resolution (*104*). It employs the same underlying data assimilation and modeling framework as ERA5 but provides finer spatial detail, making it ideal for applications requiring high-resolution land surface information. For this study, we utilized variables such as geopotential, wind components, relative humidity, and specific humidity at the 700 hPa pressure level. Additionally, we used hourly precipitation data at 0.25° horizontal resolution. The data utilized spanned from 28 September to 8 October 2023.

(b) IMERG

We use Version 07B of the Integrated Multi-satellitE Retrievals for GPM (IMERG) dataset provided by NASA. This version represents the latest advancement in global precipitation estimation, incorporating the GPROF2021 algorithm to compute precipitation estimates from multiple satellite passive microwave (PMW) sensors within the GPM constellation. The data is intercalibrated to the GPM Combined Ku Radar-Radiometer Algorithm (CORRA) product and is provided in high-resolution half-hourly grids of approximately 0.1° × 0.1° (*105*, *106*). Here, we utilize the "GPM IMERG Final Precipitation L3 Half Hourly 0.1 × 0.1° V07 (GPM 3IMERGHH)" dataset from 28 September to 8 October 2023.

(c) CPC Global Precipitation V1.0 RT

We use the CPC Global Precipitation V1.0 Real-Time (RT) dataset, provided by the NOAA Climate Prediction Center (CPC), to analyze global precipitation patterns (*107*). The CPC Global Precipitation V1.0 RT dataset combines satellite observations and in situ gauge measurements to offer real-time precipitation estimates, enhancing both spatial and temporal coverage. This results in a reliable and consistent precipitation product. Our study specifically utilizes data from 28 September to 8 October 2023.

(d) Rain Gauge Data

We use hourly rainfall data for September and October 2023 from the gauge located at Lachen in Sikkim and daily accumulated rainfall from Dalia in Bangladesh. The rainfall data at Lachen was collected personally during fieldwork from the AWS installed at the location (27.7296°N, 88.5471°E) (by a co-author). The AWS was installed as a part of the funding received by the Department of Science and Technology, Government of India. The rain gauge data for Dalia station was procured from the Bangladesh Water Development Board (BWDB).

8.2 Methods

8.2.1 Statistical Parameters

We use several statistical parameters: (i) mean station rainfall, (ii) mean ERA5 rainfall, (iii) mean absolute error, and (iv) root mean square error, to quantify the nature of rainfall, uncertainties, and the accuracy of different rainfall datasets with respect to the rain gauge-based data (*108*) (figs. S24 and S25).

8.2.2 Correlation Analysis

To ascertain the similarity in daily variability and trends of precipitation among different rainfall datasets (section 8.1), we use the Pearson correlation coefficient, Spearman Correlation Coefficient, and pattern correlation (figs. S24D, S25D, and S27). The Pearson Correlation Coefficient measures the linear relationship between datasets, indicating how well the variation in one dataset predicts the variation in another (*109*). It assumes linearity, and normal distribution, and is sensitive to outliers. The Spearman Correlation Coefficient assesses rank-based relationships through a monotonic function, making it useful for non-linear trends (*110*). It is less sensitive to outliers and does not assume linearity or normal distribution. Pattern correlation evaluates the similarity in spatial distribution patterns of precipitation between datasets [c.f (*111*)]. It determines how well the spatial arrangement of rainfall intensity matches between datasets, reflecting how similarly they capture spatial variability. High pattern correlation indicates similar spatial features, while low correlation suggests discrepancies (figs. S24 and S25; table S9). To test the significance of the correlation coefficient, we use a t-test [(*112*), table S9). For analyzing the frequency components of the rainfall time series, we apply the Discrete Fourier Transform and subsequently calculate the probability density function for the rainfall data.

8.2.3 Interpolation Methods

We used several approaches to accurately interpolate rainfall from gridded data to specific latitude-longitude coordinates. Since rainfall can vary greatly in mountainous regions, we aimed to reduce uncertainty and obtain a representative rainfall trend for the location by averaging data from an area around the nearest grid point. The interpolation methods we employed include (i) Inverse Distance Weighted Average (IDWAVG), (ii) Bilinear Interpolation (BILINR), (iii) Nearest Neighbourhood Grid Approximation (NGRID), and (iv) Area Average Rainfall Approximation (AARA) (fig. S23).

8.2.4 Pre-Processing of the Datasets

To compare datasets with varying temporal frequencies and accumulation intervals, we standardized them to a common reference. Specifically, Lachen rainfall data is provided as hourly accumulations (mm h^{-1}) on the IST time axis, while satellite rainfall data (IMERG) is provided as half-hourly accumulations (mm h^{-1}) on the UTC axis. The ERA5 and ERA5-Land data are also in hourly accumulations (mm h^{-1}) but on the UTC axis. Dalia station rainfall data in Bangladesh is available as daily accumulations ending at 9:00 IST, and CPC-NOAA rainfall data is available as daily accumulations ending at 00:00 UTC.

Since we cannot modify the provided daily accumulation intervals, we calculated the daily accumulations for ERA5, ERA5-Land, and IMERG to end at 9:00 IST to ensure consistency, enabling comparison with the Dalia station data. To compare with the CPC-NOAA rainfall, which is already in daily accumulations, we calculated the daily accumulation for Lachen and over SLL as 24-hourly accumulations ending at 00:00 UTC for ERA5, ERA5-Land, IMERG,

and Lachen station data. This approach ensures consistency and accuracy in comparing the datasets.

Further, we noted that the correlation of Lachen daily rainfall with the nearest grid points of ERA5 and ERA5-Land was only 0.37 and 0.38, respectively, which were not statistically significant at the 95% confidence level under a two-tailed Student's t-test. To achieve more accurate assignments, various interpolation methods were used. For IDWAVG, the correlation for ERA5 increased to 0.70 with 98% confidence, while the correlation with ERA5-Land increased to 0.55. For BILINR, the correlations were 0.81 and 0.53, which were significant at the 99% and 90% confidence levels, respectively. For a 1.2° × 1.2° area average centered around the station, the correlations were 0.85 and 0.84, both significant at 99% confidence. Thus, we believe that in complex topography, where there is significant heterogeneity in rainfall, the average rainfall around the grid point better represents the trends observed at the station.

8.2.5 Rainfall Data Intercomparison and Reliability of ERA5

To understand the prevailing meteorological conditions—such as winds, pressure, and moisture—during the 3-4 October GLOF cascade, we used ERA5 reanalysis datasets. ERA5 is one of the most widely used reanalysis datasets, available at very high temporal (hourly) and spatial (0.25°) resolution with significant accuracy (*103*, *104*).

To quantify the differences and validate the use of ERA5 data as a proxy for observed data in exploring the dynamical conditions during the GLOF cascade event, we first compared various characteristics of daily ERA5 rainfall with ground stations and satellite rainfall data (IMERG). This comparison was conducted to ensure that ERA5 satisfactorily captures the rainfall cycle and trends over stations, as well as spatial patterns, even if it does not exactly replicate the rainfall amount. The rainfall trends for one station in Bangladesh (Dalia) and one in Sikkim (Lachen, which is nearest to SLL, approximately 30 km southeast) are shown in fig. S22. Similar to the gauge daily rainfall, both ERA5-Land and ERA5 exhibit a largely increasing trend in rainfall during 1-5 October, with a peak around 3-4 October at the Lachen station (Sikkim) and around 4-5 October at the Dalia station (Bangladesh) (Fig. S22).

As shown in table S9, both the Pearson correlation between Lachen and Dalia gauging stations and ERA5-Land and ERA5 remains in the range of 0.74 to 0.85 with daily station rainfall data during 1-8 October 2023 (fig. S23D). The Spearman correlation coefficient is calculated to be 0.84 and 0.85 for Lachen and Dalia respectively (fig. S24D). This indicates that largely ERA5 compares well with the daily rainfall trends and also the amounts over the gauging stations. A similar correlation range has been observed between ERA5 and IMERG satellite daily rainfall (fig. S27). Additionally over Sikkim, ERA5 and ERA5-Land perform better compared to satellite rain, likely because of the complex terrain, while over land, ERA5 and satellite both are comparable or IMERG show better results than reanalysis-based precipitation, consistent with findings from previous studies (*113–115*) which also suggested that ERA5 rainfall outperforms satellite data in complex terrains but may perform worse over plains and during convective storms (*116*). Further, the pattern correlation coefficients of ERA5 with IMERG from 28 September to 8 October 2023 remain near 0.7 (fig. S27). This indicates that ERA5 rainfall data not only exhibits similar temporal variability as station data but also the spatial patterns of rainfall match satisfactorily. Additionally, for SLL, where no rain gauge is available, we used interpolated rainfall data from nearby grids as representative from the gridded rainfall datasets: ERA5, ERA5-Land, CPC, and IMERG. All datasets are in agreement with the increasing trend of rainfall over SLL during 1-5 October, except IMERG which shows an increasing trend up to 2 October, then decreasing, and increasing again from 3-6 October (fig.

S23). This difference is expected as previous studies suggest that satellite rainfall measurements are less accurate over complex terrain (*114*).

Further statistical analysis shows that ERA5 effectively captures both the Fourier spectral peaks and the probability density of rainfall distribution when compared to station data (figs. S24B and S25B). This suggests ERA5 is proficient in representing different modes of variability and accurately reflects rainfall characteristics, including the probabilities of extreme or light rainfall events. Additionally, mean rainfall from ERA5 closely matches the observed data at Lachen (in Sikkim), but in Bangladesh (Dalia), ERA5 reports a higher mean rainfall compared to station data.

Given that ERA5 largely captures the onset, strength, temporal, and spatial variations of rain events, we can rely on it for analyzing other atmospheric fields responsible for triggering the rainfall event. All the above analyses, along with guidance from previous works (*103*), clearly suggest that ERA5 dynamical fields are robust for further investigation in unraveling the dynamical fields responsible for the heavy rainfall and floods over Northeast India during 3–4 October 2023.

8.2.6 Meteorological Conditions During the October 2023 Sikkim Flood

Analysis of the geopotential height at 700 hPa isobaric surface, IMERG daily rainfall data, and specific humidity at 700 hPa (Fig. 4 and fig. S26) reveals that the October 2023 Sikkim flood was significantly influenced by the proximity of a low-pressure system or cyclonic circulation located south and southeast of Sikkim from 28 September to 6 October. As this system moved over West Bengal and Bangladesh on 3 and 4 October, it triggered substantial increases in heavy rainfall along its path, impacting most parts of northeast India, including West Bengal, Sikkim, and Bangladesh.

A detailed daily comparison of moisture, circulation, rainfall, and pressure fields indicates that when the weather system was near the Myanmar coast on 28 September 2023, the weather over northeast India was mostly clear. As the system moved northwest into the northern Bay of Bengal and reached the state of Odisha in India during 29-30 September, a significant increase in moisture content and rainfall was observed over the states of Odisha, Bihar, Jharkhand, and Bengal. Notably, after 1 October 2023, the system ceased its westward movement and began drifting northeast towards Bengal (Fig. 4 and fig. S26). During this eastward movement, it triggered heavy rainfall over its eastern sector, where northward winds dominated. The interaction of these northerly winds with the Himalayan topography likely enhanced orographic rainfall over the Sikkim region.

As the system advanced eastward, heavy rainfall was recorded in several places in Bangladesh from 5-7 October (Fig. 4). Once the system moved past Bengal, rainfall over Sikkim significantly decreased, indicating that the flood event was closely modulated by this low-pressure system. Additionally, persistent rainfall occurred in southern Sikkim before the lake burst event on the night of 3 October. As the rainfall system moved from south to north due to the northward background winds of the low-pressure system, conditions deteriorated further. The lake water flowed through regions already affected by previous rainfall, exacerbating the situation.

In essence, the heavy rainfall and subsequent floods in Sikkim, Bengal, and Bangladesh were directly influenced by the low-pressure monsoon system that originated in the Bay of Bengal. This system recurved towards Sikkim during 2-4 October 2023, modulating the cascade of flood and landslide events.

9. Mapping exposed elements

We mapped elements exposed to the 2023 SLL GLOF and areas impacted by triggered landslides along the Teesta River in India and Bangladesh (tables S1-S2 and S4-S7). We focused on quantifying the change of exposure to buildings in the past decade and the totals of buildings were surveyed for two points in time (2013 and 2023) (Fig. 7A; tables S1 and S4). The pre-event building footprints for May 2023 (v3) are sourced from (*117*, *118*). For data accuracy of buildings refer to (*117*, *118*). Taking the 2023 building dataset as baseline, we employed 2011-2014 high-resolution Maxar imagery (Google Earth) to identify buildings that existed at that time.

Bridges (Fig. 7C and fig. S39, table S6) and roadways (fig. S32; tables S2 and S7) impacted by GLOF cascade and triggered landslides were mapped using 0.7 m resolution post-event Pléiades imagery (acquired on 24, 29, and 31 October and 5 November 2023) for the first 67.5 km downstream of the lake. The PlanetScope imagery (3 m resolution) from 9 October to 24 October 2023 were utilized further downstream (fig. S39). The existing bridges (pre-GLOF) were mapped using high-resolution Maxar imagery from Google Earth. Road networks for the states of Sikkim, West Bengal, and Bangladesh obtained from OpenStreetMaps (*119*) were overlaid on the post-event imagery to extract the impacted roads both by flood and triggered landslides. We used post-flood PlanetScope imagery (acquired on 31 July, 3 September, 16 September, and 28 September 2023) for mapping the areal extent of impacted agricultural land (Fig. 7B).

The limitations/uncertainties resulted from the size of the study area (hundreds of km along Teesta River), the number of exposed elements (tens of thousands), and the data used. Our analysis of exposure change considers only two points in time (2013 and 2023 before the GLOF) and cannot capture any changes with finer temporal resolution, e.g., exposure changes associated with damages caused by seasonal floods. Rather than going into details, we aim to provide elementary statistics to document the changing number/area of exposed elements between a decade before and shortly before the 2023 GLOF. Further, it is important to mention that the location of elements within the 2023 GLOF impact area does not necessarily imply that these elements were damaged or destroyed. Therefore, we primarily report changing exposure of buildings rather than conclusively stating the extent of damages associated with the 2023 GLOF, unless explicitly known (e.g. as for bridges).

10. Transboundary implications and sediment transport

To evaluate the transboundary implication of the flood cascade we collected gauged data from the BWDB for water level in the Teesta River, rainfall, and sediment discharge (fig. S41). The data was collected for the Dalia station (26.1758 N, 89.0505 E) located in Dimla Upazila (an administrative region or sub-district) of the Nilphamari District, the first station to encounter the floods along the Teesta's path in Bangladesh (see Fig.1 for location). We analyzed sediment discharge available at 7-day temporal intervals from 17 September 2023 to 29 October 2023. Daily water level and rainfall data were analyzed for this period. BWDB employs a Binckley Silt Sampler, a cylindrical device with a uniform opening, for collecting suspended sediment samples (*120*). This instantaneous sampler is lowered into the water column and triggered at specific depths (0.2 and 0.8 of the total depth) by pulling a wire. At each depth, 1000 ml of water is collected. The samples undergo a two-step process to determine the total suspended sediment concentration:

Coarse Sediment Analysis: Samples are allowed to settle for 100 seconds. The settled portion (coarse sediment) is then collected and analyzed to determine its concentration per liter volume using a dispersion method.

Fine Sediment Analysis: A separate sample, collected from the top of the water column for all verticals, is sent for analysis. The analysis includes filtration techniques to obtain the average concentration of finer sediment particles. The total suspended sediment concentration for each vertical is calculated by adding the concentration of coarse sediment (obtained from on-site analysis) to the average concentration of fine sediment. The sediment transport load is calculated and expressed in kilograms per second (kg s^{-1}).

Flood impacts: The collapse of a ~90 m high embankment in Gangachara upazila (administrative division) of Rangpur district was reported to have destroyed 11 houses in the Paschim Isli village along the banks of the Teesta River (*121*). Immediately downstream of this region, in the Char Isli area of the Gangachara upazila (Rangpur district), the flood inundation and erosion destroyed several houses (fig. S41E). The flood washed away 73 houses while temporarily displacing 33,000 people in the five districts including Rangpur, Lalmonirhat, Kurigram, Gaibandha, and Nilphamari. At Rajarhat in Kurigram district, the collapse of another embankment was reported (*121*). Significant asset losses were recorded in Lalmonirhat, Kurigram, and Rangpur due to the submersion of residential and agricultural properties (*122*). In these districts, 21 unions faced inundation, with houses submerged under up to about 1 m of water and extensive agricultural lands affected. High rainfall was recorded in Bangladesh on 5 October 2023, a day after the GLOF cascade entered Bangladesh (see Fig. 4B; section 8.3.6). The impacts in Bangladesh were due to a combined effect of the GLOF cascade on 4 October and the intense rainfall that followed immediately on 5 October 2023.

References

1. S. D. Richardson, J. M. Reynolds, An overview of glacial hazards in the Himalayas. *Quat. Int.* **65**–**66**, 31–47 (2000).

2. J. L. Carrivick, F. S. Tweed, A global assessment of the societal impacts of glacier outburst floods. *Glob. Planet. Change* **144**, 1–16 (2016).

3. G. Veh, O. Korup, A. Walz, Hazard from Himalayan glacier lake outburst floods. *Proc. Natl. Acad. Sci.* **117**, 907–912 (2020).

4. G. Zheng, S. K. Allen, A. Bao, J. A. Ballesteros-Cánovas, M. Huss, G. Zhang, J. Li, Y. Yuan, L. Jiang, T. Yu, W. Chen, M. Stoffel, Increasing risk of glacial lake outburst floods from future Third Pole deglaciation. *Nat. Clim. Chang.* **11**, 411–417 (2021).

5. C. Taylor, T. R. Robinson, S. Dunning, J. Rachel Carr, M. Westoby, Glacial lake outburst floods threaten millions globally. *Nat. Commun.* **14**, 487 (2023).

6. M. Geertsema, B. Menounos, G. Bullard, J. L. Carrivick, J. J. Clague, C. Dai, D. Donati, G. Ekstrom, J. M. Jackson, P. Lynett, M. Pichierri, A. Pon, D. H. Shugar, D. Stead, J. Del Bel Belluz, P. Friele, I. Giesbrecht, D. Heathfield, T. Millard, S. Nasonova, A. J. Schaeffer, B. C. Ward, D. Blaney, E. Blaney, C. Brillon, C. Bunn, W. Floyd, B. Higman, K. E. Hughes, W. McInnes, K. Mukherjee, M. A. Sharp, The 28 November 2020 Landslide, Tsunami, and Outburst Flood – A Hazard Cascade Associated With Rapid Deglaciation at Elliot Creek, British Columbia, Canada. *Geophys. Res. Lett.* **49**, e2021GL096716 (2022).

7. P. Cui, C. Dang, Z. Cheng, K. M. Scott, Debris Flows Resulting From Glacial-Lake Outburst Floods in Tibet, China. *Phys. Geogr.* **31**, 508–527 (2010).

8. S. G. Evans, K. B. Delaney, N. M. Rana, "Chapter 16 - The occurrence and mechanism of catastrophic mass flows in the mountain cryosphere" in *Hazards and Disasters Series*, W. Haeberli, C. Whiteman. (Eds.), Snow and Ice-Related Hazards, Risks and Disasters, (Second Edition), Eds. (Elsevier, 2021; https://www.sciencedirect.com/science/article/pii/B9780128171295000044), pp. 541–596.

9. K. L. Cook, C. Andermann, F. Gimbert, B. R. Adhikari, N. Hovius, Glacial lake outburst floods as drivers of fluvial erosion in the Himalaya. *Science (80-.).* **362**, 53–57 (2018).

10. A. Sattar, U. K. Haritashya, J. S. Kargel, A. Karki, Transition of a small Himalayan glacier lake outburst flood to a giant transborder flood and debris flow. *Sci. Rep.* **12**, 12421 (2022).

11. P. Mani, S. Allen, S. G. Evans, J. S. Kargel, M. Mergili, D. Petrakov, M. Stoffel, Geomorphic Process Chains in High-Mountain Regions—A Review and Classification Approach for Natural Hazards Assessment. *Rev. Geophys.* **61**, e2022RG000791 (2023).

12. B. K. Govindha Raj, V. K. Kumar, R. S.N., Remote sensing-based inventory of glacial lakes in Sikkim Himalaya: semi-automated approach using satellite data. *Geomatics, Nat. Hazards Risk* **4**, 241–253 (2013).

13. S. Aggarwal, S. C. Rai, P. K. Thakur, A. Emmer, Inventory and recently increasing GLOF susceptibility of glacial lakes in Sikkim, Eastern Himalaya. *Geomorphology* **295**, 39–54 (2017).

14. A. Sattar, A. Goswami, A. V. Kulkarni, A. Emmer, U. K. Haritashya, S. Allen, H. Frey, C. Huggel, Future Glacial Lake Outburst Flood (GLOF) hazard of the South Lhonak Lake, Sikkim Himalaya. *Geomorphology* **388**, 107783 (2021).

15. N. Islam, P. P. Patel, Inventory and GLOF hazard assessment of glacial lakes in the Sikkim Himalayas, India. *Geocarto Int.* **37**, 3840–3876 (2022).

16. A. Singh, V. Anand, K. H. V Durga Rao, S. R. P., P. Chauhan, Unveiling the catastrophic landslide-induced flash flood in Teesta River, Sikkim: insight from South Lhonak Glacial Lake. *Landslides*, doi: 10.1007/s10346-024-02378-7 (2024).

17. T. Zhang, W. Wang, B. An, A massive lateral moraine collapse triggered the 2023 South Lhonak Lake outburst flood, Sikkim Himalayas. *Landslides*, doi: 10.1007/s10346-024-02358-x (2024).

18. SSDMA, "Post Disaster Needs Assessment, Glacial Lake Outburst Flood Sikkim" (2023); https://ssdma.nic.in/Uploads/PdfFiles/SIKKIM%20PDNA.pdf

19. NRSC, https://www.isro.gov.in/Satellite_Insights_Expanding_Glacial_Lakes_Indian_Himalayas.html (2024).

20. D. Li, X. Lu, D. E. Walling, T. Zhang, J. F. Steiner, R. J. Wasson, S. Harrison, S.

Nepal, Y. Nie, W. W. Immerzeel, D. H. Shugar, M. Koppes, S. Lane, Z. Zeng, X. Sun, A. Yegorov, T. Bolch, High Mountain Asia hydropower systems threatened by climate-driven landscape instability. *Nat. Geosci.* **15**, 520–530 (2022).

21. R. A. Vaidya, D. J. Molden, A. B. Shrestha, N. Wagle, C. Tortajada, The role of hydropower in South Asia's energy future. *Int. J. Water Resour. Dev.* **37**, 367–391 (2021).

22. S. A. Dunning, N. J. Rosser, D. N. Petley, C. R. Massey, Formation and failure of the Tsatichhu landslide dam, Bhutan. *Landslides* **3**, 107–113 (2006).

23. S. K. Allen, P. Rastner, M. Arora, C. Huggel, M. Stoffel, Lake outburst and debris flow disaster at Kedarnath, June 2013: hydrometeorological triggering and topographic predisposition. *Landslides* **13**, 1479–1491 (2016).

24. W. Schwanghart, R. Worni, C. Huggel, M. Stoffel, O. Korup, Uncertainty in the Himalayan energy–water nexus: estimating regional exposure to glacial lake outburst floods. *Environ. Res. Lett.* **11**, 74005 (2016).

25. W. Schwanghart, M. Ryan, O. Korup, Topographic and Seismic Constraints on the Vulnerability of Himalayan Hydropower. *Geophys. Res. Lett.* **45**, 8985–8992 (2018).

26. Y. Nie, H. D. Pritchard, Q. Liu, T. Hennig, W. Wang, X. Wang, S. Liu, S. Nepal, D. Samyn, K. Hewitt, X. Chen, Glacial change and hydrological implications in the Himalaya and Karakoram. *Nat. Rev. Earth Environ.* **2**, 91–106 (2021).

27. D. H. Shugar, M. Jacquemart, D. Shean, S. Bhushan, K. Upadhyay, A. Sattar, W. Schwanghart, S. McBride, M. V. W. de Vries, M. Mergili, A. Emmer, C. Deschamps-Berger, M. McDonnell, R. Bhambri, S. Allen, E. Berthier, J. L. Carrivick, J. J. Clague, M. Dokukin, S. A. Dunning, H. Frey, S. Gascoin, U. K. Haritashya, C. Huggel, A. Kääb, J. S. Kargel, J. L. Kavanaugh, P. Lacroix, D. Petley, S. Rupper, M. F. Azam, S. J. Cook, A. P. Dimri, M. Eriksson, D. Farinotti, J. Fiddes, K. R. Gnyawali, S. Harrison, M. Jha, M. Koppes, A. Kumar, S. Leinss, U. Majeed, S. Mal, A. Muhuri, J. Noetzli, F. Paul, I. Rashid, K. Sain, J. Steiner, F. Ugalde, C. S. Watson, M. J. Westoby, A massive rock and ice avalanche caused the 2021 disaster at Chamoli, Indian Himalaya. *Science (80-.).* **373**, 300–306 (2021).

28. M. A. Gleyzes, L. Perret, P. Kubik, PLEIADES SYSTEM ARCHITECTURE AND MAIN PERFORMANCES. *Int. Arch. Photogramm. Remote Sens. Spat. Inf. Sci.* **XXXIX-B1**, 537–542 (2012).

29. D. Shean, High Mountain Asia 8-meter DEM Mosaics Derived from Optical Imagery, Version 1 [Data Set], *NASA National Snow and Ice Data Center Distributed Active Archive Center*. (2017). https://doi.org/10.5067/KXOVQ9L172S2.

30. M. Van Wyk de Vries, A. D. Wickert, Glacier Image Velocimetry: an open-source toolbox for easy and rapid calculation of high-resolution glacier velocity fields. *Cryosph.* **15**, 2115–2132 (2021).

31. M. Van Wyk de Vries, K. Arrell, G. K. Basyal, A. L. Densmore, A. Dunant, E. L. Harvey, G. K. Jimee, M. E. Kincey, S. Li, D. Singh Pujara, R. Shrestha, N. J. Rosser, S. J. Dadson, Detection of slow-moving landslides through automated monitoring of surface deformation using Sentinel-2 satellite imagery. *Earth Surf. Process. Landforms*

49, 1397–1410 (2024).

32. L. Toney, K. E. Allstadt, lsforce: A Python-based single-force seismic inversion framework for massive landslides. *Seismol. Res. Lett.* **4**, 2610–2626 (2021).

33. C. E. A. Allstadt, K.E., Toney, L., lsforce (Version 1.1) [Source code], *U.S. Geological Survey Software Release* (2023). https://doi.org/https://www.google.com/url?q=https://doi.org/10.5066/P9CR20KW&sa=D&source=docs&ust=1722328626094457&usg=AOvVaw1kObXBwwL9v_w861C9U7MT.

34. NDMA, "Mission report of GLOF Risk Assessment & Installation of AWS in Sikkim" (2024); https://www.ndma.gov.in/sites/default/files/PDF/Reports/GLOF_Mission_Report_NDMA.pdf.

35. S. P. Pudasaini, M. Mergili, A Multi-Phase Mass Flow Model. *J. Geophys. Res. Earth Surf.* **124**, 2920–2942 (2019).

36. M. F. Azam, P. Wagnon, E. Berthier, C. Vincent, K. Fujita, J. S. Kargel, Review of the status and mass changes of Himalayan-Karakoram glaciers. *J. Glaciol.* **64**, 61–74 (2018).

37. R. Hugonnet, R. McNabb, E. Berthier, B. Menounos, C. Nuth, L. Girod, D. Farinotti, M. Huss, I. Dussaillant, F. Brun, A. Kääb, Accelerated global glacier mass loss in the early twenty-first century. *Nature* **592**, 726–731 (2021).

38. J. L. Carrivick, F. S. Tweed, J. L. Sutherland, J. Mallalieu, Toward Numerical Modeling of Interactions Between Ice-Marginal Proglacial Lakes and Glaciers. *Front. Earth Sci.* **8** (2020).

39. E. Lee, J. L. Carrivick, D. J. Quincey, S. J. Cook, W. H. M. James, L. E. Brown, Accelerated mass loss of Himalayan glaciers since the Little Ice Age. *Sci. Rep.* **11**, 24284 (2021).

40. W. M. O. (WMO), "State of the Global Climate 2023" (Geneva, 2024); https://library.wmo.int/idurl/4/68835.

41. W. Haeberli, B. Hallet, L. Arenson, R. Elconin, O. Humlum, A. Kääb, V. Kaufmann, B. Ladanyi, N. Matsuoka, S. Springman, D. V. Mühll, Permafrost creep and rock glacier dynamics. *Permafr. Periglac. Process.* **17**, 189–214 (2006).

42. J. L. Carrivick, T. Heckmann, Short-term geomorphological evolution of proglacial systems. *Geomorphology* **287**, 3–28 (2017).

43. A. Kellerer-Pirklbauer, X. Bodin, R. Delaloye, C. Lambiel, I. Gärtner-Roer, M. Bonnefoy-Demongeot, L. Carturan, B. Damm, J. Eulenstein, A. Fischer, L. Hartl, A. Ikeda, V. Kaufmann, K. Krainer, N. Matsuoka, U. Morra Di Cella, J. Noetzli, R. Seppi, C. Scapozza, P. Schoeneich, M. Stocker-Waldhuber, E. Thibert, M. Zumiani, Acceleration and interannual variability of creep rates in mountain permafrost landforms (rock glacier velocities) in the European Alps in 1995–2022. *Environ. Res. Lett.* **19**, 34022 (2024).

44. S. Gruber, Derivation and analysis of a high-resolution estimate of global permafrost

zonation. *Cryosph.* **6**, 221–233 (2012).

45. J. Obu, S. Westermann, A. Bartsch, N. Berdnikov, H. H. Christiansen, A. Dashtseren, R. Delaloye, B. Elberling, B. Etzelmüller, A. Kholodov, A. Khomutov, A. Kääb, M. O. Leibman, A. G. Lewkowicz, S. K. Panda, V. Romanovsky, R. G. Way, A. Westergaard-Nielsen, T. Wu, J. Yamkhin, D. Zou, Northern Hemisphere permafrost map based on TTOP modelling for 2000–2016 at 1 km2 scale. *Earth-Science Rev.* **193**, 299–316 (2019).

46. P. Baral, M. A. Haq, Spatial prediction of permafrost occurrence in Sikkim Himalayas using logistic regression, random forests, support vector machines and neural networks. *Geomorphology* **371**, 107331 (2020).

47. V. M. Ponce, T. Ahmad, S. A. V., Dam-Breach Flood Wave Propagation Using Dimensionless Parameters. *J. Hydraul. Eng.* **129**, 777–782 (2003).

48. D. W. Burbank, J. Leland, E. Fielding, R. S. Anderson, N. Brozovic, M. R. Reid, C. Duncan, Bedrock incision, rock uplift and threshold hillslopes in the northwestern Himalayas. *Nature* **379**, 505–510 (1996).

49. D. Farinotti, M. Huss, J. J. Fürst, J. Landmann, H. Machguth, F. Maussion, A. Pandit, A consensus estimate for the ice thickness distribution of all glaciers on Earth. *Nat. Geosci.* **12**, 168–173 (2019).

50. S. Harrison, J. S. Kargel, C. Huggel, J. Reynolds, D. H. Shugar, R. A. Betts, A. Emmer, N. Glasser, U. K. Haritashya, J. Klimeš, L. Reinhardt, Y. Schaub, A. Wiltshire, D. Regmi, V. Vil\'\imek, Climate change and the global pattern of moraine-dammed glacial lake outburst floods. *Cryosph.* **12**, 1195–1209 (2018).

51. O. Korup, J. J. Clague, Natural hazards, extreme events, and mountain topography. *Quat. Sci. Rev.* **28**, 977–990 (2009).

52. S. G. Heidel, The progressive lag of sediment concentration with flood waves. *Eos, Trans. Am. Geophys. Union* **37**, 56–66 (1956).

53. J. L. Carrivick, Dam break – Outburst flood propagation and transient hydraulics: A geosciences perspective. *J. Hydrol.* **380**, 338–355 (2010).

54. M. Guan, J. L. Carrivick, N. G. Wright, P. A. Sleigh, K. E. H. Staines, Quantifying the combined effects of multiple extreme floods on river channel geometry and on flood hazards. *J. Hydrol.* **538**, 256–268 (2016).

55. K. M. Scott, J. W. Vallance, N. Kerle, J. Luis Macías, W. Strauch, G. Devoli, Catastrophic precipitation-triggered lahar at Casita volcano, Nicaragua: occurrence, bulking and transformation. *Earth Surf. Process. Landforms* **30**, 59–79 (2005).

56. J. W. Vallance, "Lahars: Origins, Behavior and Hazards BT - Advances in Debris-flow Science and Practice" M. Jakob, S. McDougall, P. Santi, Eds. (Springer International Publishing, Cham, 2024; https://doi.org/10.1007/978-3-031-48691-3_12), pp. 347–382.

57. T. de Haas, B. W. McArdell, W. Nijland, A. S. Åberg, J. Hirschberg, P. Huguenin, Flow and Bed Conditions Jointly Control Debris-Flow Erosion and Bulking. *Geophys. Res. Lett.* **49**, e2021GL097611 (2022).

58. Y. Nie, Q. Deng, H. D. Pritchard, J. L. Carrivick, F. Ahmed, C. Huggel, L. Liu, W. Wang, M. Lesi, J. Wang, H. Zhang, B. Zhang, Q. Lü, Y. Zhang, Glacial lake outburst floods threaten Asia's infrastructure. *Sci. Bull.* **68**, 1361–1365 (2023).

59. M. Carey, G. McDowell, C. Huggel, B. Marshall, H. Moulton, C. Portocarrero, Z. Provant, J. M. Reynolds, L. Vicuña, "Chapter 8 - A socio-cryospheric systems approach to glacier hazards, glacier runoff variability, and climate change" in *Hazards and Disasters Series*, W. Haeberli, C. Whiteman. (Eds.), Snow and Ice-Related Hazards, Risks and Disasters, (Second Edition), Eds. (Elsevier, 2021; https://www.sciencedirect.com/science/article/pii/B9780128171295000184), pp. 215–257.

60. S. Dubey, A. Sattar, V. Gupta, M. K. Goyal, U. K. Haritashya, J. S. Kargel, Transboundary hazard and downstream impact of glacial lakes in Hindu-Kush Karakoram Himalayas. *Sci. Total Environ.* **914**, 169758 (2024).

61. DST. Sikkim, "South Lhonak Expedition 2016: A technical Report" (2016); https://dstsikkim.gov.in/Adv/South Lhonak Lake expedition_tech report.pdf.

62. NDMA, National Disaster Management Authority of India (2023). https://ndma.gov.in/sites/default/files/2023-10/NDMA_PR_GLOF_121023.pdf.

63. M. J. Westoby, S. A. Dunning, J. L. Carrivick, T. J. Coulthard, K. Sain, A. Kumar, E. Berthier, U. K. Haritashya, D. E. Shean, M. F. Azam, K. Upadhyay, M. Koppes, H. R. McCourt, D. H. Shugar, Rapid fluvial remobilization of sediments deposited by the 2021 Chamoli disaster, Indian Himalaya. *Geology* **51**, 924–928 (2023).

64. M. M. Rahaman, A.-A.- Mamun, Hydropower development along Teesta river basin: opportunities for cooperation. *Water Policy* **22**, 641–657 (2020).

65. D. E. Shean, O. Alexandrov, Z. M. Moratto, B. E. Smith, I. R. Joughin, C. Porter, P. Morin, An automated, open-source pipeline for mass production of digital elevation models (DEMs) from very-high-resolution commercial stereo satellite imagery. *ISPRS J. Photogramm. Remote Sens.* **116**, 101–117 (2016).

66. R. A. Beyer, O. Alexandrov, S. McMichael, The Ames Stereo Pipeline: NASA's Open Source Software for Deriving and Processing Terrain Data. *Earth Sp. Sci.* **5**, 537–548 (2018).

67. C. Deschamps-Berger, S. Gascoin, E. Berthier, J. Deems, E. Gutmann, A. Dehecq, D. Shean, M. Dumont, Snow depth mapping from stereo satellite imagery in mountainous terrain: evaluation using airborne laser-scanning data. *Cryosph.* **14**, 2925–2940 (2020).

68. RGI Consortium, "Randolph Glacier Inventory - A Dataset of Global Glacier Outlines, Version 6." (Boulder, Colorado USA, 2017); https://doi.org/https://doi.org/10.7265/4m1f-gd79.

69. D. Falaschi, E. Berthier, J. M. C. Belart, C. Bravo, M. Castro, M. Durand, R. Villalba, Increased mass loss of glaciers in Volcán Domuyo (Argentinian Andes) between 1962 and 2020, revealed by aerial photos and satellite stereo imagery. *J. Glaciol.* **69**, 40–56 (2023).

70. E. S. Miles, C. S. Watson, F. Brun, E. Berthier, M. Esteves, D. J. Quincey, K. E. Miles, B. Hubbard, P. Wagnon, Glacial and geomorphic effects of a supraglacial lake

drainage and outburst event, Everest region, Nepal Himalaya. *Cryosph.* **12**, 3891–3905 (2018).

71. P. Wagnon, F. Brun, A. Khadka, E. Berthier, D. Shrestha, C. Vincent, Y. Arnaud, D. Six, A. Dehecq, M. Ménégoz, V. Jomelli, Reanalysing the 2007–19 glaciological mass-balance series of Mera Glacier, Nepal, Central Himalaya, using geodetic mass balance. *J. Glaciol.* **67**, 117–125 (2021).

72. Y. Yu, B. Li, Y. Li, W. Jiang, Retrospective Analysis of Glacial Lake Outburst Flood (GLOF) Using AI Earth InSAR and Optical Images: A Case Study of South Lhonak Lake, Sikkim. (2024). https://doi.org/10.3390/rs16132307.

73. G. Ekström, C. P. Stark, Simple Scaling of Catastrophic Landslide Dynamics. *Science (80).* **339**, 1416–1419 (2013).

74. K. L. Cook, R. Rekapalli, M. Dietze, M. Pilz, S. Cesca, N. P. Rao, D. Srinagesh, H. Paul, M. Metz, P. Mandal, G. Suresh, F. Cotton, V. M. Tiwari, N. Hovius, Detection and potential early warning of catastrophic flow events with regional seismic networks. *Science (80).* **374**, 87–92 (2021).

75. M. Dietze, The R package ``eseis'' -- a software toolbox for environmental seismology. *Earth Surf. Dyn.* **6**, 669–686 (2018).

76. H. Kanamori, J. W. Given, Analysis of long-period seismic waves excited by the May 18, 1980, eruption of Mount St. Helens—A terrestrial monopole? *J. Geophys. Res. Solid Earth* **87**, 5422–5432 (1982).

77. H. Kawakatsu, Centroid single force inversion of seismic waves generated by landslides. *J. Geophys. Res. Solid Earth* **94**, 12363–12374 (1989).

78. E. E. Brodsky, E. Gordeev, H. Kanamori, Landslide basal friction as measured by seismic waves. *Geophys. Res. Lett.* **30** (2003).

79. K. Allstadt, Extracting source characteristics and dynamics of the August 2010 Mount Meager landslide from broadband seismograms. *J. Geophys. Res. Earth Surf.* **118**, 1472–1490 (2013).

80. C. Hibert, G. Ekström, C. P. Stark, Dynamics of the Bingham Canyon Mine landslides from seismic signal analysis. *Geophys. Res. Lett.* **41**, 4535–4541 (2014).

81. J. M. Maurer, J. M. Schaefer, J. B. Russell, S. Rupper, N. Wangdi, A. E. Putnam, N. Young, Seismic observations, numerical modeling, and geomorphic analysis of a glacier lake outburst flood in the Himalayas. *Sci. Adv.* **6**, eaba3645 (2024).

82. M. Mergili, J.-T. Fischer, J. Krenn, S. P. Pudasaini, r.avaflow v1, an advanced open-source computational framework for the propagation and interaction of two-phase mass flows. *Geosci. Model Dev.* **10**, 553–569 (2017).

83. S. P. Pudasaini, M. Mergili, Mechanically Controlled Landslide Deformation. *J. Geophys. Res. Earth Surf.* **129**, e2023JF007466 (2024).

84. G. Zheng, M. Mergili, A. Emmer, S. Allen, A. Bao, H. Guo, M. Stoffel, The 2020 glacial lake outburst flood at Jinwuco, Tibet: causes, impacts, and implications for hazard and risk assessment. *Cryosph.* **15**, 3159–3180 (2021).

85. J. Klimeš, J. Novotný, I. Novotná, B. J. de Urries, V. Vilímek, A. Emmer, T. Strozzi, M. Kusák, A. C. Rapre, F. Hartvich, H. Frey, Landslides in moraines as triggers of glacial lake outburst floods: example from Palcacocha Lake (Cordillera Blanca, Peru). *Landslides* **13**, 1461–1477 (2016).

86. A. Sattar, A. Goswami, A. V Kulkarni, Hydrodynamic moraine-breach modeling and outburst flood routing - A hazard assessment of the South Lhonak lake, Sikkim. *Sci. Total Environ.* **668**, 362–378 (2019).

87. R. Jha, V. Smakhtin, "A review of methods of hydrological estimation at ungauged sites in India" (Colombo, Sri Lanka, 2008).

88. "Design Guidelines for Headworks of Hydropower Projects" (Kathmandu, Nepal); http://www.doed.gov.np/storage/listies/December2019/design-guidelines-for-headworks.pdf.

89. Z. Feng, X. Wang, Y. Ran, Dynamic impact of boulders on different types of concrete dam. *J. Mt. Sci.* **19**, 2920–2934 (2022).

90. D. H. Shugar, A. Burr, U. K. Haritashya, J. S. Kargel, C. S. Watson, M. C. Kennedy, A. R. Bevington, R. A. Betts, S. Harrison, K. Strattman, Rapid worldwide growth of glacial lakes since 1990. *Nat. Clim. Chang.* **10**, 939–945 (2020).

91. J. Muñoz Sabater, ERA5-Land hourly data from 1950 to present, *Copernicus Climate Change Service (C3S) Climate Data Store (CDS)* (2019). https://doi.org/https://doi.org/10.24381/cds.e2161bac.

92. IPCC, Ed., "Human Influence on the Climate System" in *Climate Change 2021 – The Physical Science Basis: Working Group I Contribution to the Sixth Assessment Report of the Intergovernmental Panel on Climate Change* (Cambridge University Press, Cambridge, 2023; https://www.cambridge.org/core/product/681C5DCC6B7CAF9DB626B3CD934E5D31), pp. 423–552.

93. M. F. Azam, P. Wagnon, C. Vincent, A. Ramanathan, A. Linda, V. B. Singh, Reconstruction of the annual mass balance of Chhota Shigri glacier, Western Himalaya, India, since 1969. *Ann. Glaciol.* **55**, 69–80 (2014).

94. M. F. Azam, S. Srivastava, Mass balance and runoff modelling of partially debris-covered Dokriani Glacier in monsoon-dominated Himalaya using ERA5 data since 1979. *J. Hydrol.* **590**, 125432 (2020).

95. M. Jackson, M. F. Azam, P. Baral, R. Benestad, F. Brun, S. Muhammad, S. Pradhananga, F. Shrestha, J. F. Steiner, A. Thapa, "Consequences of climate change for the cryosphere in the Hindu Kush Himalaya" in *Water, Ice, Society, and Ecosystems in the Hindu Kush Himalaya: An Outlook*, P. Wester, S. Chaudhary, N. Chettri, M. Jackson, A. Maharjan, S. Nepal, J. F. Steiner, Eds. (International Centre for Integrated Mountain Development (ICIMOD), 2023), pp. 17–71.

96. J. M. Maurer, J. M. Schaefer, S. Rupper, A. Corley, Acceleration of ice loss across the Himalayas over the past 40 years. *Sci. Adv.* **5**, eaav7266 (2024).

97. O. King, A. Dehecq, D. Quincey, J. Carrivick, Contrasting geometric and dynamic evolution of lake and land-terminating glaciers in the central Himalaya. *Glob. Planet.*

Change **167**, 46–60 (2018).

98. C. S. Watson, J. S. Kargel, D. H. Shugar, U. K. Haritashya, E. Schiassi, R. Furfaro, Mass Loss From Calving in Himalayan Proglacial Lakes. *Front. Earth Sci.* **7** (2020).

99. B. Etzelmüller, M. Guglielmin, C. Hauck, C. Hilbich, M. Hoelzle, K. Isaksen, J. Noetzli, M. Oliva, M. Ramos, Twenty years of European mountain permafrost dynamics—the PACE legacy. *Environ. Res. Lett.* **15**, 104070 (2020).

100. H. Blatter, W. Haeberli, Modelling Temperature Distribution in Alpine Glaciers. *Ann. Glaciol.* **5**, 18–22 (1984).

101. N. J. Wilson, G. E. Flowers, Environmental controls on the thermal structure of alpine glaciers. *Cryosph.* **7**, 167–182 (2013).

102. W. Haeberli, L. U. Arenson, J. Wee, C. Hauck, N. Mölg, Discriminating viscous creep features (rock glaciers) in mountain permafrost from debris-covered glaciers -- a commented test at the Gruben and Yerba Loca sites, Swiss Alps and Chilean Andes. *EGUsphere* **2023**, 1–23 (2023).

103. H. Hersbach, B. Bell, P. Berrisford, S. Hirahara, A. Horányi, J. Muñoz-Sabater, J. Nicolas, C. Peubey, R. Radu, D. Schepers, A. Simmons, C. Soci, S. Abdalla, X. Abellan, G. Balsamo, P. Bechtold, G. Biavati, J. Bidlot, M. Bonavita, G. De Chiara, P. Dahlgren, D. Dee, M. Diamantakis, R. Dragani, J. Flemming, R. Forbes, M. Fuentes, A. Geer, L. Haimberger, S. Healy, R. J. Hogan, E. Hólm, M. Janisková, S. Keeley, P. Laloyaux, P. Lopez, C. Lupu, G. Radnoti, P. de Rosnay, I. Rozum, F. Vamborg, S. Villaume, J.-N. Thépaut, The ERA5 global reanalysis. *Q. J. R. Meteorol. Soc.* **146**, 1999–2049 (2020).

104. J. Muñoz-Sabater, E. Dutra, A. Agust\'\i-Panareda, C. Albergel, G. Arduini, G. Balsamo, S. Boussetta, M. Choulga, S. Harrigan, H. Hersbach, B. Martens, D. G. Miralles, M. Piles, N. J. Rodr\'\iguez-Fernández, E. Zsoter, C. Buontempo, J.-N. Thépaut, ERA5-Land: a state-of-the-art global reanalysis dataset for land applications. *Earth Syst. Sci. Data* **13**, 4349–4383 (2021).

105. A. Y. Hou, R. K. Kakar, S. Neeck, A. A. Azarbarzin, C. D. Kummerow, M. Kojima, R. Oki, K. Nakamura, T. Iguchi, The Global Precipitation Measurement Mission. *Bull. Am. Meteorol. Soc.* **95**, 701–722 (2014).

106. G. J. Huffman, D. T. Bolvin, D. Braithwaite, K.-L. Hsu, R. J. Joyce, C. Kidd, E. J. Nelkin, S. Sorooshian, E. F. Stocker, J. Tan, D. B. Wolff, P. Xie, "Integrated Multi-satellite Retrievals for the Global Precipitation Measurement (GPM) Mission (IMERG) BT - Satellite Precipitation Measurement: Volume 1" V. Levizzani, C. Kidd, D. B. Kirschbaum, C. D. Kummerow, K. Nakamura, F. J. Turk, Eds. (Springer International Publishing, Cham, 2020; https://doi.org/10.1007/978-3-030-24568-9_19), pp. 343–353.

107. P. Xie, P. A. Arkin, Global Precipitation: A 17-Year Monthly Analysis Based on Gauge Observations, Satellite Estimates, and Numerical Model Outputs. *Bull. Am. Meteorol. Soc.* **78**, 2539–2558 (1997).

108. D. S. Wilks, *Statistical Methods in the Atmospheric Sciences* (Academic Press, ed. 3, 2011).

109. J. Benesty, J. Chen, Y. Huang, I. Cohen, “Pearson Correlation Coefficient BT - Noise Reduction in Speech Processing” I. Cohen, Y. Huang, J. Chen, J. Benesty, Eds. (Springer Berlin Heidelberg, Berlin, Heidelberg, 2009; https://doi.org/10.1007/978-3-642-00296-0_5), pp. 1–4.

110. M. H. Kutner, C. J. Nachtsheim, W. Neter, John; Li, *Applied Linear Statistical Models* (McGraw-Hill, ed. 5, 2005).

111. K. Y. Kim, G. R. North, EOF Analysis of Surface Temperature Field in a Stochastic Climate Model. *J. Clim.* **6**, 1681–1690 (1993).

112. E. I. Obilor, E. C. Amadi, Test for Significance of Pearson’s Correlation Coefficient (r). *Int. J. Innov. Math. Stat. Energy Policies* **6**, 11–23 (2018).

113. D. A. Lavers, A. Simmons, F. Vamborg, M. J. Rodwell, An evaluation of ERA5 precipitation for climate monitoring. *Q. J. R. Meteorol. Soc.* **148**, 3152–3165 (2022).

114. Y. Xin, Y. Yang, X. Chen, X. Yue, Y. Liu, C. Yin, Evaluation of IMERG and ERA5 precipitation products over the Mongolian Plateau. *Sci. Rep.* **12**, 21776 (2022).

115. J. Xu, Z. Ma, S. Yan, J. Peng, Do ERA5 and ERA5-land precipitation estimates outperform satellite-based precipitation products? A comprehensive comparison between state-of-the-art model-based and satellite-based precipitation products over mainland China. *J. Hydrol.* **605**, 127353 (2022).

116. H. E. Beck, M. Pan, T. Roy, G. P. Weedon, F. Pappenberger, A. I. J. M. van Dijk, G. J. Huffman, R. F. Adler, E. F. Wood, Daily evaluation of 26 precipitation datasets using Stage-IV gauge-radar data for the CONUS. *Hydrol. Earth Syst. Sci.* **23**, 207–224 (2019).

117. W. Sirko, S. Kashubin, M. Ritter, A. Annkah, Y. S. E. Bouchareb, Y. Dauphin, D. Keysers, M. Neumann, M. Cisse, J. Quinn, Continental-Scale Building Detection from High Resolution Satellite Imagery. *arXiv Prepr.*, doi: https://doi.org/10.48550/arXiv.2107.12283 (2021).

118. Open Buildings, A dataset of building footprints to support social good applications. https://sites.research.google/open-buildings/.

119. OSM, OpenStreetMap. http://www.openstreetmap.org.

120. BWDB, “Technical Report on Improving Data Collection; Long Term Monitoring, Research and Analysis of Bangladesh Coastal Zone (Sustainable Polders Adapted to Coastal Dynamics)” (2022); https://acrobat.adobe.com/id/urn:aaid:sc:AP:ef3fa0bc-578e-4fd0-ba6d-57a8ecda61c0.

121. E. Hossain, S. Ali, R. K. Manik, Rain, flash flood wreak havoc in north part of Bangladesh, *NEW AGE* (2023). https://www.google.com/url?q=https://www.newagebd.net/article/214140/rain-flash-flood-wreak-havoc-in-north-part-of-bangladesh&sa=D&source=docs&ust=1722328626097218&usg=AOvVaw2ZsOeg0knyHK_z1DtRHjs1.

122. S. Report, Flash floods hit 3 northern dists, *The Daily Star* (2023). https://www.thedailystar.net/environment/news/flash-floods-hit-3-northern-dists-

3435866.

123. N. SAGE, NSF SAGE Facility Web Services. https://service.iris.edu/.

124. Sentinel Hub. https://www.sentinel-hub.com/.

125. PlanetLabs, Education and Research—Satellite Imagery Solutions, *Planet* (2023). https://planet.com/markets/education-and-research.

126. E. Berthier, Spot6 and Pléiades Digital Elevation Models (DEMs) and elevation change grid to understand the South Lhonak lake (Sikkim) flood of October 2023. Zenodo (2024). https://doi.org/10.5281/zenodo.13122207.

127. S. Gascoin, K. Cook, Pléiades Digital Elevation Models of South Lhonak Lake (Sikkim, India). Zenodo (2024). https://doi.org/10.5281/zenodo.13124662.

128. M. Mergili, S. P. Pudasaini, r.avaflow - The mass flow simulation tool, *2014-2024*. https://www.avaflow.org.

129. A. Sattar, S. Rinzin, M. Mergili, r.avaflow simulation package for 3 October 2023 South Lhonak GLOF reconstruction in Sikkim, India. Zenodo (2024). https://doi.org/10.5281/zenodo.13254778.

130. M. V. W. De Vries, Detection of slow-moving landslides from Sentinel-2 optical satellite imagery. Zenodo (2023). https://doi.org/10.5281/zenodo.7766276.

131. R. W. Herschy, The world's maximum observed floods. *Flow Meas. Instrum.* **13**, 231–235 (2002).

Acknowledgments: We acknowledge PlanetLabs for the pre- and post-flood PlanetScope and SkySat images used in the study. This work used acquired Pléiades and SPOT6 images, thanks to the CIEST2 service developed and performed with the French Space Agency (CNES) by FormaTerre, Solid Earth component of the Data Terra Research Infrastructure. All seismic data were downloaded through the EarthScope Consortium Web Services (*123*). AS acknowledges IIT Bhubaneswar for providing the necessary office resources to carry out the work. We thank SSDMA for supporting this work. We thank the ITBP and SSDMA for providing insightful ground information. Our gratitude extends to all individuals, stakeholders, and government offices who contributed to this comprehensive work. SA, HF, and CH acknowledge the support of the Swiss Agency for Development and Cooperation (SDC) in several collaborations on hazards and risks in the Indian Himalaya, including the SCA project.

Funding: AS was supported by the DST Inspire Faculty Fellowship, Ministry of Science and Technology, Government of India (GOI). EB was supported by the French Space Agency (TOSCA/CNES). MVWDV was supported by Isaac Newton Trust (UK), grant G122390. DHS was supported by Natural Sciences and Engineering Research Council of Canada (NSERC), Alberta Innovates, grant DG-2020-04207. MFA was supported by the Ministry of Earth Sciences (MoES), GOI, grant MOES/PAMC/H&C/131/2019-PC-II. RKR was supported by the DST's Centre of Excellence at Sikkim University funded by the Department of Science and Technology, GOI DST/CCP/CoE/186/2019 (G). IR was supported by MoES, GOI granted MoES/PAMC/H&C/127/2019-PC-II. NI was supported by the Swiss Government Excellence Scholarship, grant 2020.0271. MDG was supported by ThePrint office, New Delhi.

Author contributions: Conceptualization: AS, KLC, SA, MVWDV, WH, PK; **Data Curation:** AS, KLC, SKR, EB, MVWDV, PK, DHS, AE, HF, PRO, KSK, PRA, RR, FH, MFA, SG, RKR, IR, MDG, WS, CSW, NI; **Formal Analysis:** AS, KLC, SKR, EB, SA, SR, MVWDV, WH, PK, DHS, AE, HF, MFA, SG, IR; **Funding Acquisition**: AS, EB, MVWDV, DHS, MFA, RKR, IR, NI, MDG; **Investigation:** AS, KLC, SKR, EB, SA, SR, MVWDV, WH, PK, DHS, AE, HF, PRO, KSK, PRA, MFA, SG, LEB, IR, CSW, SYB; **Methodology:** AS, KLC, SKR, EB, SA, SR, MVWDV, WH, PK, MFA, SG; **Project Administration:** AS, KLC, SKR, EB, MVWDV; **Resources**: KLC, EB, DHS, PRO, KSK, PRA, FH; **Software:** MVWDV, MM; **Supervision:** AS, WH, CH, AVK, JLC, DP, UKH; **Validation:** AS, KLC, SKR, EB, SA, MVWDV, WH, PK, AE, PRO, SK, PRA, RR, FH, MDG; **Visualization:** AS, KLC, SKR, SA, MVWDV, WH, PK, DHS, AE, UKH, MFA, SG, IR, SYB; **Writing (original draft):** AS, KLC, EB, SA, MVWDV, WH, PK, AE, MFA, JLC; **Writing (review & editing):** AS, KLC, SKR, EB, SA, SR, MVWDV, WH, PK, DHS, AE, UKH, HF, PRO, KSK, PRA, RR, FH, CH, MM, MFA, SG, JLC, LEB, RKR, IR, AVK, DP, WS, CSW, NI, MDG, SNL.

Competing interests: The authors declare that they have no competing interests.

Data and materials availability: We used publicly available data sources whenever possible. The Sentinel-2 data are available from (*124*). PlanetScope satellite image data are available through Planet's Education and Research Program (*125*). Pre- and post-event very-high-resolution satellite images are available through Airbus/CNES (Pléiades and SPOT 6). We make the pre- and post-GLOF high-resolution DEM composites created in this study available in the repository (*126*) for 4 m DEMs and (*127*) for the 1 m DEMs. Building footprints were obtained from (*117, 118*). Road networks were obtained from (*119*). The r.avaflow model is available at (*128*). We make the model codes and South Lhonak reconstructed GLOF movie available in the repository (*129*). The toolbox for measuring the surface displacement of slow-moving landslides is available from (*130*). All ERA5 data can be found at https://cds.climate.copernicus.eu/#!/home. IMERG data is available at https://disc.gsfc.nasa.gov/datasets/GPM_3IMERGHH_07/summary?keywords=%22IMERG%20final%22. CPC Global Precipitation is available at https://psl.noaa.gov/data/gridded/data.cpc_blended_olr-2.5deg.html. Station rainfall data for Dalia station was procured from the Bangladesh Water Development Board (BWDB). Station rainfall data from Lachen was personally retrieved during fieldwork from the AWS installed as a part of the funding received by the Department of Science and Technology, Government of India DST/CCP/CoE/186/2019.

Supplementary Materials

Figs. S1 to S47

Tables S1 to S11

Movies S1

Fig. S1.

Post-GLOF field observations of the SLL reveal several key features. (A) the exposed surface of the breached frontal moraine, with exposed dead ice within the moraine. (B) a significant drop in lake level, resulting in a reduced lake size, and an exposed lakebed post-GLOF. (C) the breached frontal moraine as seen from upstream. Photo credits: ITBP.

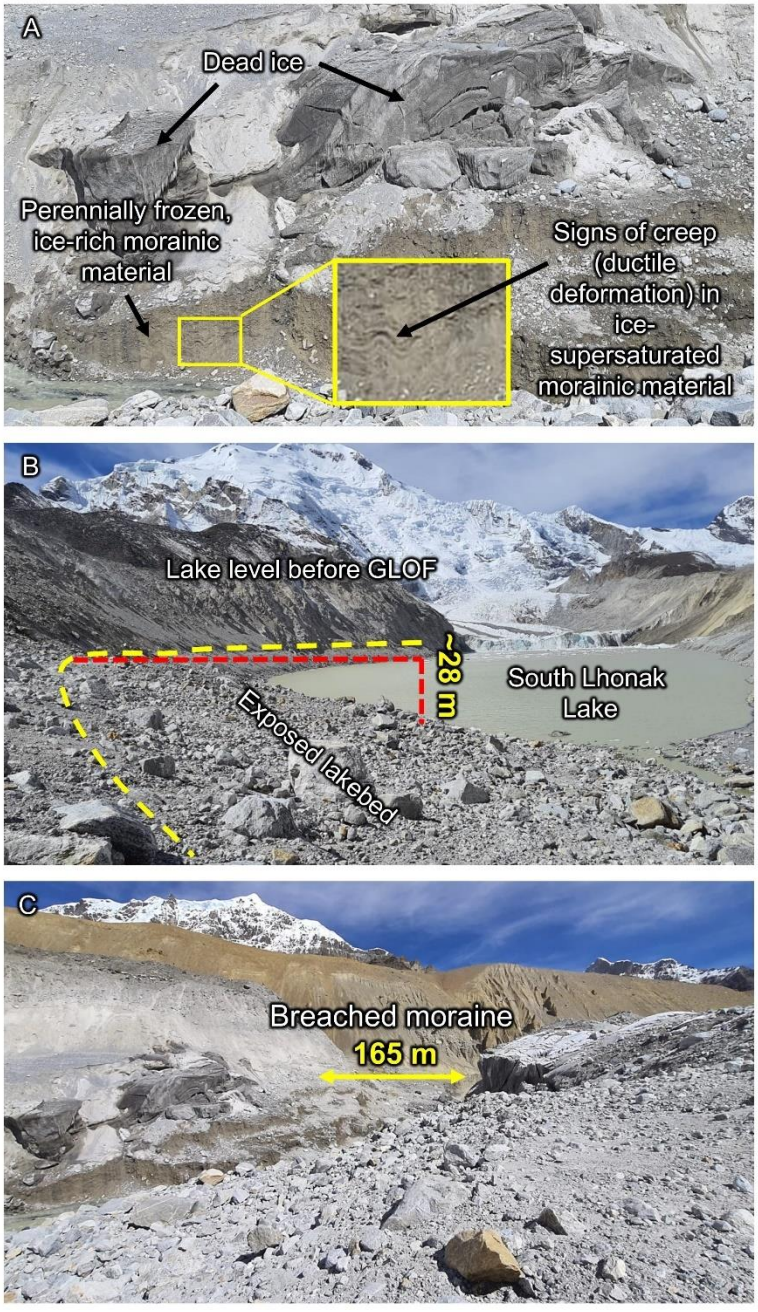

Fig. S2.

2017-2022 pre-GLOF velocity map (top panel) and time-series (b and c; m a^{-1}) for two regions over the northern lateral moraine of SLL. Background imagery in the top panel is a Sentinel-2 satellite image from 11 October 2021.

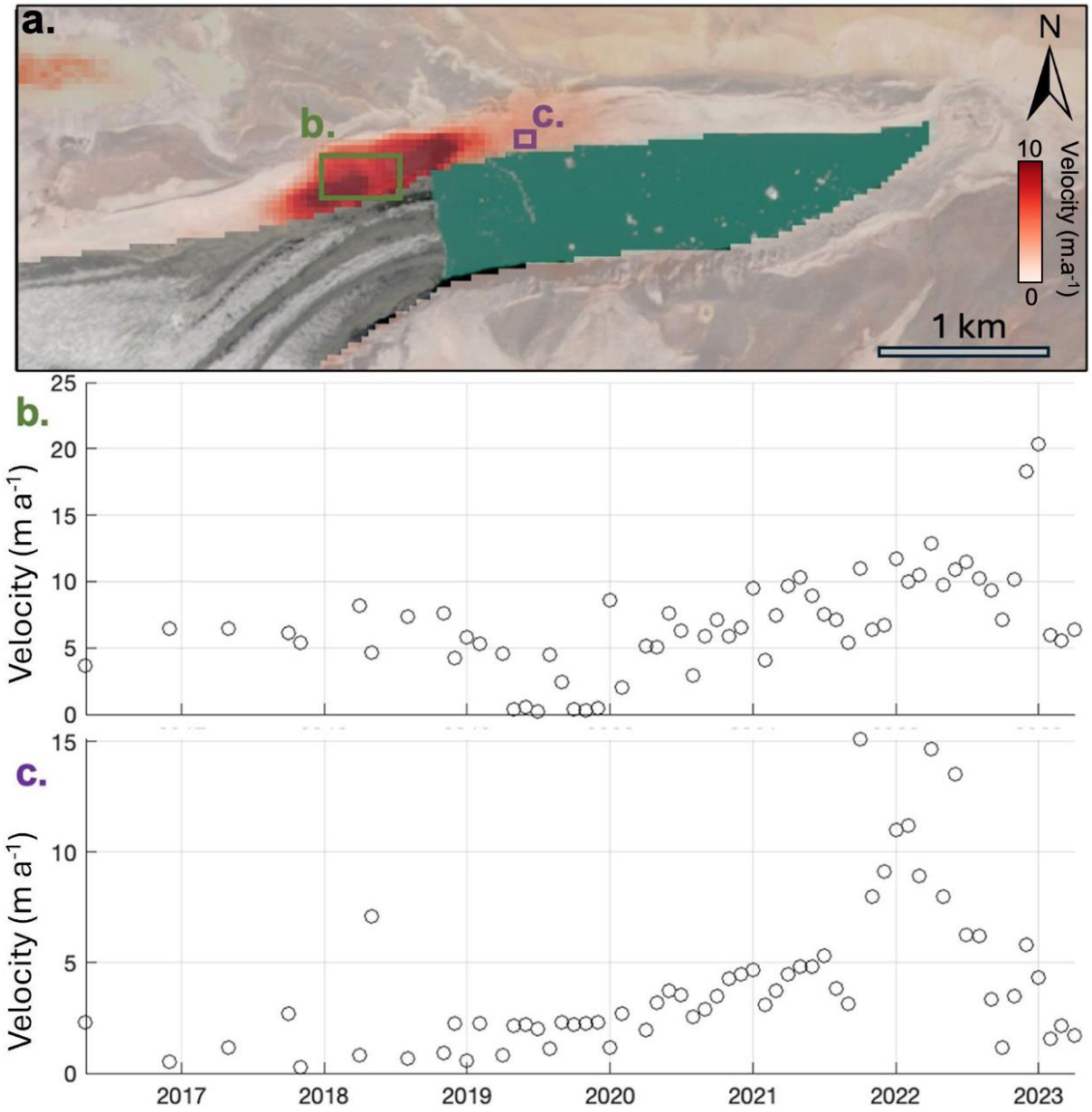

Fig. S3.

Pre-GLOF median velocity (m a^{-1}) of the northern lateral moraine of SLL from 2016-2023.

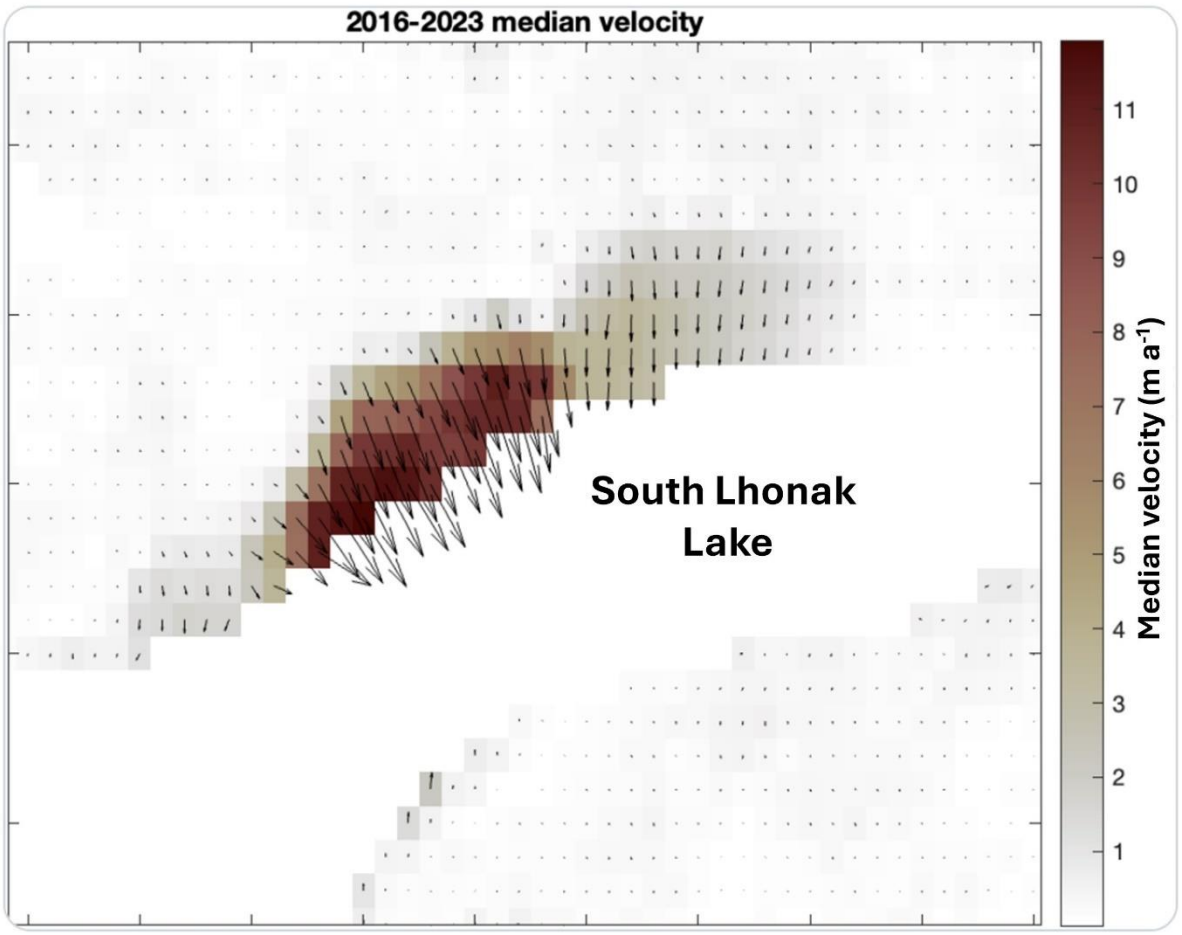

Fig. S4.

Location estimates for the potential landslide (northern lateral moraine failure of SLL) seismic signal identified at 16:42 UTC, based on data from seismic stations: EVN, KKN, and LSA. The green contour indicates the probable signal source region, and the black dot shows the best-fit source location. The geometry of the stations limits the precision of the source location estimate. The estimated location probabilities are consistent with a source located at SLL.

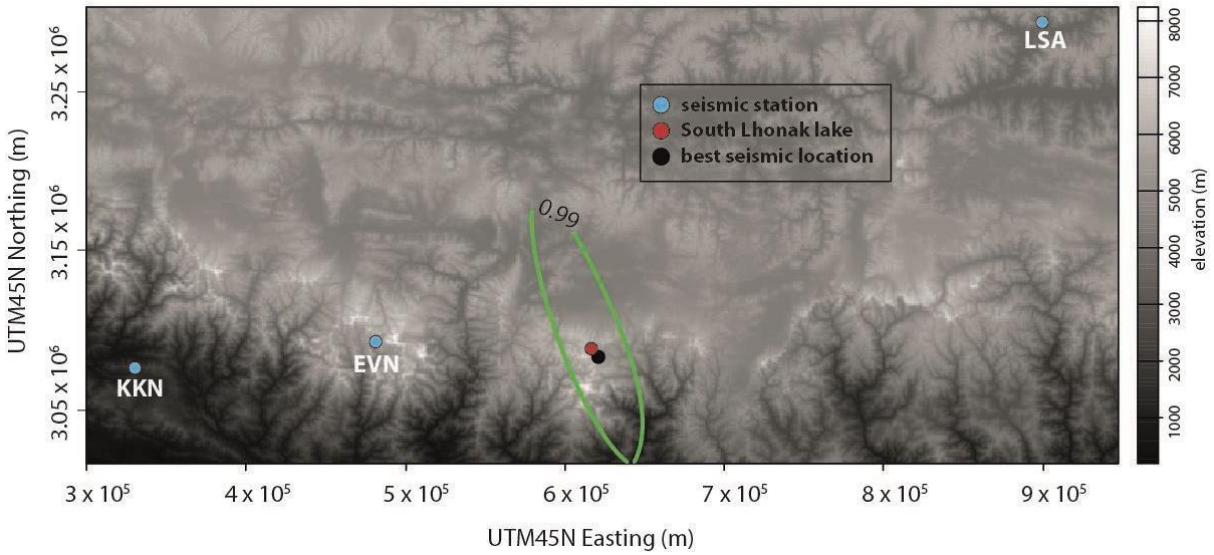

Fig. S5.

Seismic signal of northern moraine failure of SLL at EVN, KKN, and LSA stations. The black lines show the low-frequency signal (0.01-0.5 Hz), and the blue lines show the high-frequency signal (1-5 Hz).

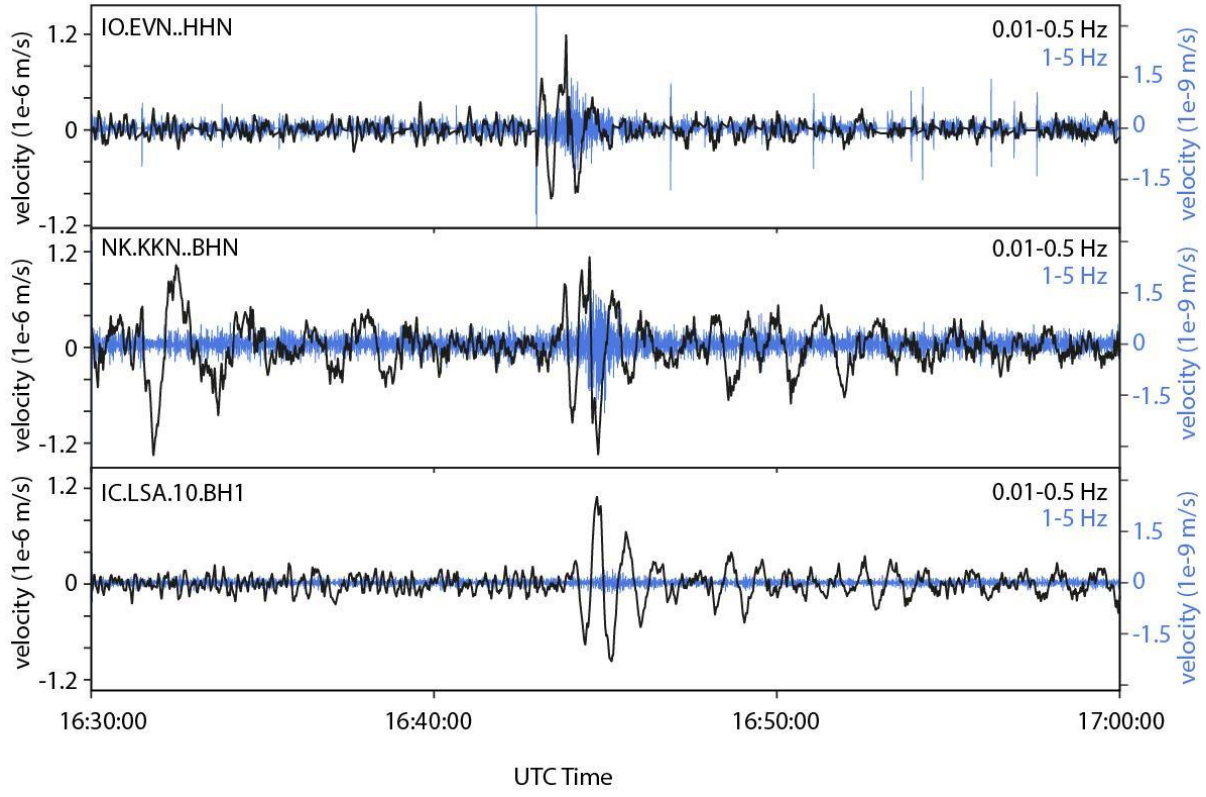

Fig. S6.

Probable seismic signal of the GLOF cascade at EVN and KKN stations (no signal was visible at LSA station). The simultaneous increase in background noise at both stations, and the greater magnitude at EVN station are consistent with the flood as the source of the signal. The appearance of the signal several hours after flood initiation likely reflects an increase in the magnitude of seismic noise generated by the flood due to sediment entrainment and the bulking of the flow.

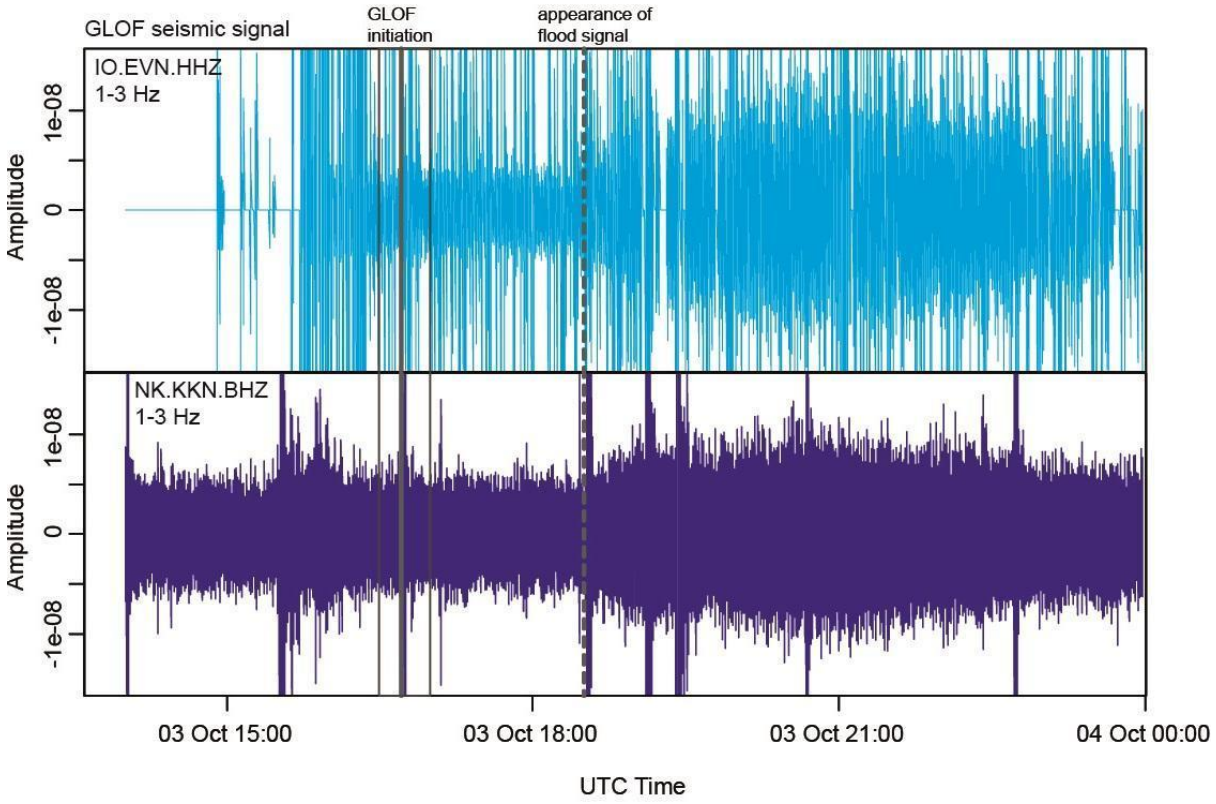

Fig. S7.

(A) Maximum erosion of the frontal moraine reconstructed for different inputs of erosion coefficient (CE=$10^{-6.75}$ to $10^{-6.25}$). The hillshade in the background is derived from post-GLOF (29 October 2023) Pléiades stereo-pairs © CNES (2023) Distribution Airbus DS, Distribution AIRBUS DS. (B) maximum erosion depth vs. distance along cross-section aa′ (shown in the first panel of A) reconstructed for different values of CE (C) Reconstructed time of GLOF arrival (in IST) at the ITBP camp (located 7.12 km downstream of the lake where reported GLOF arrival was 22.30 IST on 3 October 2023) for different values of CE. The reconstruction with CE=$10^{-6.25}$ shows good agreement with the observed frontal moraine erosion and GLOF arrival time at the ITBP camp (also see Figs. 3A and 3B).

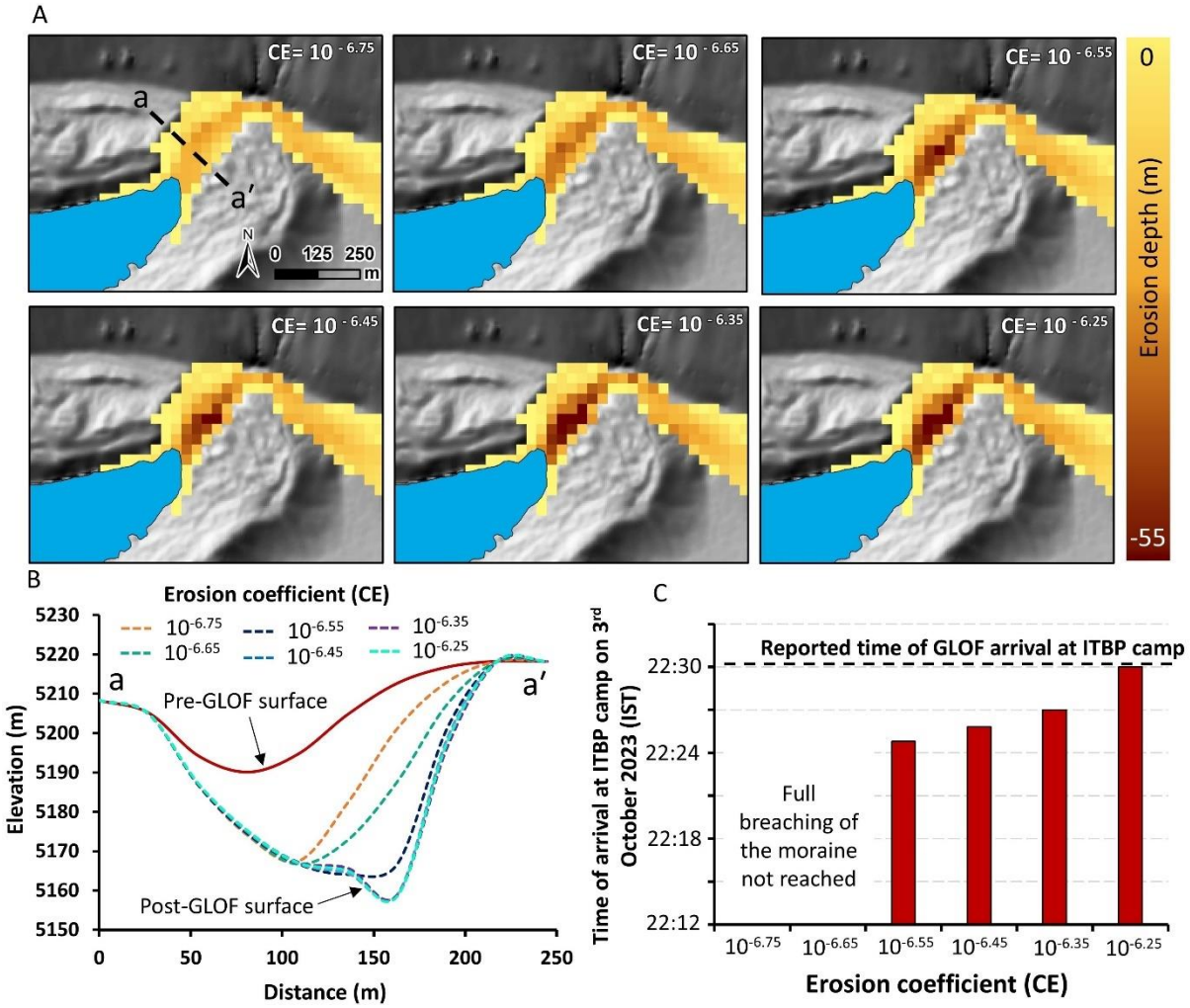

Fig. S8.

Reconstructed deposition of collapsed moraine material under SLL, derived based on the best-fit (validated) GLOF process chain model ($CE=10^{-6.25}$, see section 4). The background hillshade is created from post-GLOF (29 October 2023) Pléiades stereo-pairs © CNES (2023) Distribution Airbus DS.

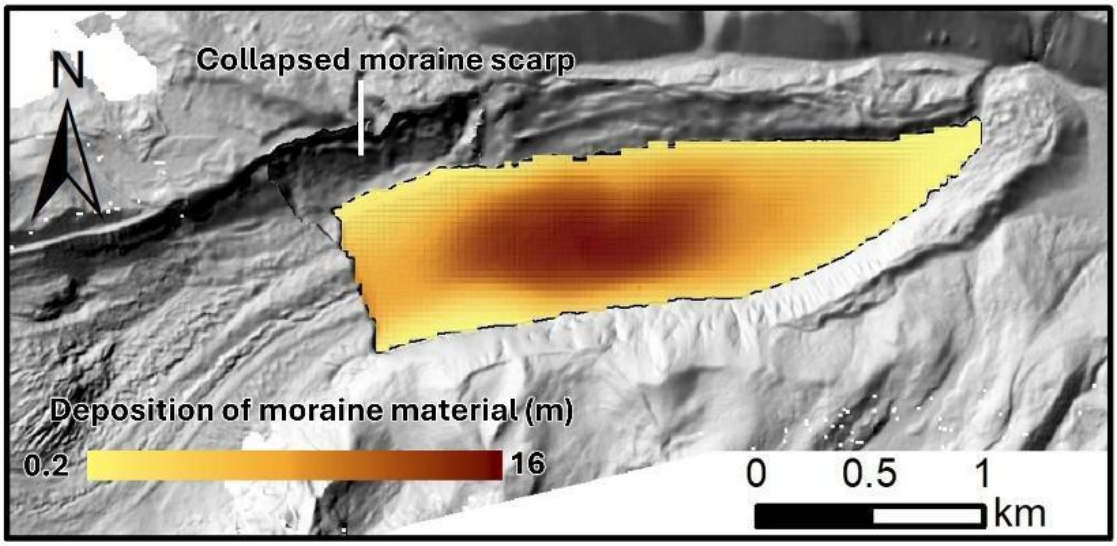

Fig. S9. Peak discharge vs. distance from the South Lhonak Lake for the reconstructed 2023 GLOF event and the different return period flood discharges for 2-year, 10-year, 100-year, 1000-year, and 1000-year return period floods; Qmax is calculated from (*131*). Note that all discharges are water-only flood estimates and do not consider erosion and entrainment of sediment.

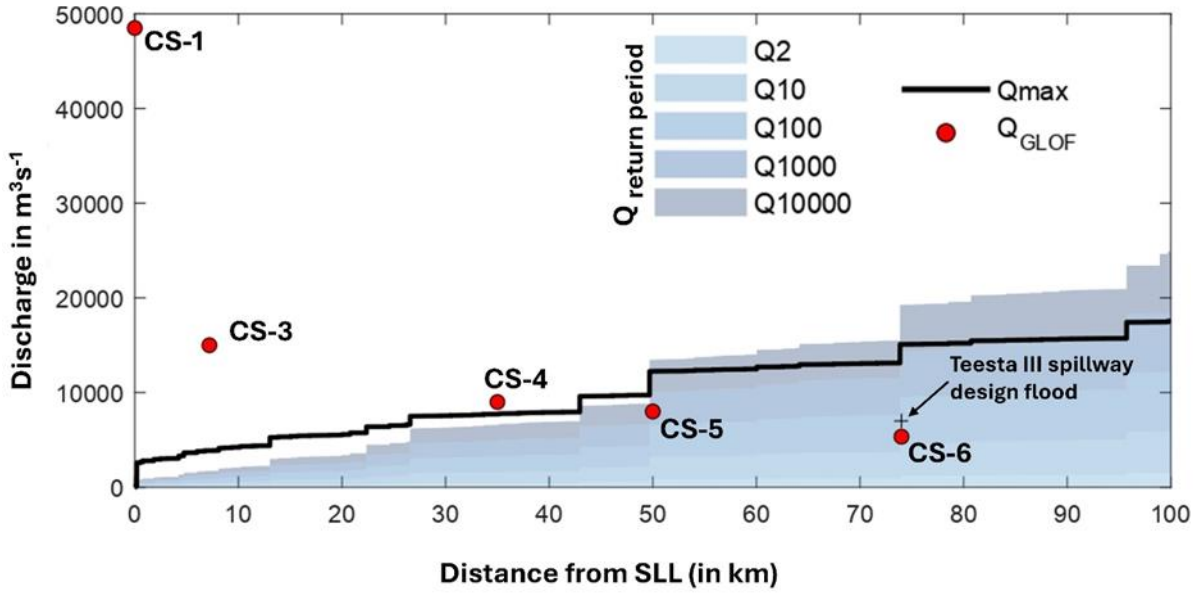

Fig. S10.

Annual air temperature anomalies based on daily mean temperature from the ERA5-Land reanalysis over SLL. Panel (A) shows anomalies for all months, and panel (B) focuses on anomalies from June to September (JJAS). Anomalies are calculated relative to the 1991-2020 standard climatological reference period. The dashed line represents a 5-year trailing moving average.

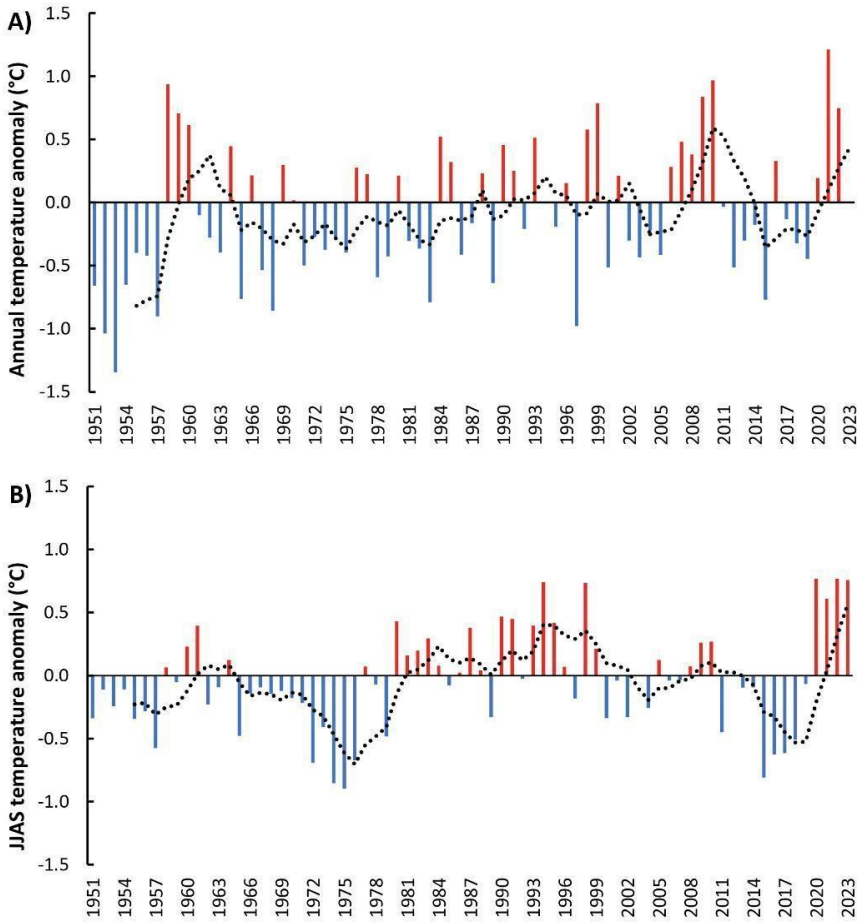

Fig. S11.

Annual precipitation anomalies over SLL, derived from daily precipitation data for the months of June to September (JJAS) using ERA5-Land reanalysis. Anomalies are calculated relative to the 1991-2020 standard climatological reference period. The dashed line represents a 5-year trailing moving average.

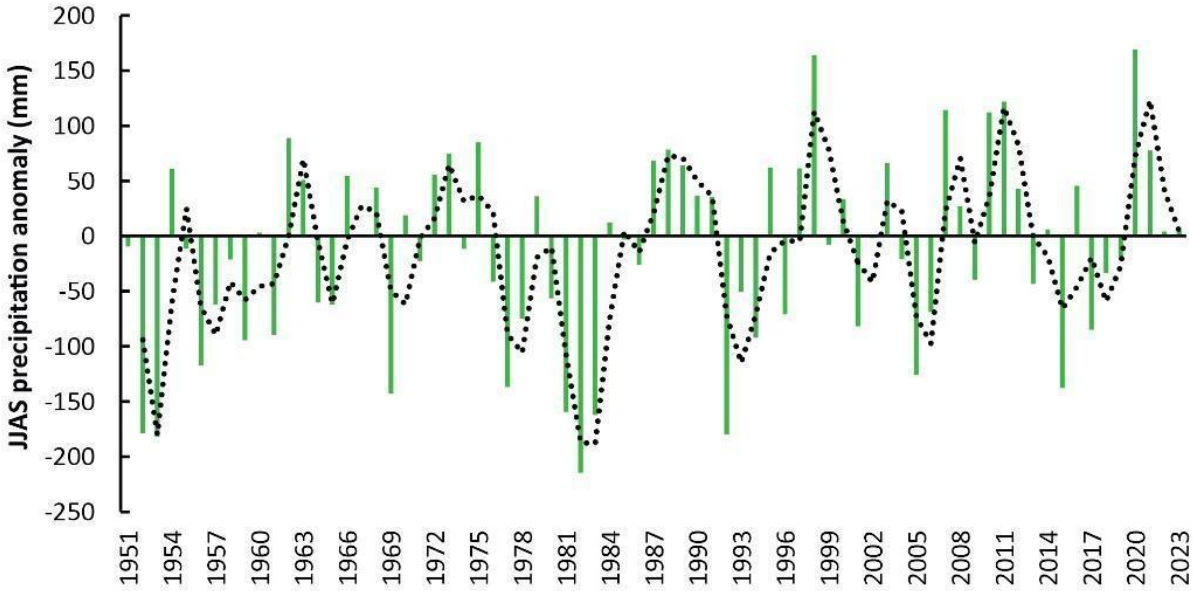

Fig. S12.

The modeled annual glacier-wide mass balances since 1950 (black dots), mean annual air temperature (dark brown dots), and precipitation (light blue dots). The geodetic mean mass balance available over 2000-2019 is shown as a thick blue line (*32*). The estimated uncertainties in modeled glacier-wide mass balances and mean geodetic mass balance are also shown as grey bars and a light blue envelope, respectively. The trends in mean annual temperature and precipitation plotted over 1950-2023 are significant, with corresponding statistics provided at the bottom of the figure panel. The air temperature and precipitation data is from the nearest ERA5 grid point (27.875 N, 88.375 E; 4514 m a.s.l.), which is ~18 km downstream of SLL.

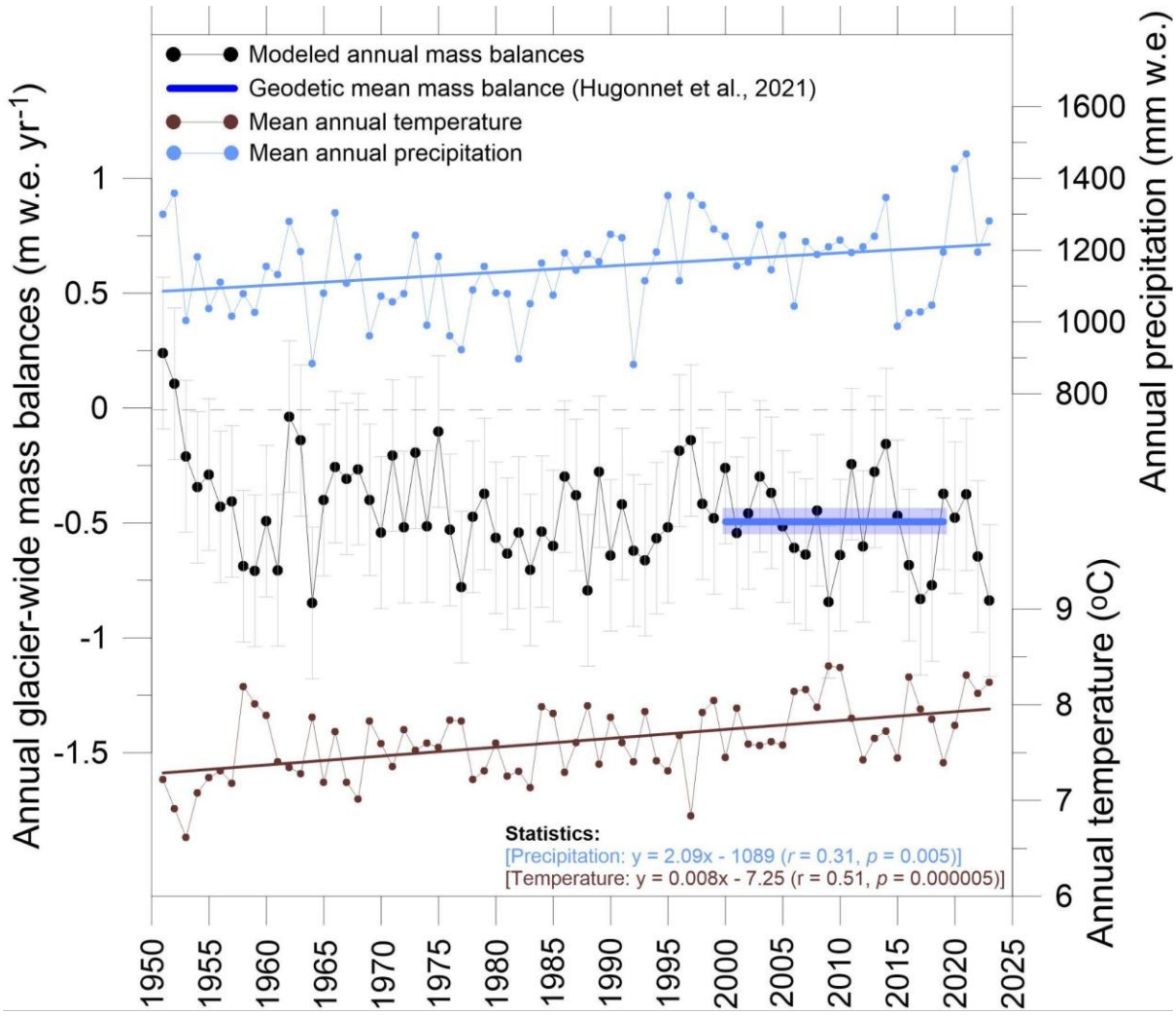

Fig. S13.

Viscous creep features in permafrost (rock glaciers) in the valley below SLL. The figure includes an overview (upper left), north-exposed slopes (1), and south-exposed slopes (2, 3, 4), with the elevations given in meters above sea level. All background imagery is © Maxar Technology/CNES/ Airbus (Google Earth).

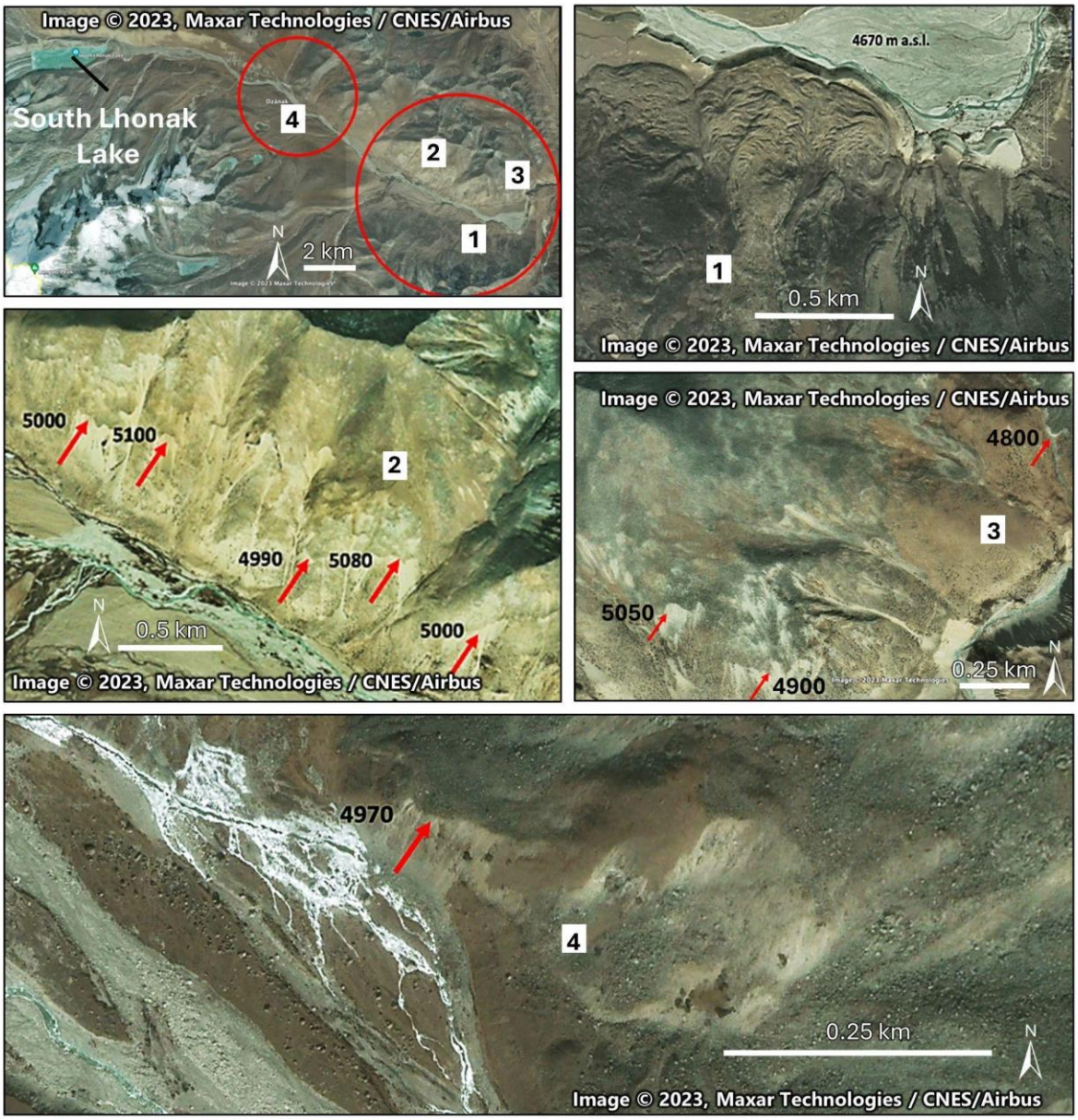

Fig. S14.

An overview of permafrost-related surface processes and landforms around SLL. 1 = perennially frozen southern (orographic right) and terminal moraine with active fronts of down-valley creeping ice-rich permafrost. 2 = inactive lobes of former rock-glacier type deformation at the external foot of the frozen southern moraine. 3 = various and, in places, large slope movements on the sunny side of the northern (orographic left) moraine, likely containing relatively warm permafrost. 4 = slope detachments and movements towards the northern moraine. 5 = cold debris-covered glacier in permafrost, featuring multiple thermokarst structures. 6 = glacier forefield showing signs of viscous deformations. a= accumulation zone, b=glacier headwall, c=glacier tongue. Background imagery is © Maxar Technology/CNES/ Airbus (Google Earth).

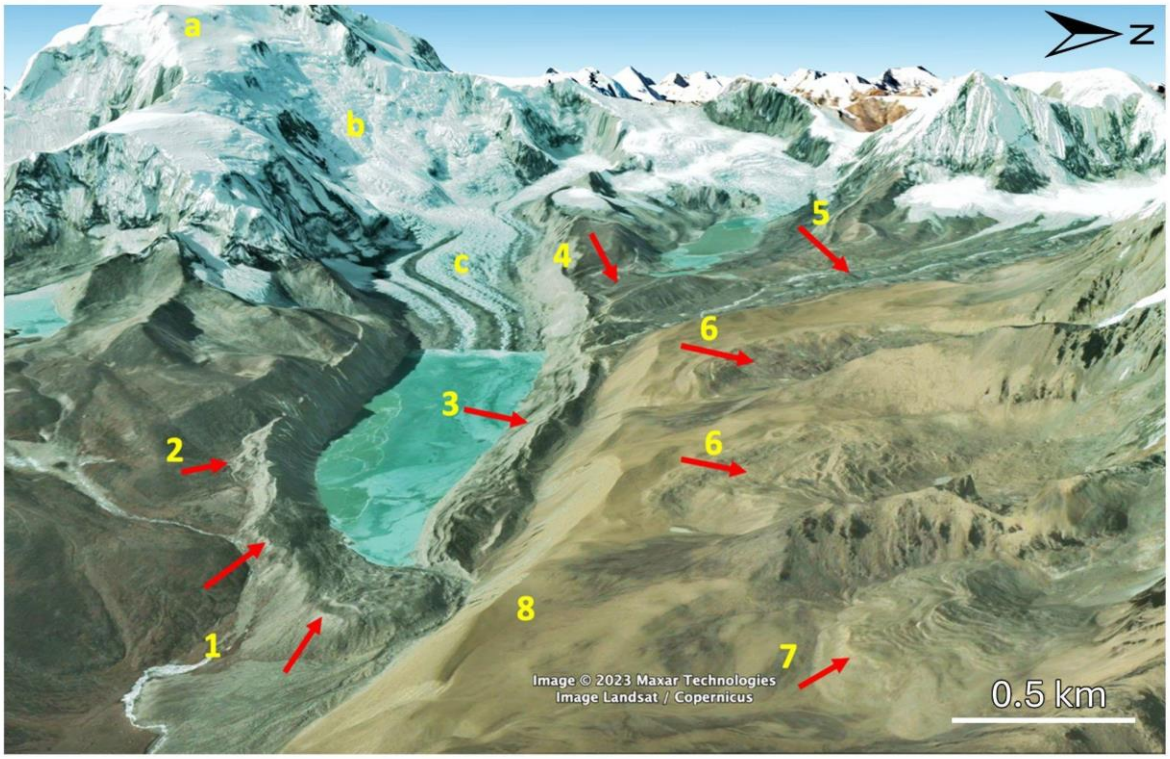

Fig. S15.

Coherent cumulative deformation in ice-rich permafrost at the southern lateral moraine (orographic right) of SLL. 1 = rock glacier-like structures indicating creep movements away from the moraine. 2 = coherent deformational structures indicating slope movements towards the moraine. 3 = detachment towards the lake side. Background imagery is © Maxar Technology/CNES/ Airbus (Google Earth)

Fig. S16.

Active creep in ice-rich permafrost and thermokarst ponds on the frontal moraine of SLL. 1 = creep and detachment areas. 2 = active creep with debris material exposure. 3 = thermokarst ponds, likely formed in buried dead ice. Background imagery is © Maxar Technology/CNES/ Airbus (Google Earth).

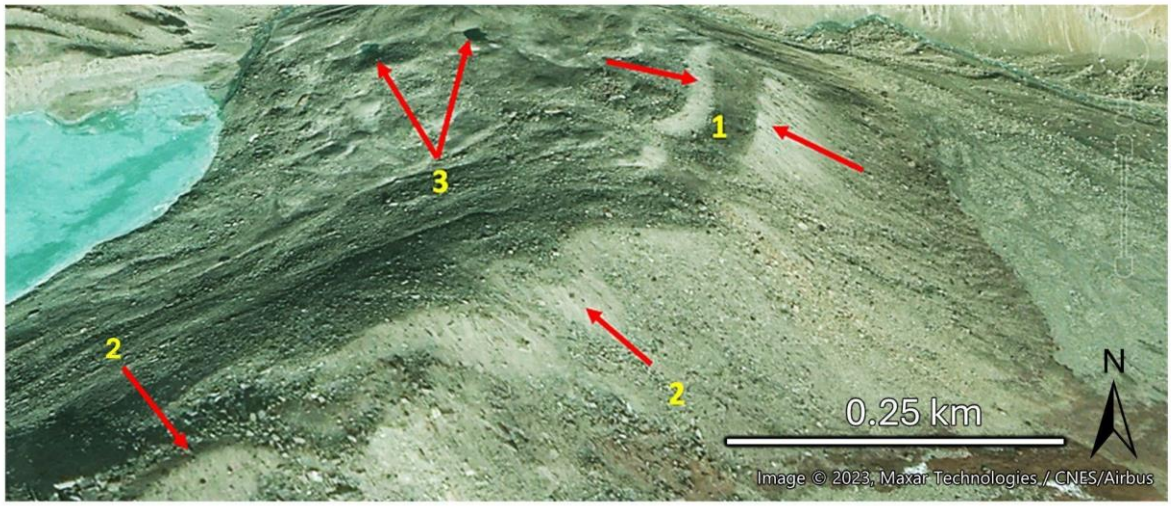

Fig. S17.

Surface processes outside the northern lateral (orographic left) moraine of SLL. 1 = detachment areas. 2 = active creep towards the northern moraine. 3 = river erosion. 4 = surface drainage on frozen debris towards the northern moraine. Background imagery is © Maxar Technology/CNES/ Airbus (Google Earth).

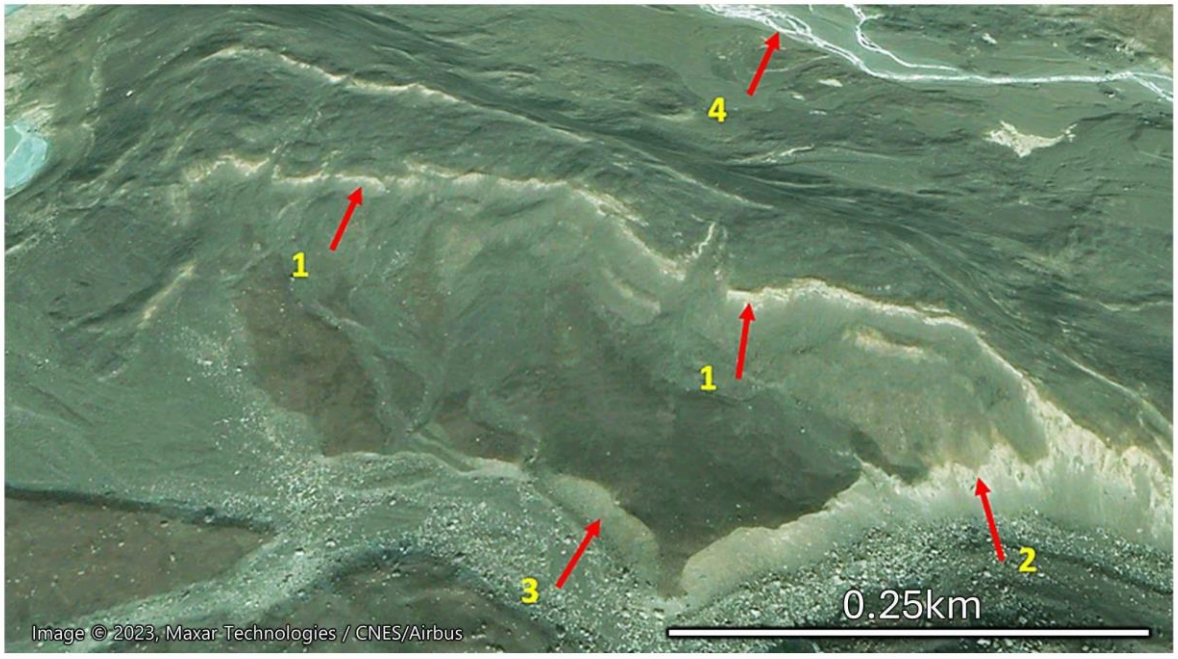

Fig. S18.

Erosion and slope instability on the lateral moraines. 1 = surface erosion, likely due to active layer detachment slides on the southern lateral moraine. 2 = rapid deep-seated coherent sliding over the northern moraine. 3 = site of the deep-seated moraine collapse on 3 October 2023. 4 = areas of diffuse detachment, sliding, and erosion. 5 = surface drainage flowing towards and through the northern moraine. Background imagery is © Maxar Technology/CNES/ Airbus (Google Earth).

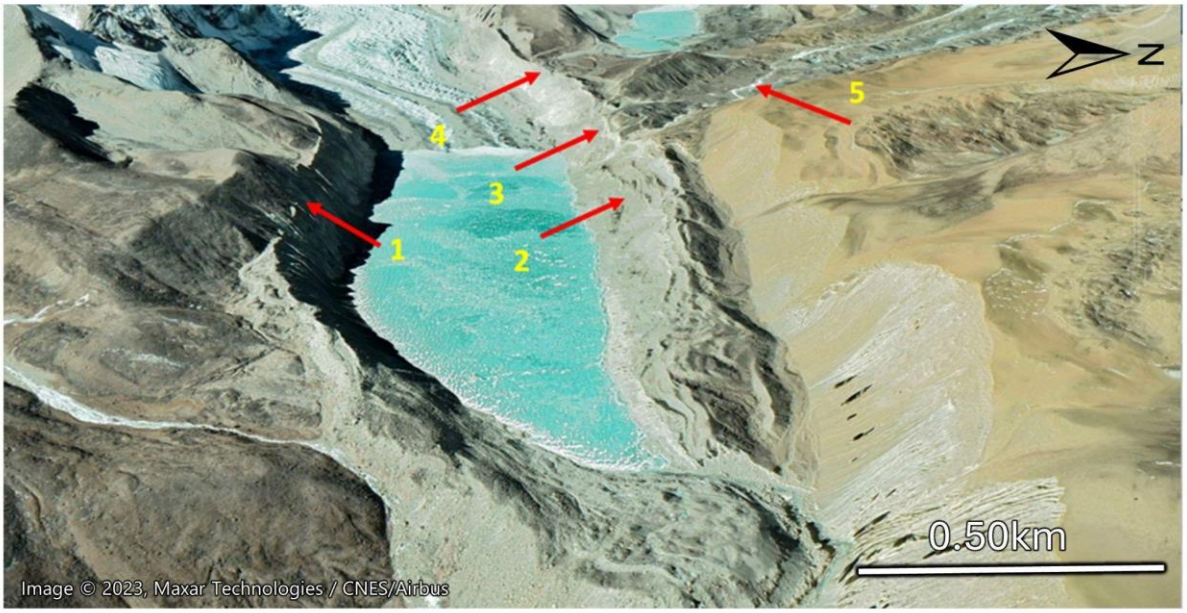

Fig. S19.

(A) Changes in the area and length of SLL, derived from interpretation of Landsat (1975–2015) and Sentinel-2 (2016–2023) satellite imagery. The length is calculated along the orographic left side of the lake (along the northern lateral moraine), extending from the lake outlet towards the failure zone. (B) The mapped lake extent is shown for selected years from 2010–2023, showing the rapid expansion of the lake below the subsequent failure zone of the northern lateral moraine on 3 October 2023. The background image is a Sentinel-2 image from 2020. All images used for lake mapping were acquired between late September to October.

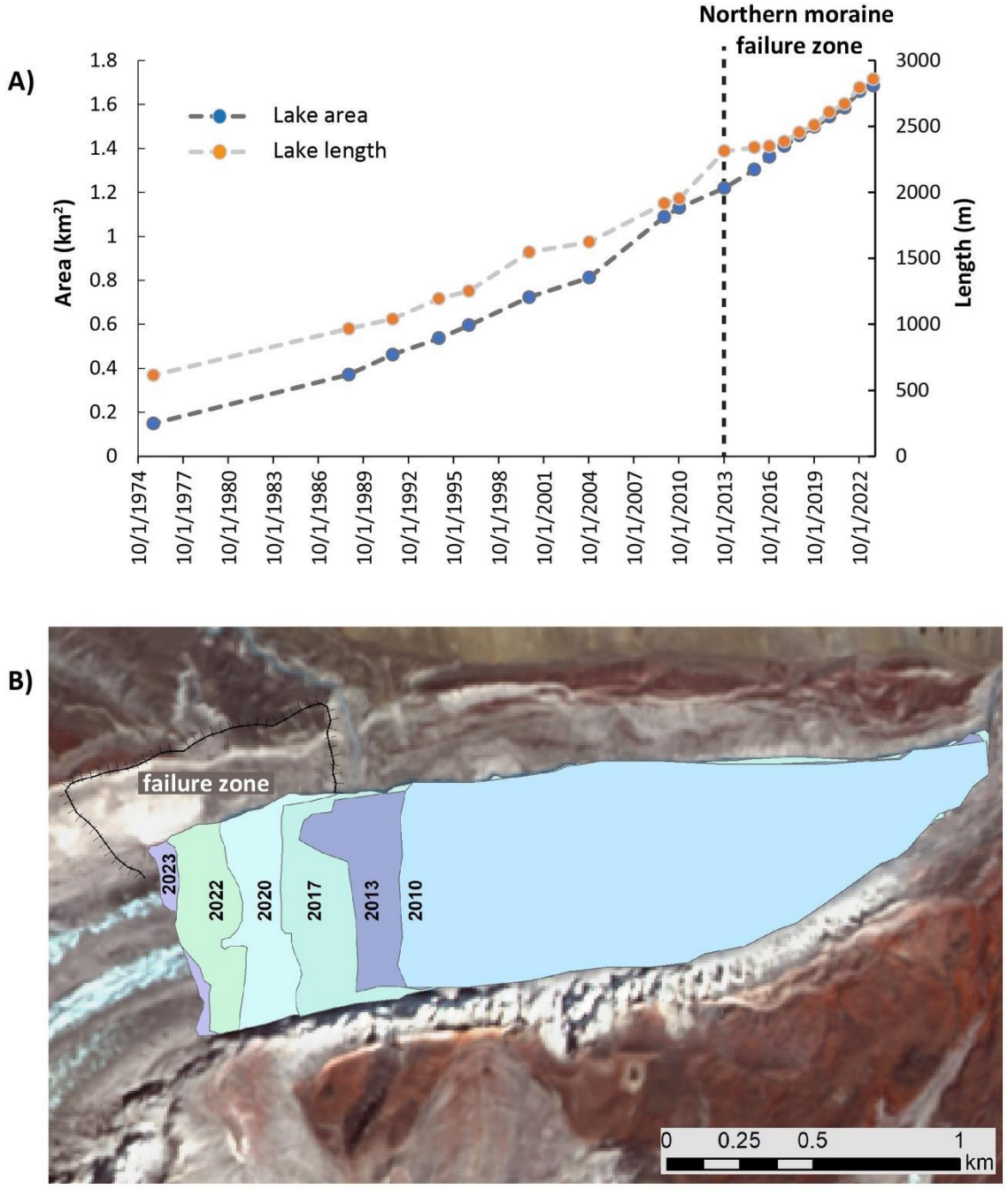

Fig. S20.

Pre-GLOF mapping of the collapsed moraine. Intact ground (IG) and scoured ground (SC) mapped using high-resolution PlanetScope imageries (3 m) from January 2023 to September 2023. Background imagery in all panels are © 2023 Planet Labs Inc.

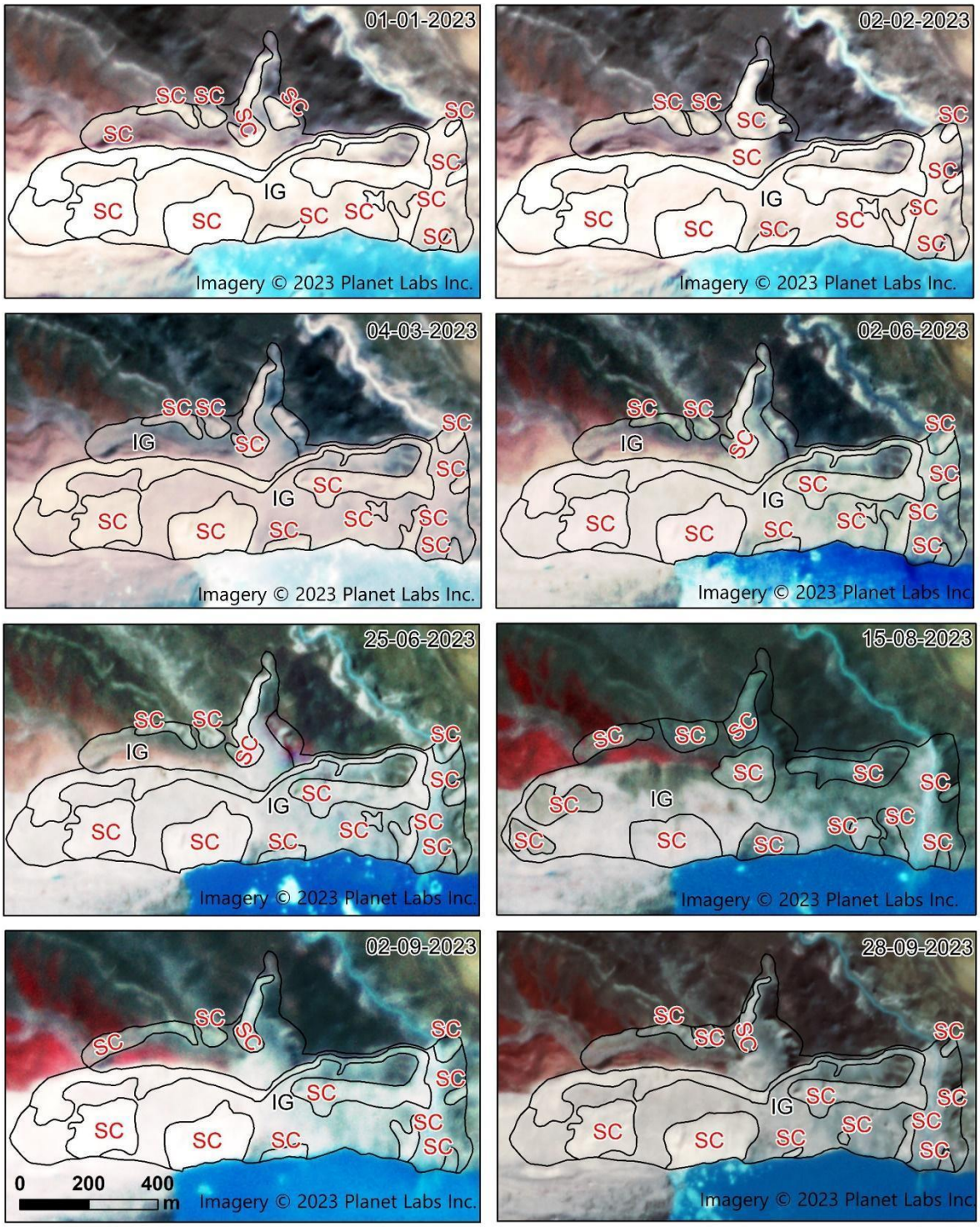

Fig. S21.

Spatial distribution of ERA5 daily specific humidity (g kg^{-1}) with winds at 700 hectopascal (hPa) isobaric surface over Eastern India and Bangladesh from 28 September to 6 October 2023. High humidity is seen over Sikkim, West Bengal, and Bangladesh from 1 October to 5 October 2023.

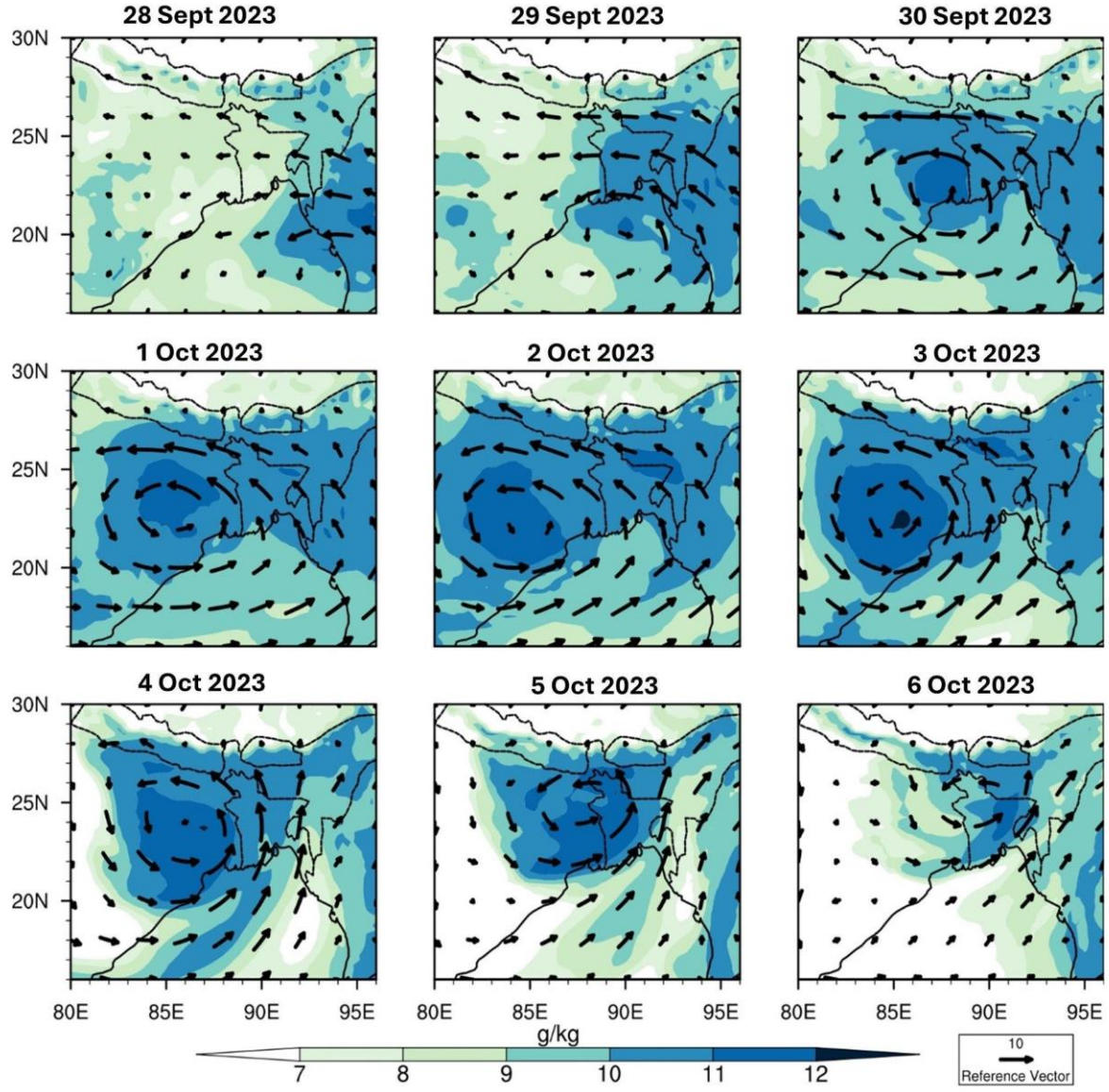

Fig. S22.

Comparison of various daily rainfall data (IMERG, ERA5, and ERA5-Land) with rain gauge data of (A) Lachen and (B) Dalia stations. The black curve represents the daily accumulation from 9 am to the next day at 9 am for the station. Note that the Lachen rainfall time series here is the average rainfall for a one-degree area centered around the nearest grid point from the station (27.7296° N, 88.5471° E), which yields the best correlation with station data. The rainfall time series for Dalia represents the rainfall at the nearest grid point from the respective station coordinates.

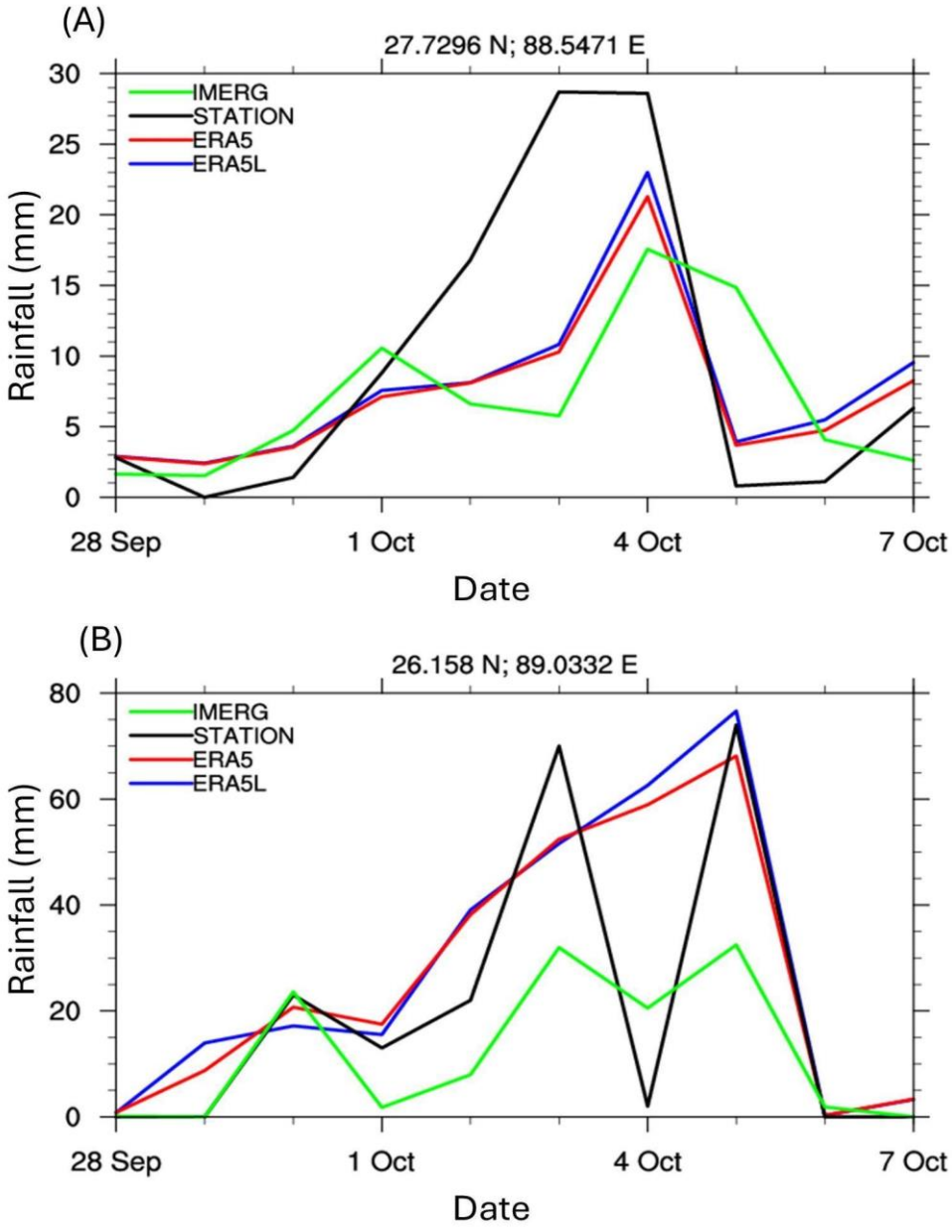

Fig. S23.

Daily rainfall time series over SLL of four different rainfall data sets: IMERGE (green), CPC NOAA (black), ERA5 high resolution (red), and ERA5-LAND (ERA5L) (blue) using four different approximations: (A) rain at grid points nearest to the station (NGRID), (B) Average rainfall of nine grid points centered around the lake, (C) IDWAVG of surrounding grid points rain. (D) BILINR rainfall over the lake from immediate surrounding grid points.

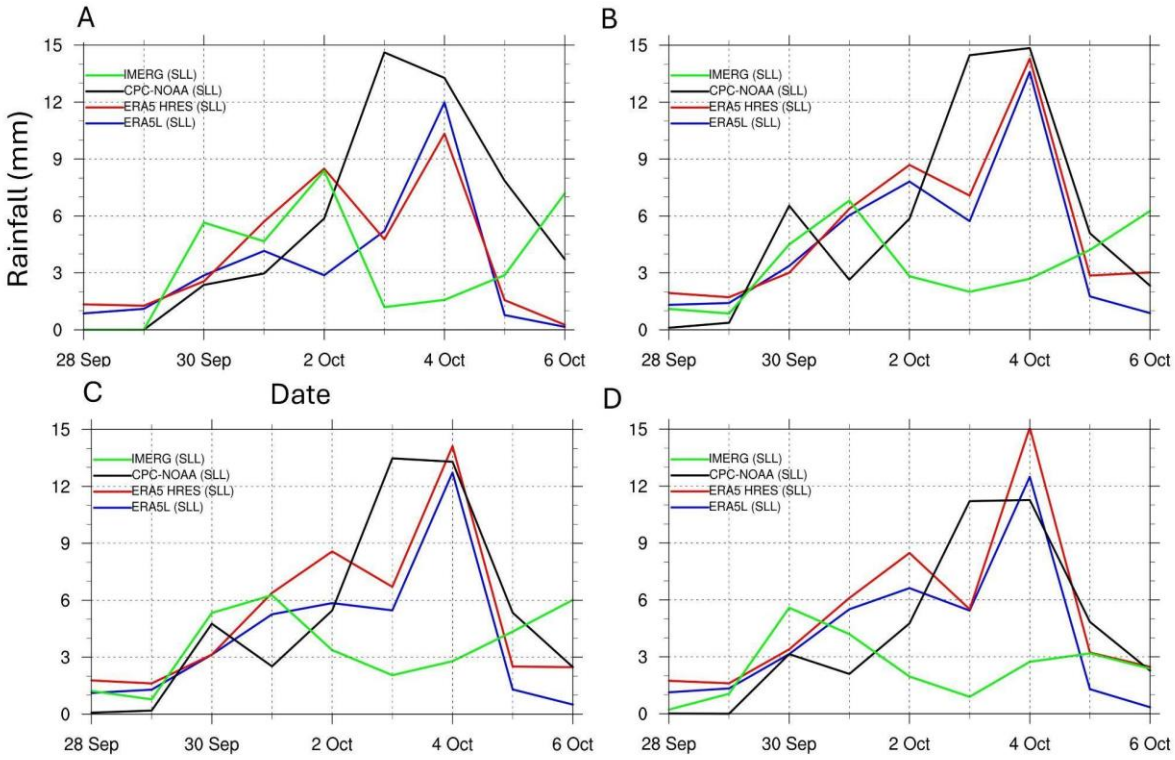

Fig. S24.

(A) Daily rainfall time series at Lachen station in Sikkim (red) and ERA5 1.2-degree area average centered around the station (blue) from 28 September to 8 October 2023. (B) Fourier power spectrum of the station (red) and ERA5 (blue) time series. (C) The probability density function of the station (red) and ERA5 (blue) rainfall data. (D) Comparison of various statistical parameters: mean, mean absolute error (MAE), root mean square error (RMSE), and Pearson and Spearman correlation coefficients between ERA5 (in mm) and station rainfall data (in mm).

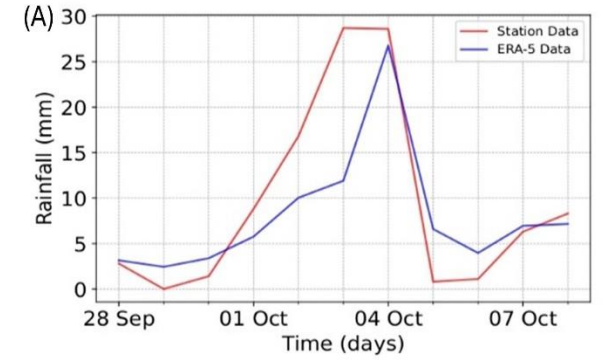

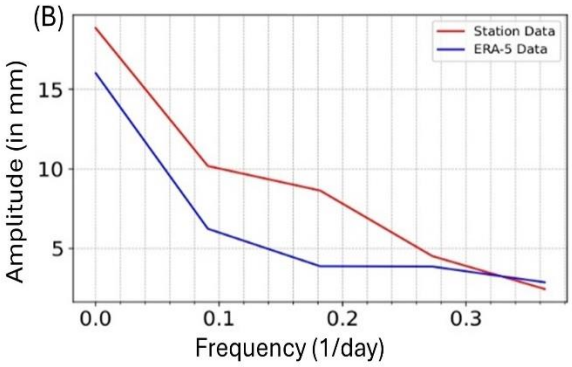

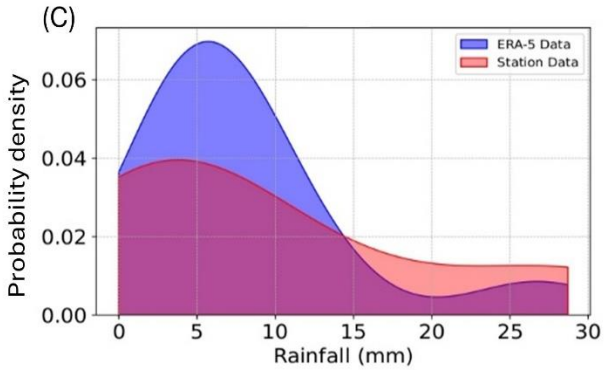

(D)

Metric	Value
Mean Station	9.42
Mean ERA5	8.01
MAE	3.97
RMSE	5.98
Pearson Correlation	0.85
Spearman Correlation	0.82

Fig. S25.

(A) Daily rainfall time series at Dalia station in Bangladesh (red) and ERA5 1.2-degree area average centered around the station (blue) from 28 September to 8 October 2023. (B) Fourier power spectrum of the station (red) and ERA5 (blue) time series. (C) The probability density function of the station (red) and ERA5 (blue) rainfall data. (D) Comparison of various statistical parameters: mean, mean absolute error (MAE), root mean square error (RMSE), and Pearson and Spearman correlation coefficients between ERA5 (in mm) and station rainfall data (in mm).

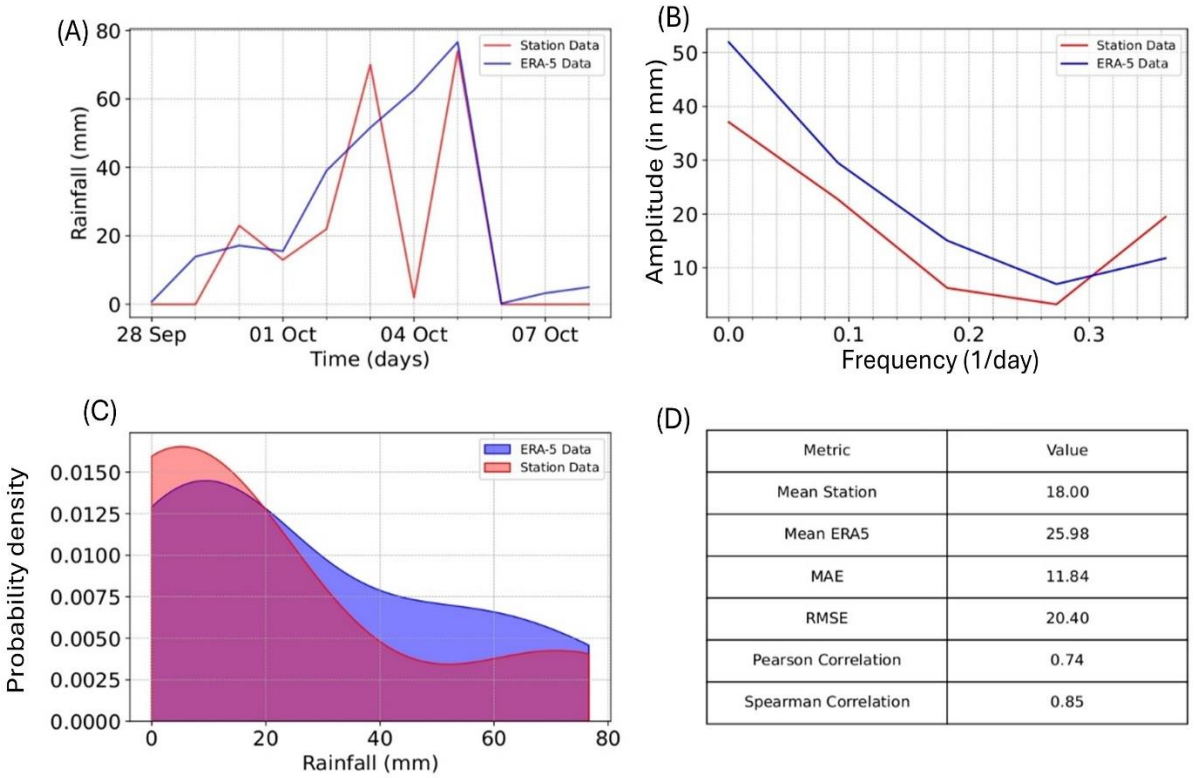

Metric	Value
Mean Station	18.00
Mean ERA5	25.98
MAE	11.84
RMSE	20.40
Pearson Correlation	0.74
Spearman Correlation	0.85

Fig. S26.

Daily (ending 09:00 IST) IMERG accumulated precipitation and winds at the 700 hPa isobaric surface from 28 September to 6 October 2023.

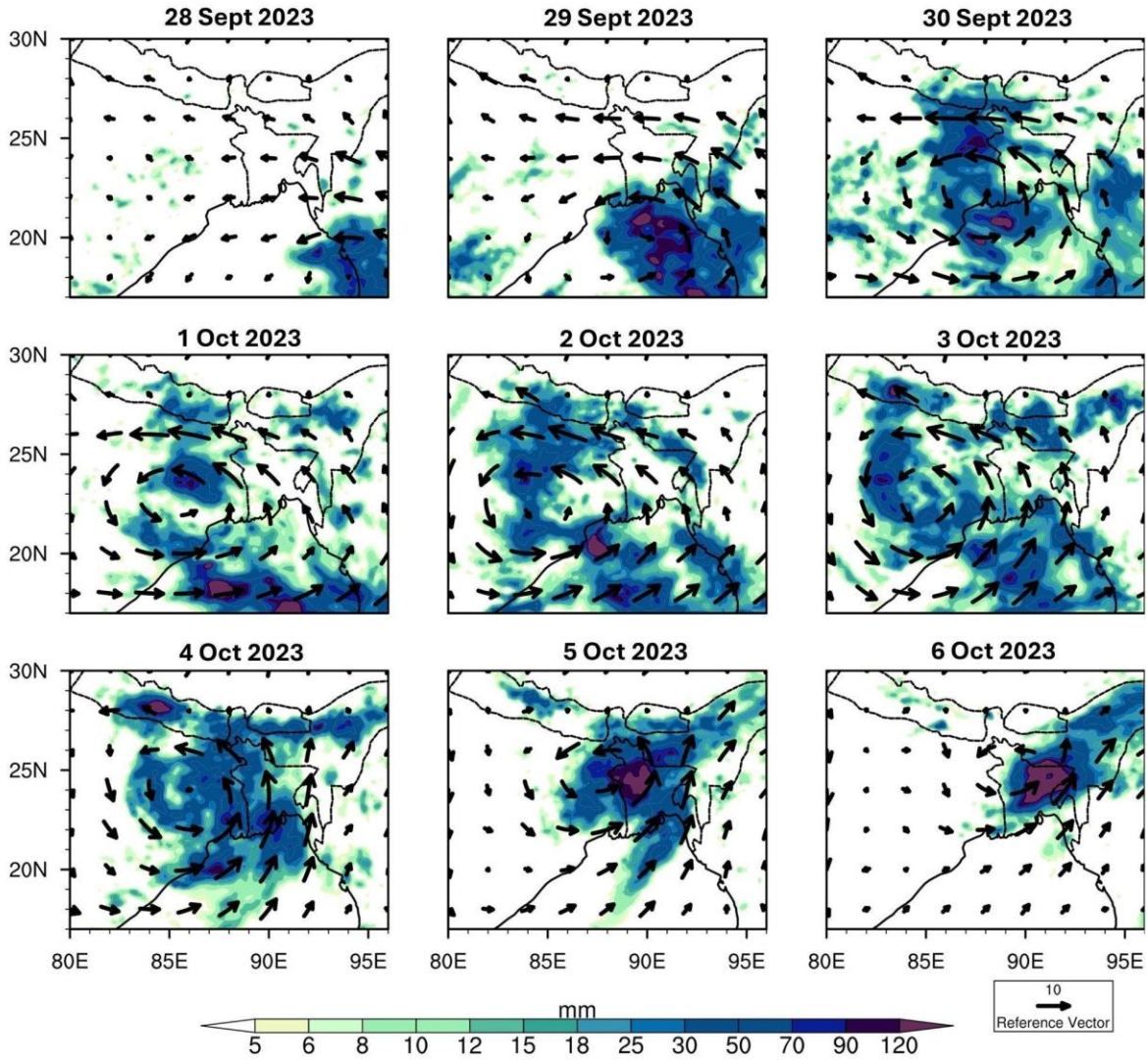

Fig. S27.

Pattern correlation coefficient (blue) between daily IMERG and ERA5 precipitation over the region 10°N-30°N, 70°E-100°E from 28 September to 7 October 2023, accompanied by significance levels calculated using a two-tailed student t-test (red).

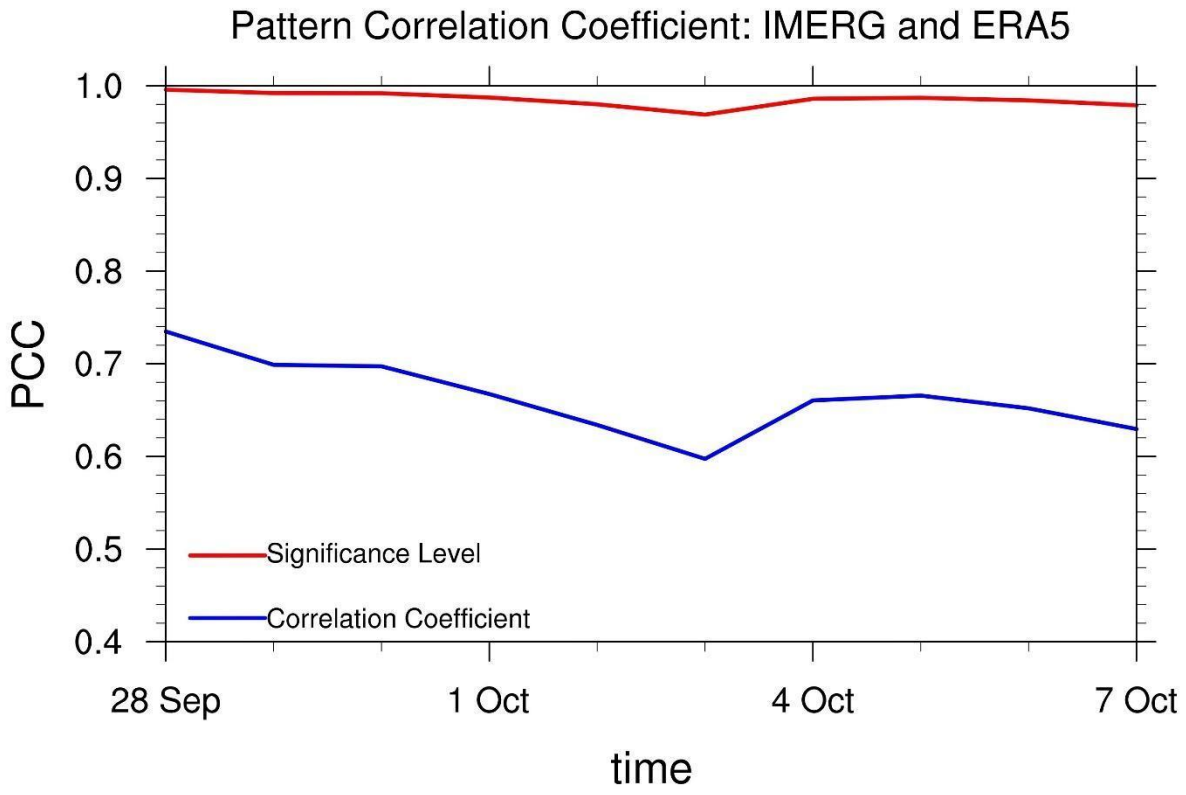

Fig. S28.

Post-GLOF landslides. (A) Locations of landslides triggered by GLOF, mapped using post-event high-resolution (0.7 m) Pléiades imagery (24, 29, and 31 October and 5 November 2023) and 3 m PlanetScope imagery (9 to 19 October 2023). (B-J) Field photographs of selected post-GLOF landslides (L9, L11, L12, L13, L14, L15, L33, L34, L35, L39 and L43). Photo credits: Rajeev Rajak and Praful Rao (co-authors). (K) Comparison of Pre- and Post- GLOF imagery showing the largest GLOF-triggered landslides (L33 and L35) that damaged buildings and highways. Background imagery in both panels shown as False Color Composite (FCC) are © 2023 Planet Labs Inc. Building footprints were obtained from (*117*, *118*). Highways were obtained from (*119*) and are © OpenStreetMap contributors. (L) Bar chart showing the total number of landslide-affected buildings (total=208), the number of affected buildings constructed in the last decade (total=117), and landslide-damaged road network (~6.4 km). (M) Formation of the landslide-dammed lake formed 35 km downstream of SLL due to deposits from L6 blocking the Teesta River. Background imagery in both panels are © Pléiades @ CNES 2023, Distribution AIRBUS DS.

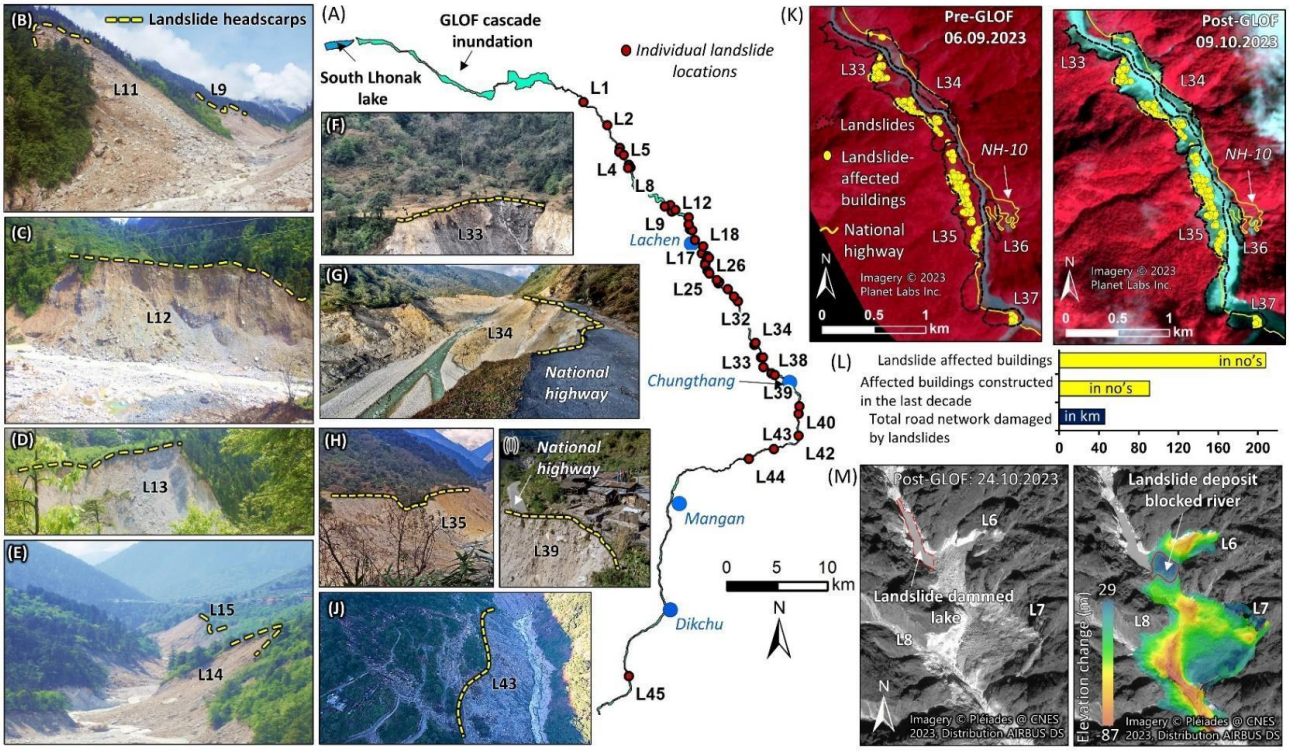

Fig. S29.

(A) Imagery showing the landslide-dammed lake existing as on 24 May 2024. (B) Partial lake drainage through a channel cutting through the landslide deposits is seen as on 15 July 2024. Background imagery in both panels shown as FCC are © 2024 Planet Labs Inc.

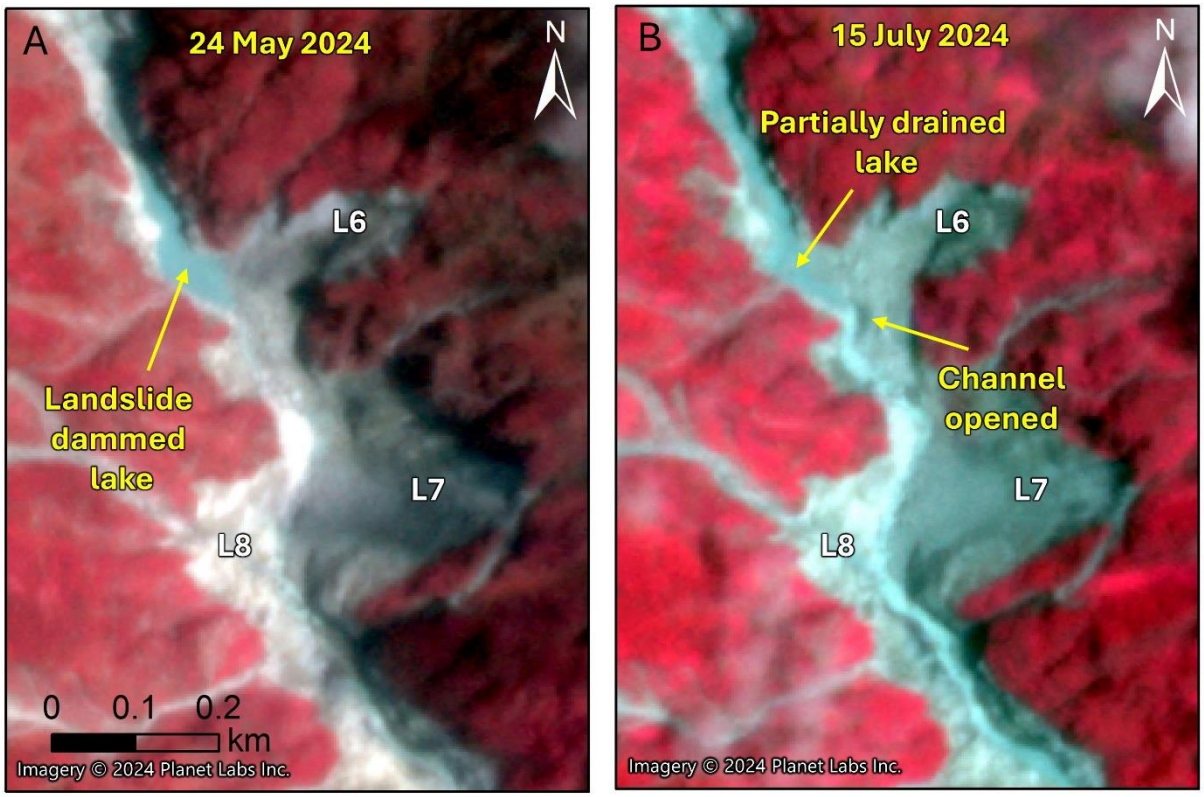

Fig. S30.

GLOF-triggered landslides (L1-23; L24-L44 shown in fig. S28) mapped using post-GLOF Pléiades imageries (0.7 m) (imagery acquired on 24, 29, and 31 October and 5 November 2023). Background imagery in all panels are Pléiades © CNES (2023) Distribution Airbus DS.

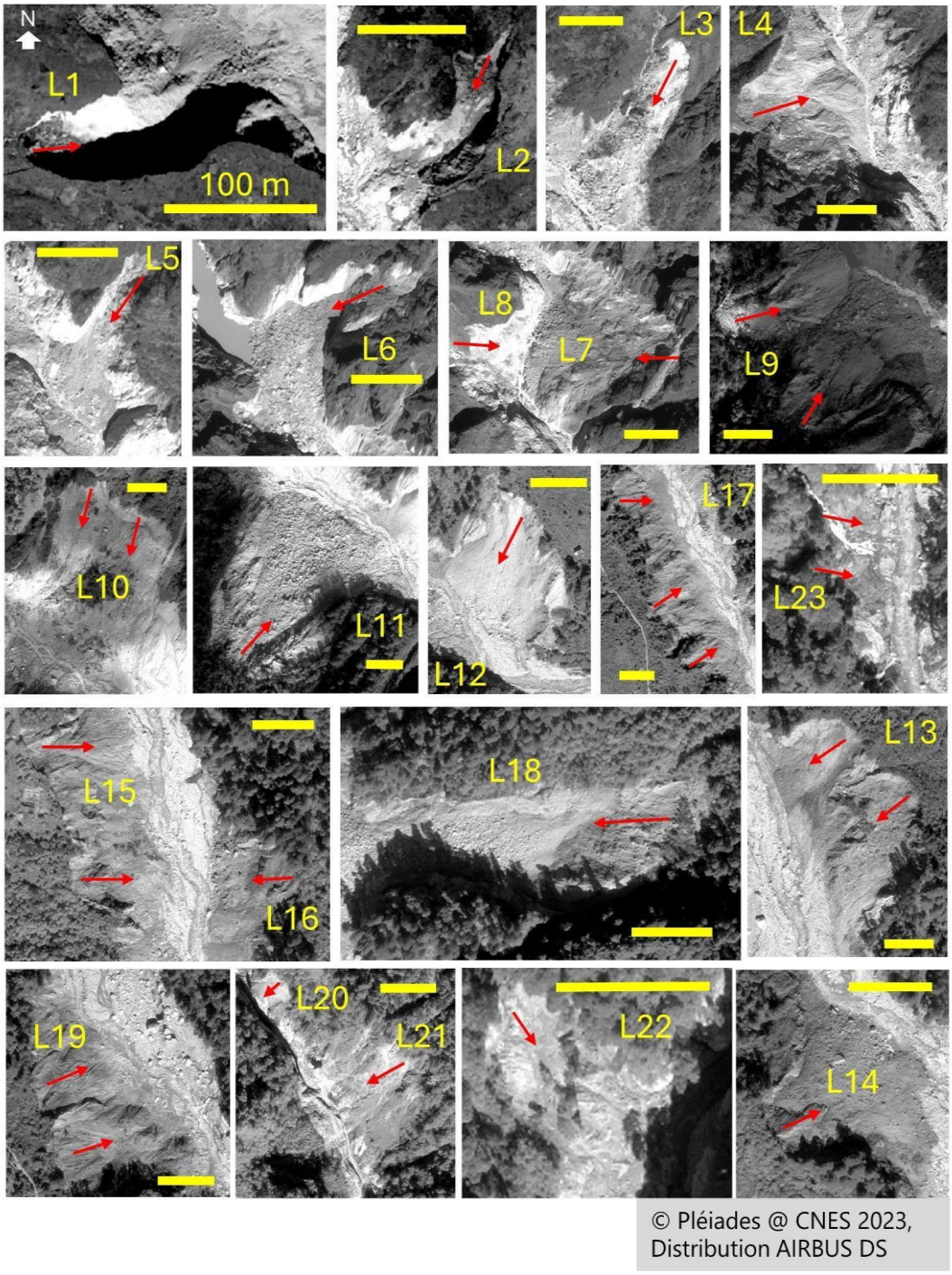

Fig. S31.

GLOF-triggered landslides (L24-L44) mapped using post-GLOF Pléiades imageries (0.7 m) (imagery acquired on 24, 29, and 31 October and 5 November 2023). Background imagery in all panels are Pléiades © CNES (2023) Distribution Airbus DS.

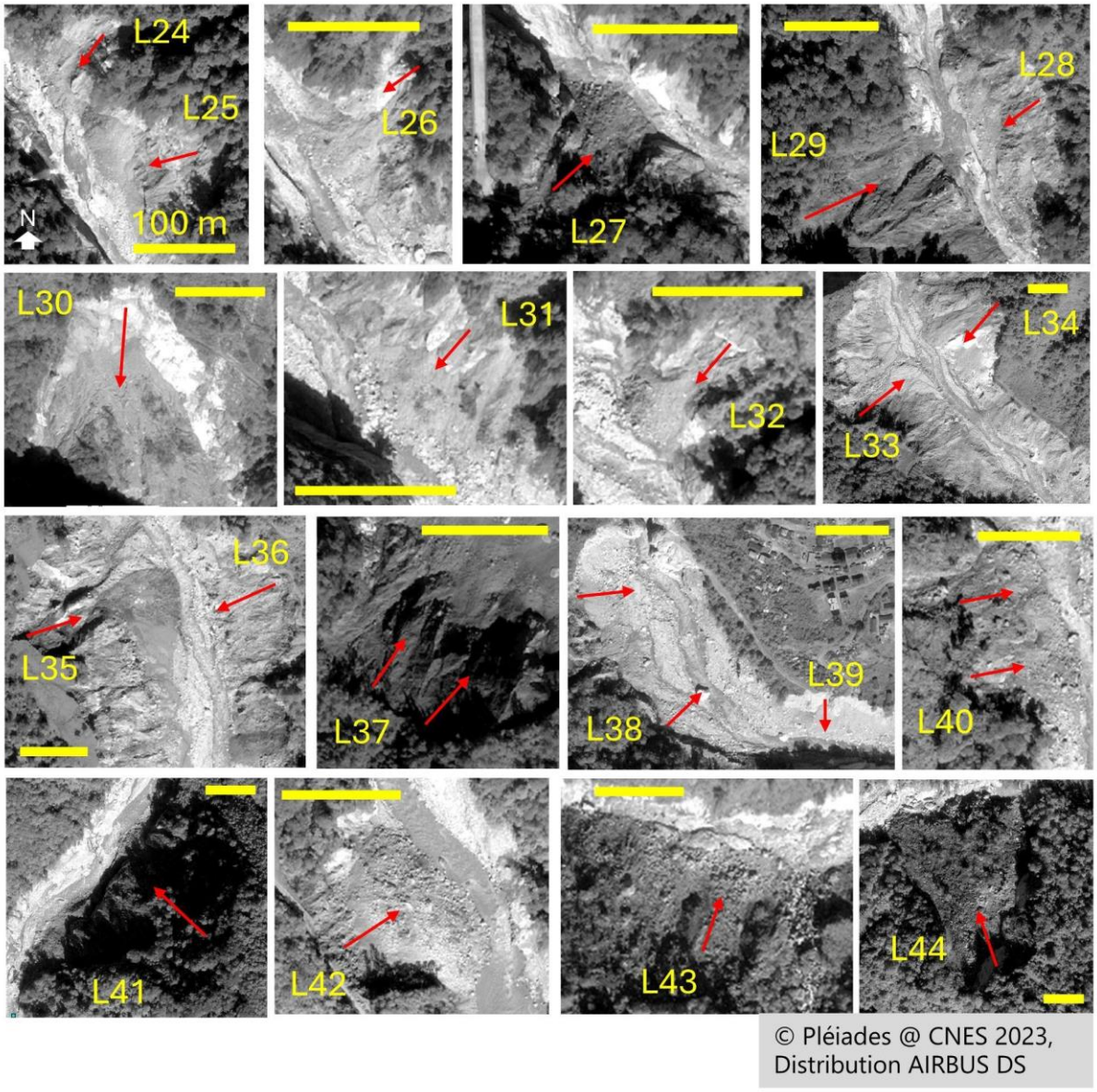

Fig. S32.

(A-I) Pléiades imagery in FCC (0.7 m) (acquired on 24, 29, and 31 October and 5 November 2023) showing GLOF-triggered landslides and affected road network. Background imagery in panels (A-I) are Pléiades © CNES (2023) Distribution Airbus DS. (J) Bar chart showing the road length damaged by individual landslides. The road networks shown in yellow dotted line are © OpenStreetMap Contributors.

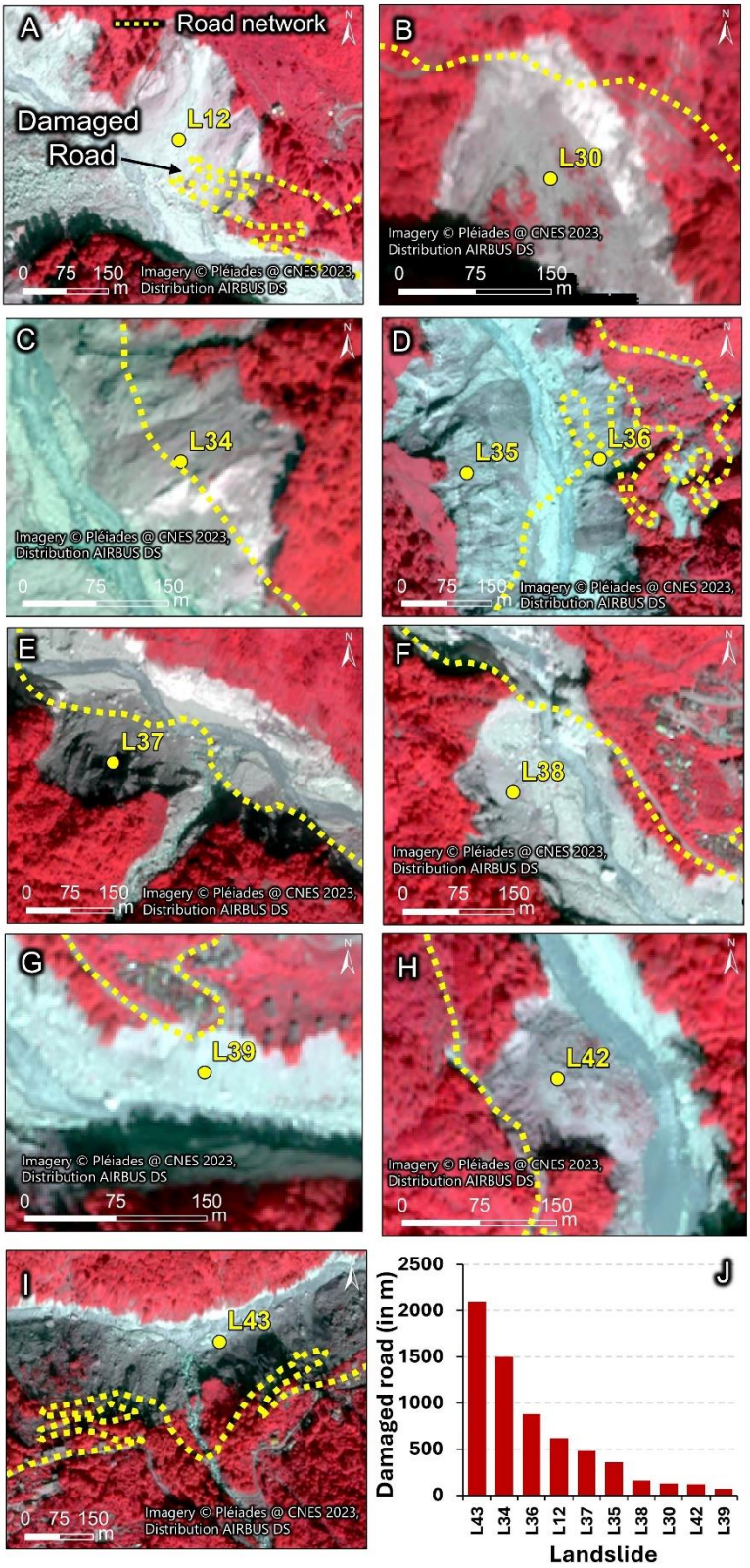

Fig. S33.

(A-F) Pléiades imagery in FCC (0.7 m) (acquired on 24, 29, and 31 October and 5 November 2023) showing GLOF-triggered landslides and damaged buildings. Background imagery are © CNES (2023) Distribution Airbus DS. (G) Bar chart showing the number of buildings damaged by individual landslides. The building footprints (v3) for May 2023 are sourced from (*117*, *118*). For data accuracy, refer to (*118*).

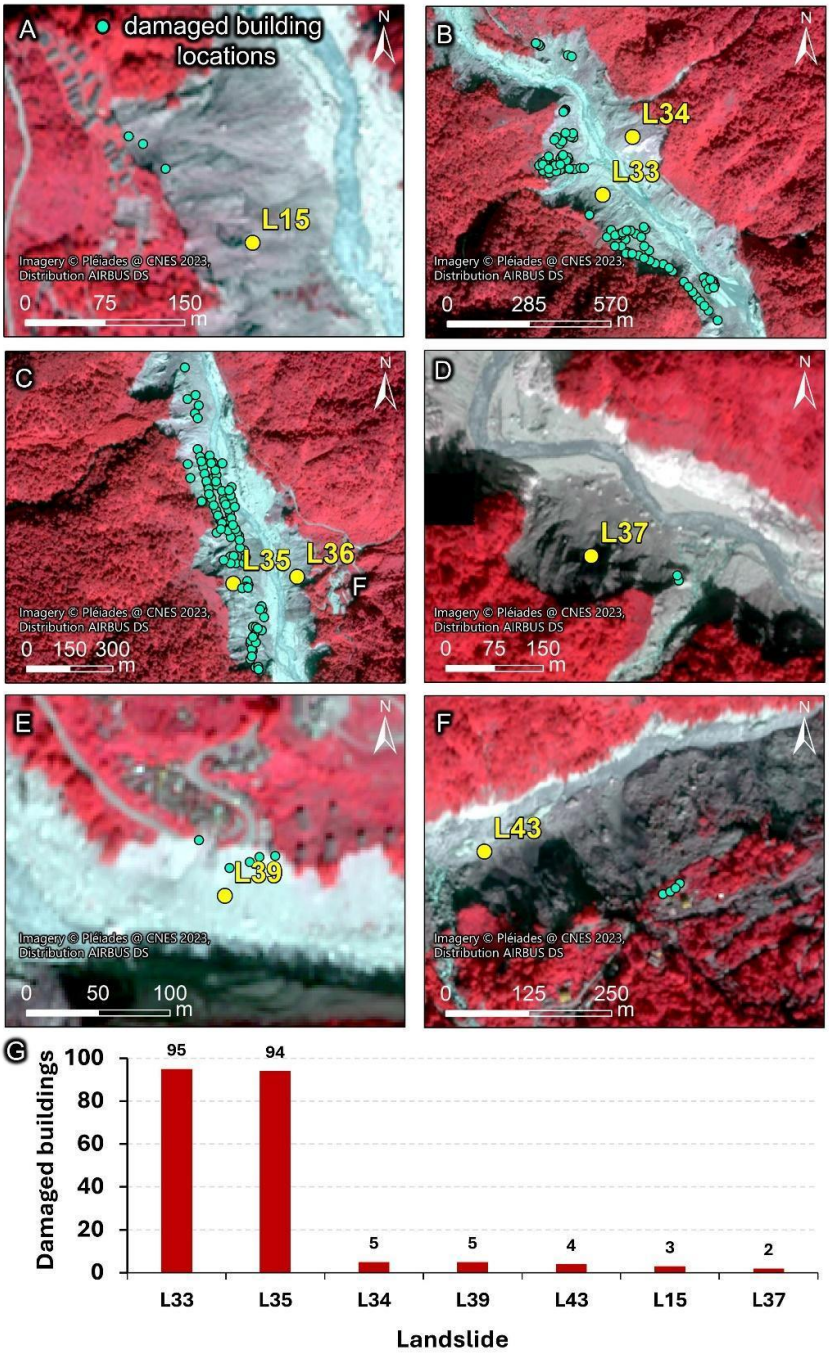

Fig. S34.

(A) Pléiades imagery in FCC (0.7 m) showing the Naga landslide (L43), where flood-triggered lateral erosion of the valley caused slumping and offset roads and concrete walls by several meters. Background imagery Pléiades © CNES (2023) Distribution Airbus DS. (B) Field photographs of the Naga landslide showing the offset of roads. (C) Field photograph showing the road damaged by the landslide. (D) Field photographs of the Naga Landslide showing the offset concrete structures. (E) Pre- and post-GLOF dynamics of the Naga landslide. Increasing offsets marked in yellow arrows were observed in 2024 monsoons, months after the landslide was triggered in October 2023. Background imagery © 2023, 2024 Planet Labs Inc. Photo credits (panels B, C, and D): Praful Rao (co-author).

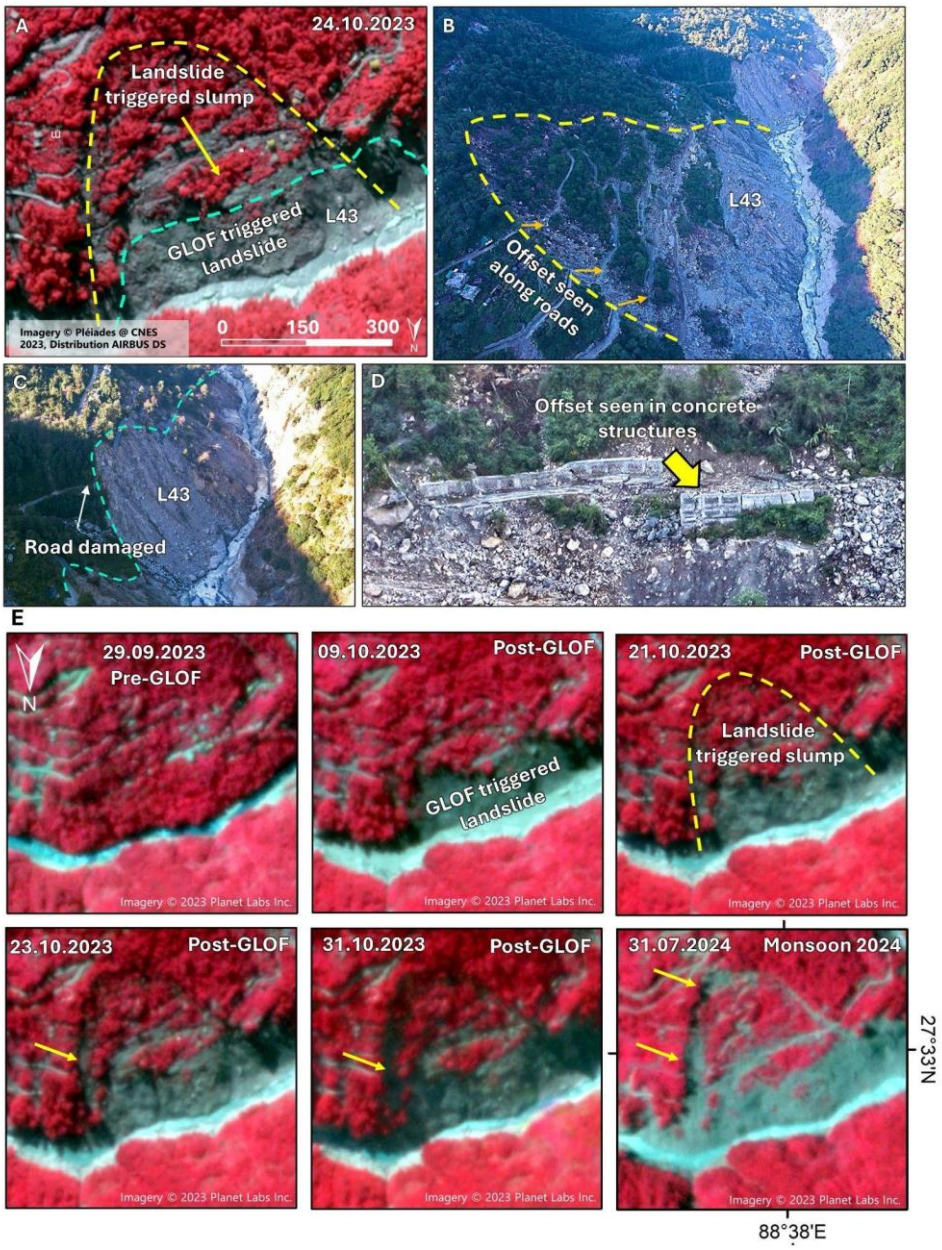

Fig. S35.

(A) Pre-GLOF PlanetScope imagery (6 September 2023) (3 m) showing the distance of Lachen settlement (27.73°N, 88.54°E) from the banks of Teesta River. Background FCC imagery is © 2023 Planet Labs Inc. (B) Post-GLOF Pléiades imagery in FCC (24 October 2023) (0.7 m), showing the widened river valley due to GLOF-triggered landslides and lateral erosion; landslide scarps approached Lachen settlement. Background FCC imagery Pléiades © CNES (2023) Distribution Airbus DS. (C) Field photograph showing the GLOF-triggered landslide (L17) and the Lachen settlement. Photo credit: Rajeev Rajak (co-author).

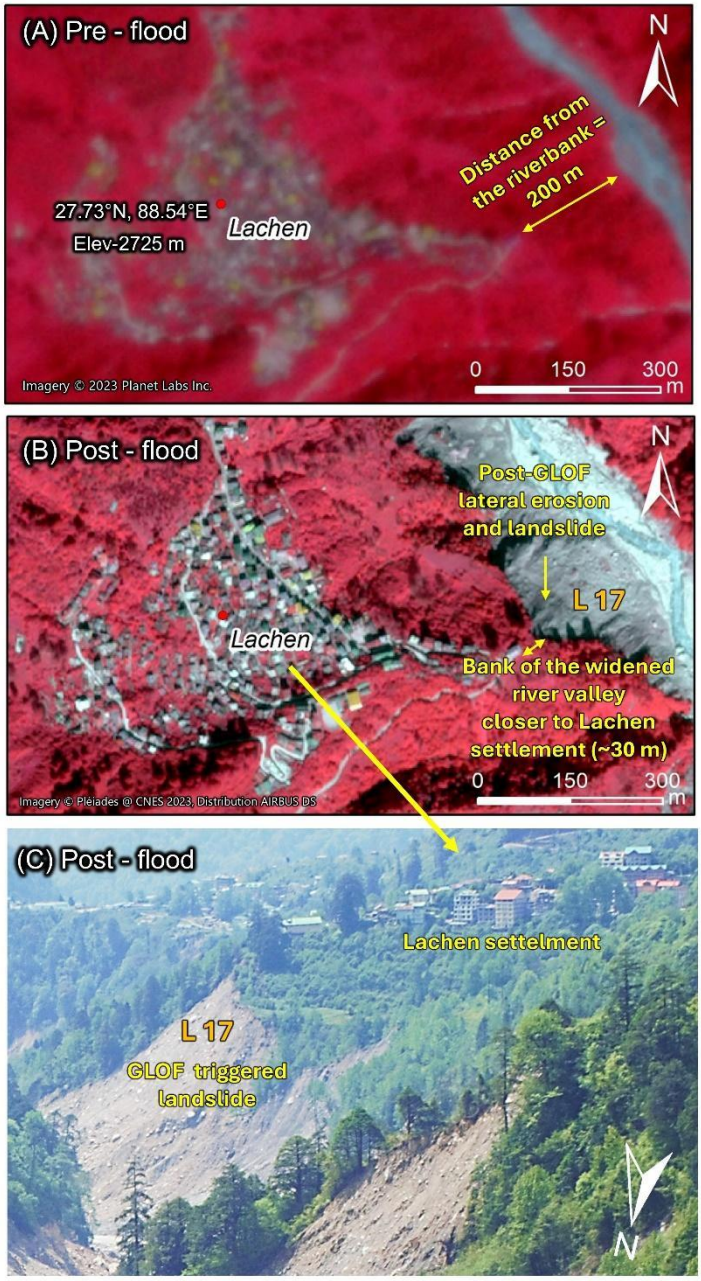

Fig. S36.

Reconstructed GLOF velocity (also see Fig. 3F) and eroded volumes (observed and calculated from DoD; also see Fig. 5) for every 5 km distance along the GLOF flow path from SLL to Chungthang, located 67.5 km downstream.

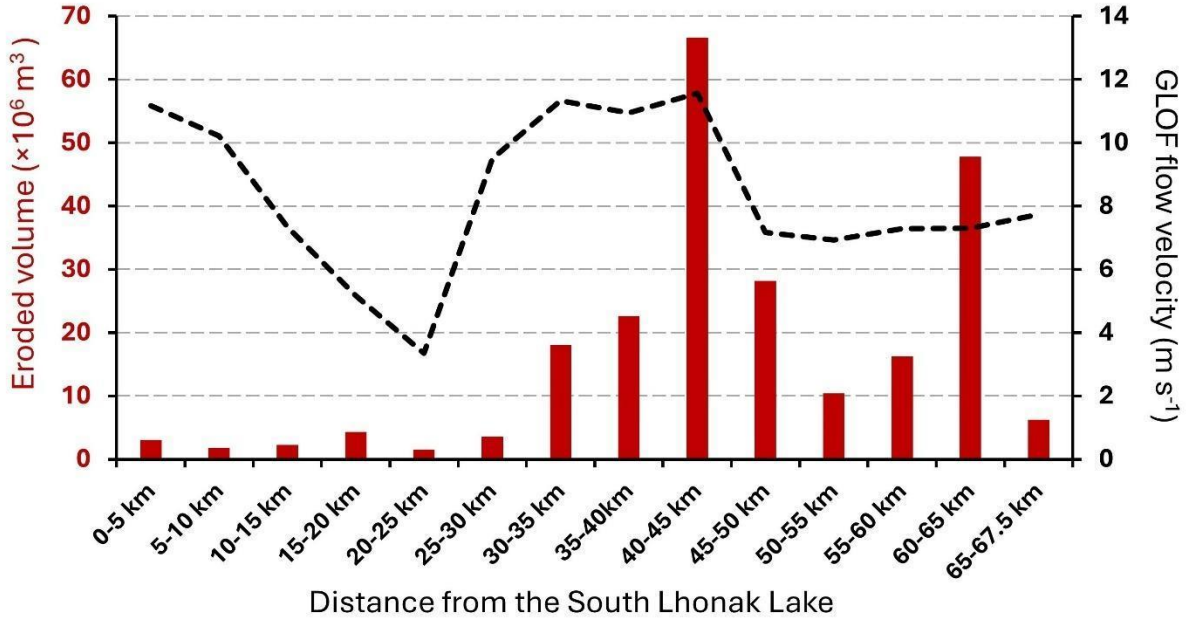

Fig. S37.

Field photographs taken along the Teesta River showing erosion caused by the 3 October 2023 GLOF cascade. Latitude and longitude are given at the center top, and elevation is indicated in the right bottom corner of each panel. Photo credits: Praful Rao (co-author).

Fig. S38.

(A) Map showing the locations of the damaged bridges and hydropower projects along the Teesta River. (B-F) Post-GLOF field photographs showing impact on five hydropower projects: Teesta III, Teesta V, Teesta VI, Teesta Low Dam III, and Teesta Low Dam IV. Photo credits: Panel B and C: Praful Rao (co-author); Panel D: Rajeev Rajak (co-author); and panel E and F: Nazimul Islam (co-author).

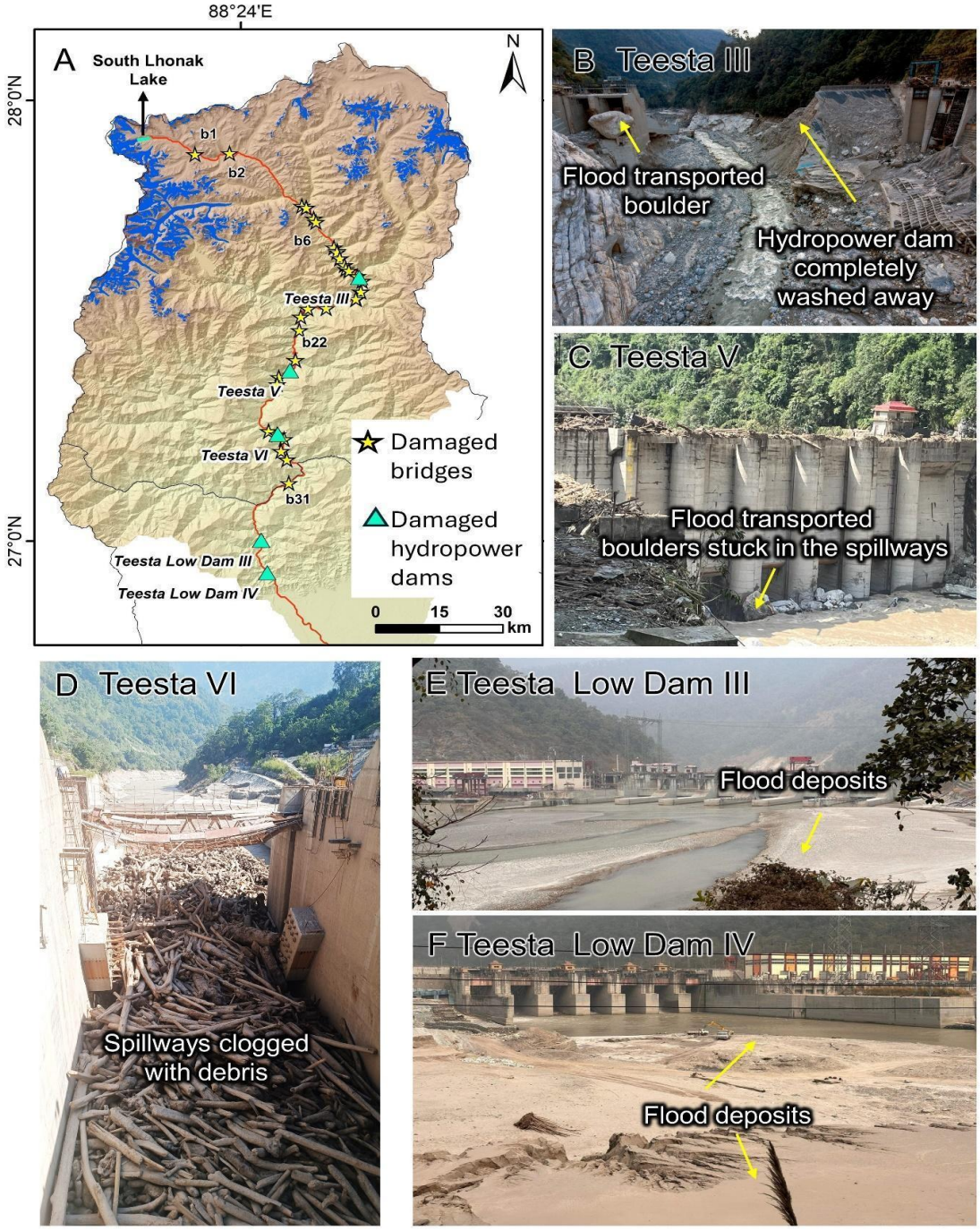

Fig. S39.

Field photographs showing the bridges damaged by the GLOF cascade along the Teesta River. Each panel provides the following details: latitude and longitude (top center), elevation (top right corner), and locality name (bottom left). Photo credits: Praful Rao and Rajeev Rajak (co-authors). Yellow arrows show the damaged bridges.

Fig. S40.

(A) Map showing the locations of the photographs in panels Cam 1- 7, showing the post-GLOF impacts. Each panel includes the following details: latitude and longitude (top center), elevation (top right corner), and locality name (center). Photo credits: Rajeev Rajak and Praful Rao (co-authors).

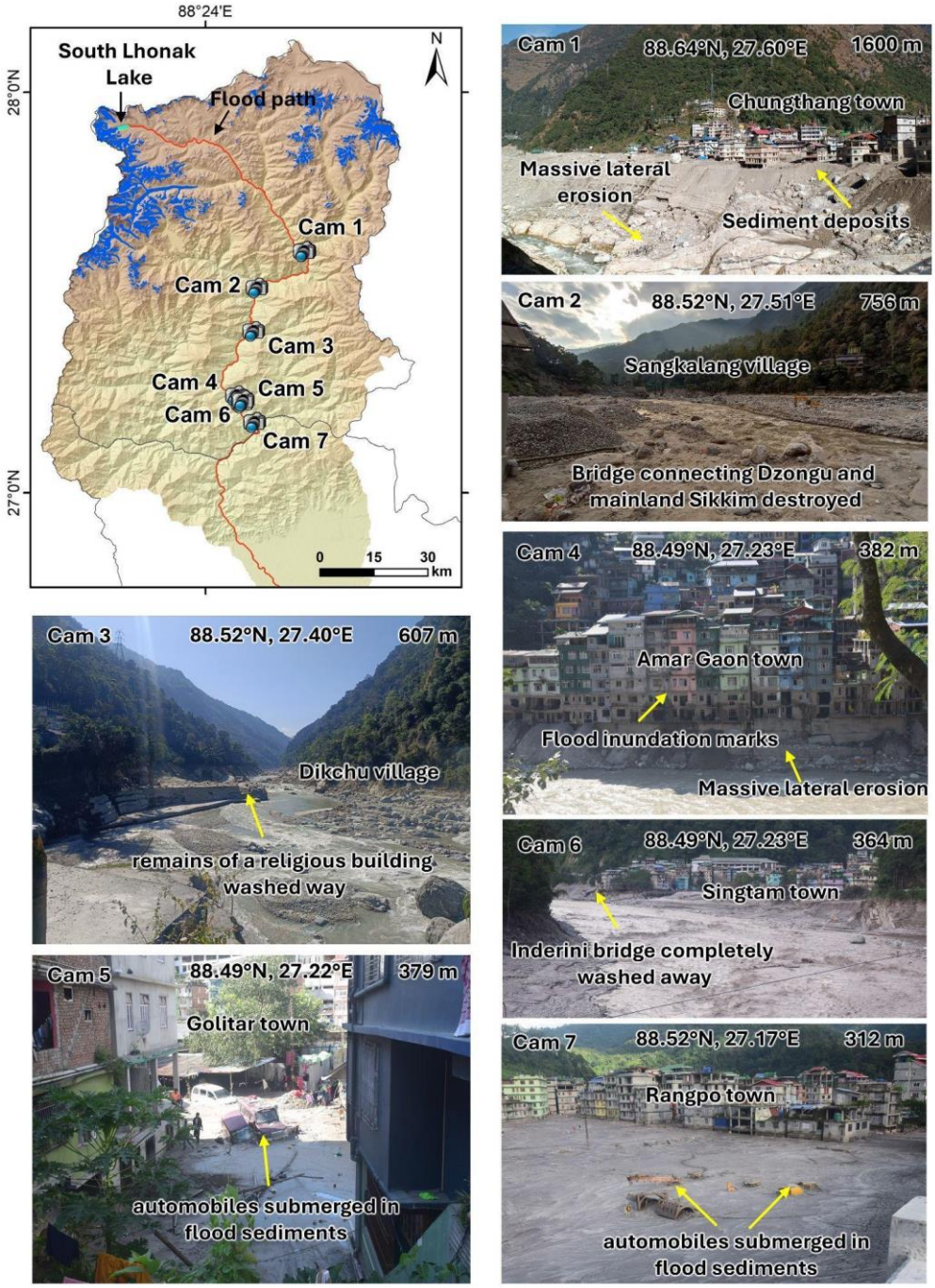

Fig. S41.

(A) Map showing the flood-affected districts in Bangladesh; colored dots show the location of the Dalia discharge station and the field photograph (as shown in panel E). (B) Recorded water levels and rainfall at the Dalia station from 17 September 2023 to 29 October 2023 (*120*). (C) Pre- and post-flood PlanetScope imagery showing an increase in turbidity of the Teesta River. Background imagery in both panels are shown as FCC and are © 2023 Planet Labs Inc. (D) Sediment discharge recorded at the Dalia station at 7-day intervals from 17 September 2023 to 29 October 2023 (*120*). (E) Field photograph of the Char Isli area at Gangachara upazila in Rangpur showing bank erosion and high sediment-laden water flow in the Teesta River; photo taken on 6 October 2023 (Image reused with permission from P Bhattacharya).

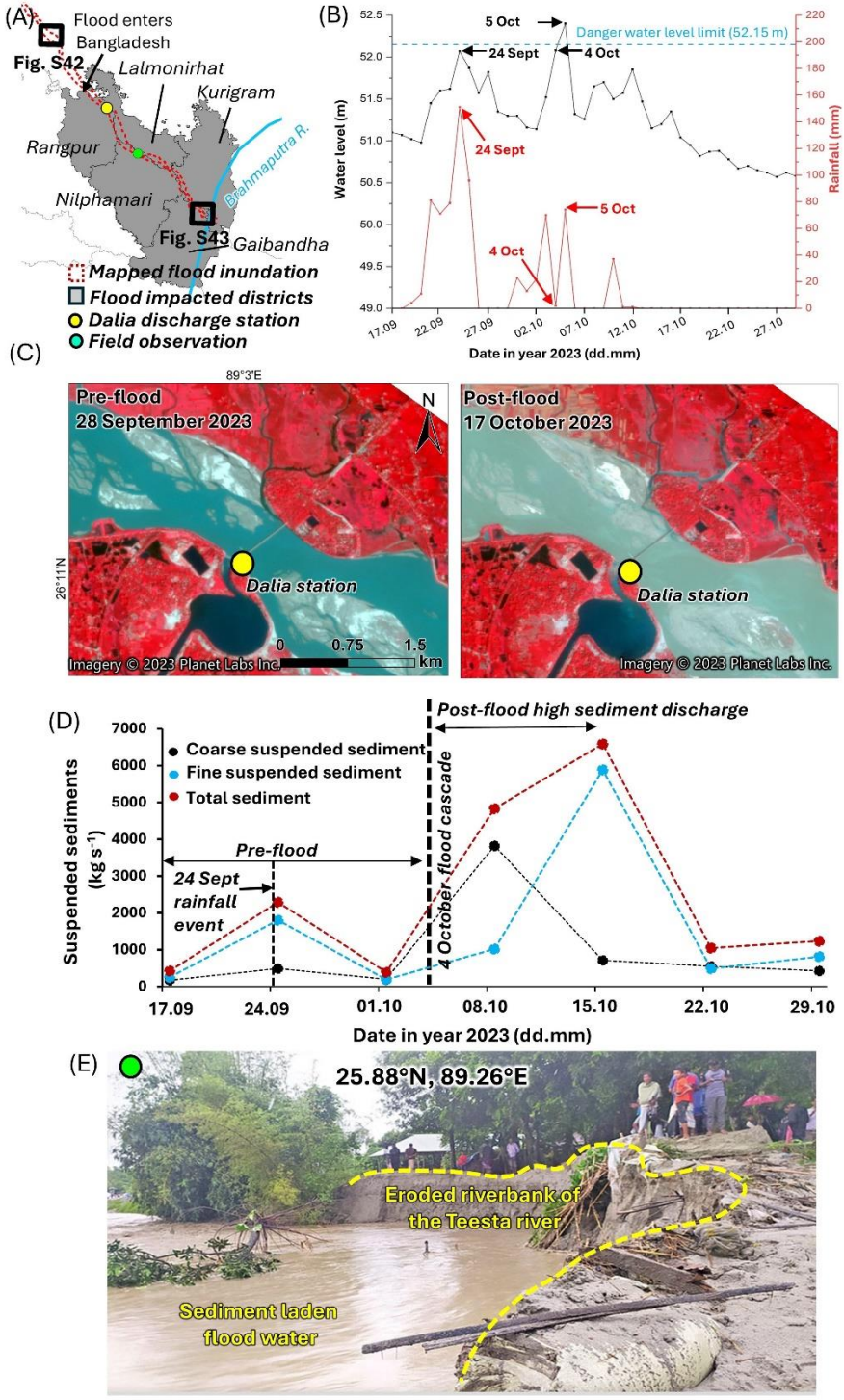

Fig. S42.

Pre- and post-flood FCC of Copernicus Sentinel-2 level 2A from 01 October 2023 to 10 November 2023 showing the post-flood turbid water and increased inundation (see Fig. S41A for location).

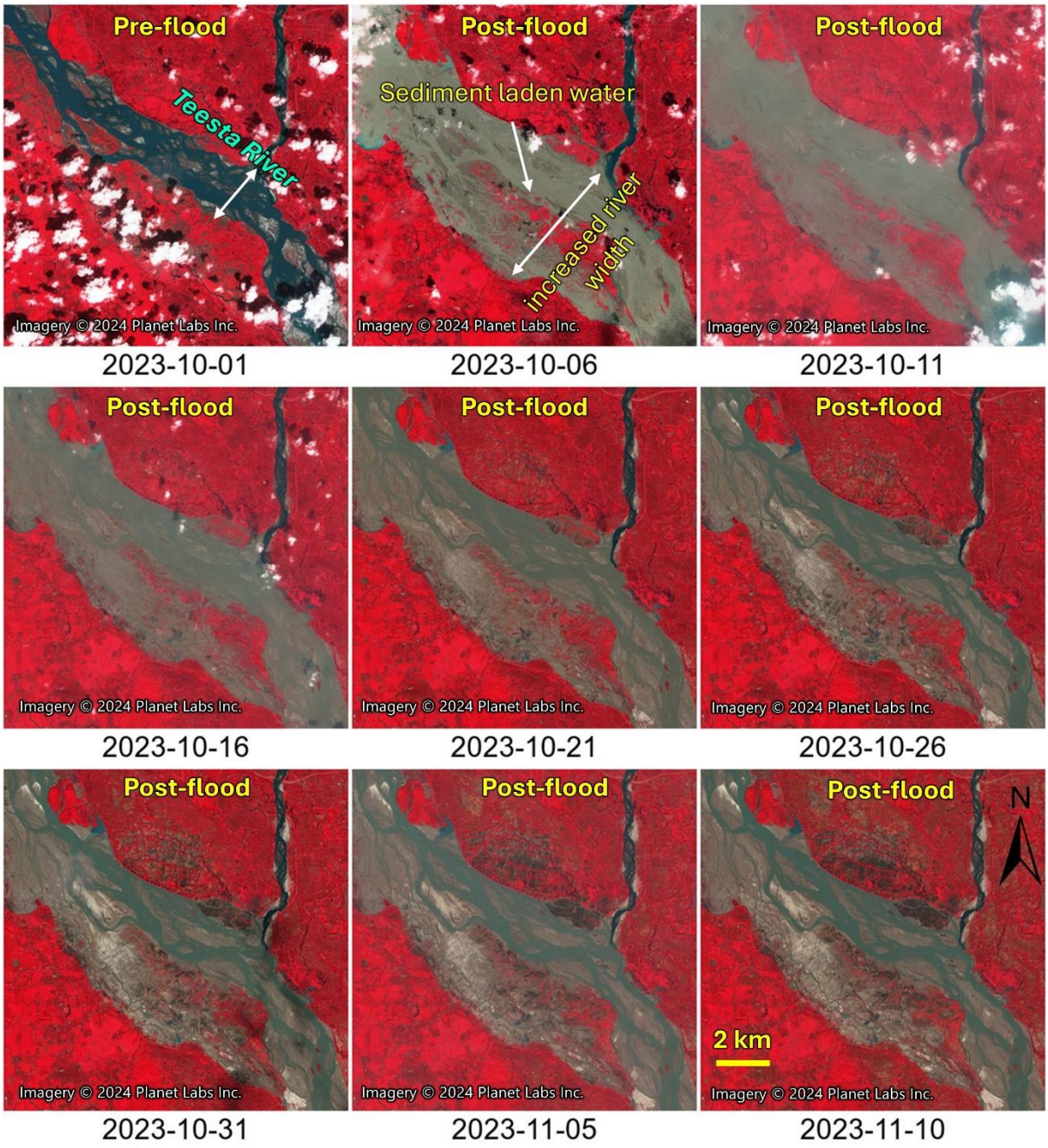

Fig. S43.

Pre- and post-flood FCC of Copernicus Sentinel-2 level 2A from 01 October 2023 to 10 November 2023 showing the post-flood turbid water of the Teesta River at the confluence of the Teesta and Brahmaputra rivers (see Fig. S41A for location).

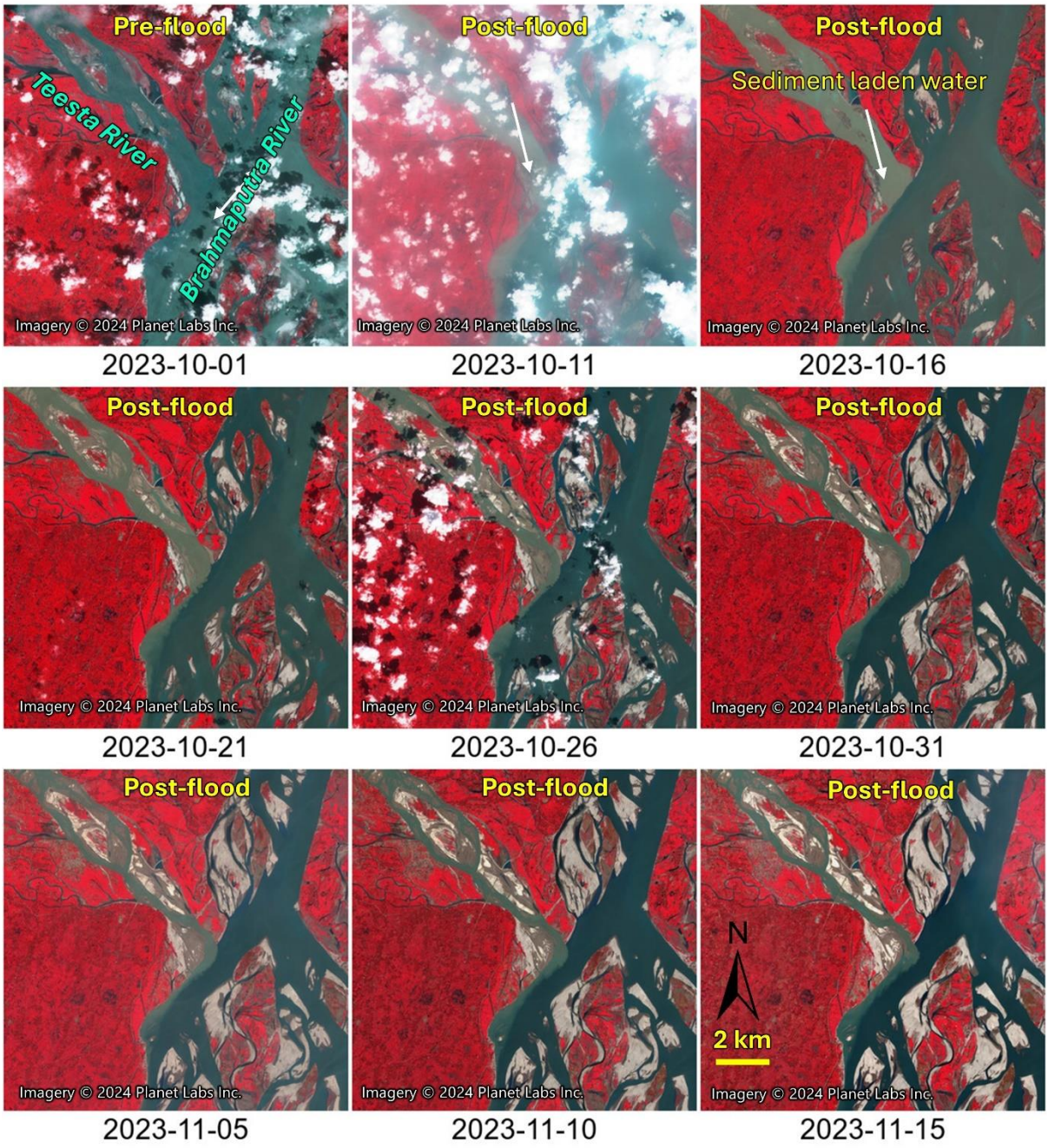

Fig. S44.

Post-failure surface displacement map showing median velocity (m a^{-1}) from October 2023 to June 2024 for the northern lateral moraine of SLL. The highest displacement area is located within the 3 October 2023 scar of the collapsed northern moraine.

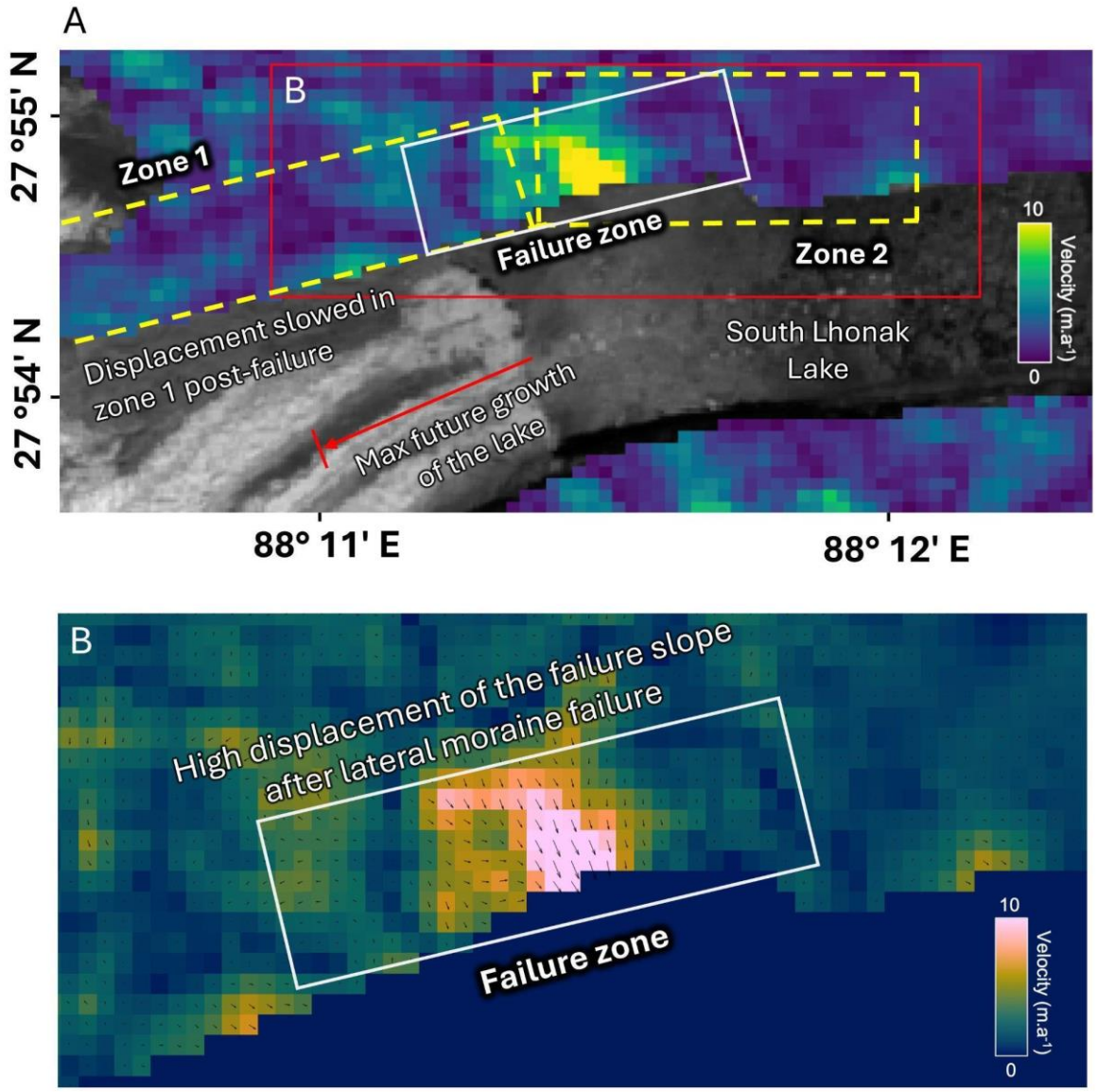

Fig. S45.

Post-GLOF mapping of the scar of the collapsed northern lateral moraine. Intact ground (IG) and mass movements (MM) mapped using high-resolution Planetscope imagery from 6 October 2023 to 1 April 2024. Background imagery in the top four panels are © 2023 Planet Labs Inc. and the bottom four are © 2024 Planet Labs Inc.

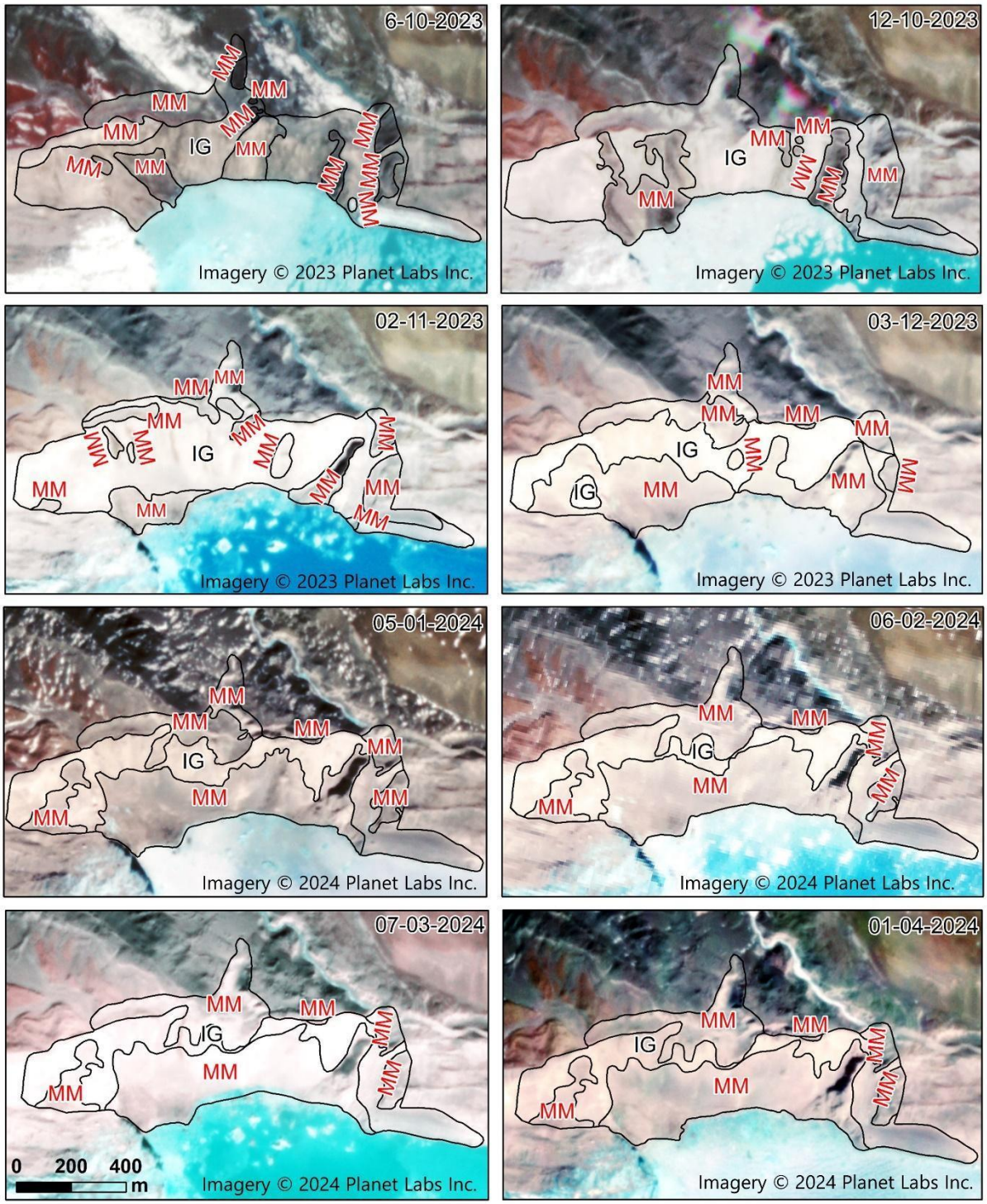

Fig. S46.

Overflowing water from the Teesta River inundated the Darjeeling-Kalimpong road near Teesta Bazaar during the July 2024 monsoon. This flooding is attributed to sediment deposition from the 3-4 October 2023 floods that elevated the riverbed by several meters, leading to early bankfull conditions. Photo credits: Save the Hills; Praful Rao (co-author).

Fig. S47.

Damaged National Highway 10 (NH-10) at several places along the Teesta River during the 2024 monsoons. Slumping and subsidence of the highway are seen at several locations. Photos taken on 21 July 2024. Photo credits: Praful Rao (co-author).

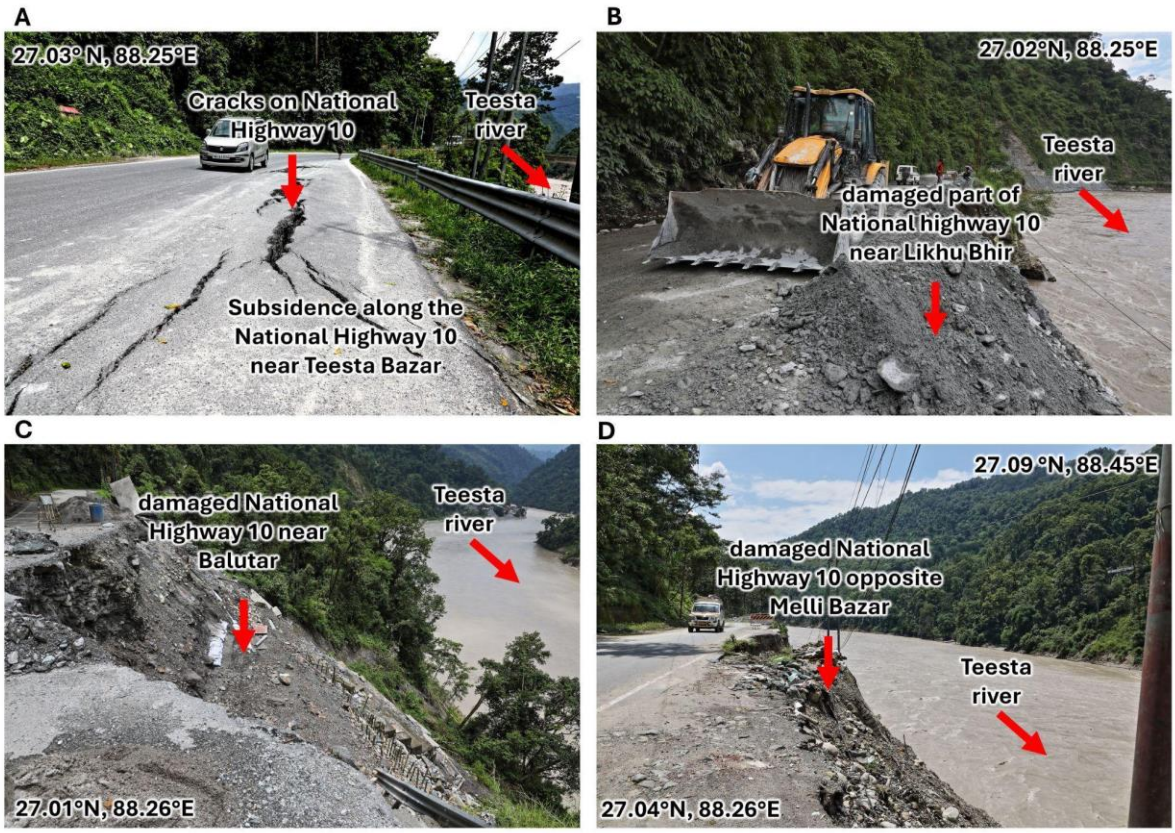

Table S1. Triggered landslides and landslide-impacted buildings; landslides that impacted buildings are highlighted in grey. The latitude, and longitude of individual landslides are given. Also given are the number of buildings impacted by each landslide along with the impacted buildings constructed in the last decade.

Landslide ID	Longitude [°E]	Latitude [°N]	Number of impacted buildings by flood-triggered landslides	flood-triggered landslide-impacted buildings constructed in the last decade
L1	88.4418	27.8581	0	0
L2	88.4654	27.8371	0	0
L3	88.4777	27.8167	0	0
L4	88.4772	27.8132	0	0
L5	88.4817	27.8102	0	0
L6	88.4869	27.8016	0	0
L7R	88.4881	27.799	0	0
L8	88.4859	27.7987	0	0
L9	88.5226	27.7638	0	0
L10	88.5282	27.7649	0	0
L11	88.5296	27.7591	0	0
L12	88.5333	27.7605	0	0
L13	88.5465	27.7536	0	0
L14	88.5466	27.7473	0	0
L15	88.5476	27.7431	3	0
L16	88.5501	27.7422	0	0
L17	88.5528	27.7332	0	0
L18	88.5609	27.7274	0	0
L19	88.5595	27.7212	0	0
L20	88.5649	27.7185	0	0
L21R	88.5666	27.7171	0	0
L22	88.5628	27.7128	0	0
L23	88.5625	27.7107	0	0
L24	88.5648	27.7057	0	0
L25	88.5655	27.7047	0	0
L26	88.5667	27.7031	0	0
L27	88.5743	27.6969	0	0
L28	88.5766	27.6951	0	0

L29R	88.5756	27.6941	0	0
L30	88.5852	27.689	0	0
L31	88.5913	27.682	0	0
L32	88.5952	27.6778	0	0
L33	88.6114	27.6386	95	58
L34	88.6125	27.6404	5	1
L35	88.6177	27.6271	94	58
L36	88.6199	27.6273	0	0
L37	88.6203	27.6185	2	0
L38	88.6283	27.6127	0	0
L39	88.6315	27.6113	5	0
L40	88.656	27.583	0	0
L41	88.655	27.5762	0	0
L42	88.6549	27.5563	0	0
L43	88.6295	27.5448	4	0
L44	88.6044	27.5363	0	0
L45	88.4807	27.3426	0	0
Total Post-GLOF landslides = 45;			**Total landslide-impacted buildings = 208**	

Table S2. Road network impacted by triggered landslides. Given are the total length of road network impacted by individual landslides.

Landslide ID	Impacted road by flood-triggered landslides (km)
L43	2.10
L34	1.50
L36	0.88
L12	0.62
L37	0.48
L35	0.35
L38	0.16
L30	0.13
L42	0.12
L39	0.07
Total landslide-impacted road network = 6.41 km	

Table S3: GLOF-induced erosion depths and volume in the first 67.5 km stretch, starting from the SLL to Chungthang.

Distance from SLL	**Maximum Erosion Depth (m)**	**Erosion Volume (m^3) ($\times 10^6$)**
0-5 km	43.61	3.03
5-10 km	26.4	1.79
10-15 km	30.34	2.24
15-20 km	55.18	4.28
20-25 km	27.97	1.54
25-30 km	39.04	3.56
30-35 km	102.96	18.05
35-40km	90.76	22.62
40-45 km	159.0	66.60
45-50 km	96.0	28.20
50-55 km	123.52	10.40
55-60 km	115.06	16.27
60-65 km	126.57	47.77
65-67.5 km	47.27	6.26
		Total eroded volume= 232.61 (m^3) ($\times 10^6$)

5

Table S4. Buildings impacted by the flood cascade mapped from the SLL to 385 km downstream. Also given are the number of buildings impacted by the flood cascade that were constructed in the last decade.

Distance from SLL (km)	Number of flood impacted buildings	Number of flood-impacted buildings constructed in the last decade	Percentage (%) of flood-impacted buildings constructed in the last decade
0 to 40	7	7	100
40 to 80	464	173	37
80 to 120	155	108	70
120 to 160	1612	852	53
160 to 200	356	141	40
200 to 240	3050	2843	93
240 to 280	3468	2741	79
280 to 320	10787	5508	51
320 to 360	2973	1151	39
360 to 385	2992	1670	56
Total	**25864**	**15194**	**59**

Table S5. Flood-inundated agricultural land mapped from SLL to 385 downstream based on pre- and post-flood mapping of agricultural land.

Distance from the SLL (km)	**Inundated agriculture land area (km^2)**
0 to 40	0
40 to 80	1.67
80 to 120	2.49
120 to 160	0.43
160 to 200	1.70
200 to 240	55.17
240 to 280	60.50
280 to 320	88.83
320 to 360	38.32
360 to 385	26.61
	Total = 275.7 km^2

Table S6. Flood-impacted major bridges mapped from SLL to 385 downstream along Teesta River. Given are the bridge ID and their locations.

Bridge ID	Longitude (°E)	Latitude (°N)	Impact
B1	88.3029	27.8781	Damaged
B2	88.3762	27.8807	Damaged
B3	88.5293	27.7612	Damaged
B4	88.5386	27.7567	Damaged
B5	88.5544	27.732	Damaged
B6	88.559	27.7246	Damaged
B7	88.5969	27.6664	Damaged
B8	88.604	27.6591	Damaged
B9	88.6038	27.6563	Damaged
B10	88.6092	27.6422	Damaged
B11	88.6192	27.6267	Damaged
B12	88.6224	27.6181	Damaged
B13	88.6289	27.6137	Damaged
B14	88.6465	27.6017	Damaged
B15	88.6566	27.591	Damaged
B16	88.6542	27.5662	Damaged
B17	88.6448	27.5501	Damaged
B18	88.6436	27.5498	Damaged
B19	88.5809	27.5286	Damaged
B20	88.5418	27.5276	Damaged
B21	88.5265	27.5092	Damaged
B22	88.5239	27.4788	Damaged
B23	88.5156	27.4116	Damaged
B24	88.5157	27.411	Damaged
B25	88.4802	27.3724	Damaged
B26	88.4585	27.2496	Damaged
B27	88.4767	27.2421	Damaged
B28	88.4914	27.2314	Damaged
B29	88.4853	27.2045	Damaged
B30	88.4973	27.1855	Damaged
B31	88.5017	27.1316	Damaged
Total major bridges damaged = 31			

Table S7. Flood-impacted road network mapped from SLL to 385 km downstream.

Distance from SLL	Impacted Road from Lake (m)
0 to 40 km	0
40 to 80 km	5181
80 to 120 km	0
120 to 160 km	6602
160 to 200 km	363
200 to 240 km	0
240 to 280 km	0
280 to 320 km	0
320 to 360 km	0
360 to 385 km	0

Table S8. Mapping aerial extent and length along the northern lateral moraine of SLL from 1975 to 2023.

Year	Date	Area (km^2)	Length along northern lateral moraine (m)	Satellite/Sensor
1975	13-10-1975	0.149	615	Landsat MSS
1988	14-10-1988	0.37118	967	Landsat 5 TM
1991	21-09-1991	0.46241	1040	Landsat 5 TM
1994	15-10-1994	0.53651	1194	Landsat 5 TM
1996	20-10-1996	0.59556	1252	Landsat 5 TM
2000	07-10-2000	0.72342	1547	Landsat 7 ETM+
2004	18-10-2004	0.81243	1624	Landsat 5 TM
2009	16-10-2009	1.08848	1916	Landsat 5 TM
2010	03-10-2010	1.13007	1953	Landsat 5 TM
2013	11-10-2013	1.21963	2313	Landsat 8 OLI
2015	09-10-2015	1.30316	2340	Landsat 8 OLI
2016	17-10-2016	1.36176	2349	Sentinel 2 MSI
2017	17-10-2017	1.41069	2384	Sentinel 2 MSI
2018	10-10-2018	1.45959	2453	Sentinel 2 MSI
2019	10-10-2019	1.49793	2509	Sentinel 2 MSI
2020	09-10-2020	1.54448	2608	Sentinel 2 MSI
2021	11-10-2021	1.58516	2670	Sentinel 2 MSI
2022	14-10-2022	1.66018	2793	Sentinel 2 MSI
2023	14-09-2023	1.6847	2857	Sentinel 2 MSI

Table S9. Correlation of ERA5 and ERA5-LAND with gauge and IMERG. Correlation of ERA5 and ERA5-Land with gauge and IMERG data is presented. Note that the levels of confidence are shown beside each correlation coefficient using the Student's t-test. Coefficients that are significant at the 90% confidence level or above are shown in bold. For calculating correlation over Lachen station, the rainfall time series of ERA5 and ERA5-LAND is a degree area average centered on the grid point nearest to the station. The percentages in parentheses represent the confidence levels calculated using the standard two-tailed Student's t-test. Bold numbers indicate that the confidence level of the correlation is greater than 90%.

Correlation of ERA5 and ERA5-LAND with Gauge and IMERG		**Pearson Correlation**		**Spearman correlation**	
		GAUGE	**IMERG**	**GAUGE**	**IMERG**
LACHEN (SIKKIM)	ERA5	**0.85 (99%)**	**0.57 (95%)**	**0.84 (99%)**	0.47 (85%)
	ERA5-LAND	**0.84 (99%)**	**0.59 (93%)**	**0.84 (99%)**	0.47 (85%)
DALIA (BANGLADESH)	ERA5	**0.75 (99%)**	**0.84 (99%)**	**0.85 (99%)**	**0.75 (99%)**
	ERA5-LAND	**0.74 (99%)**	**0.86 (99%)**	**0.85 (99%)**	**0.75 (99%)**

Table S10. Details of PlanetScope imageries used to study the pre- and post-GLOF dynamics of the northern moraine of SLL.

Scene IDs	Scene Date	Number of scars	Mass movement	Intact Ground
20230101_042140_91_248c_3B, 20230101_042143_23_248c_3B, 20230101_044037_47_2402_3B	1-Jan-23	13	NA	1
20230202_034757_80_245c_3B, 20230304_044103_75_2413_3B	2-Feb-23	12	NA	1
20230304_044103_75_2413_3B	4-Mar-23	12	NA	1
20230602_042955_90_2477_3B,20230625_034833_24_2431_3B	2-Jun-23	12	NA	1
20230625_034833_24_2431_3B, 20230625_034835_35_2431_3B, 20230625_035321_93_24ab_3B	25-Jun-23	12	NA	1
20230815_043340_58_241c_3B	15-Aug-23	12	NA	1
20230902_035656_47_24a9_3B, 20230902_043426_10_2483_3B,	2-Sep-23	11	NA	1
20230927_035600_45_24c8_3B,	27-Sep-23	11	NA	1
20230928_035723_44_242d_3B,20230928_035725_55_242d_3B	28-Sep-23	12	NA	1
20231006_035902_75_24a1_3B	6-Oct-23	NA	12	1
20231007_035705_56_24bf_3B	7-Oct-23	NA	13	1
20231008_035629_65_2415_3B, 20231008_035631_96_2415_3B, 20231008_043623_43_241c_3B	8-Oct-23	NA	8	1
20231009_043258_88_227a_3B, 20231009_043301_00_227a_3B, 20231009_043329_57_24a4_3B	9-Oct-23	NA	9	1
20231011_035316_81_242b_3B, 20231011_035318_89_242b_3B, 20231011_043451_38_2479_3B	11-Oct-23	NA	6	1
20231012_035217_36_2459_3B, 20231012_035219_48_2459_3B	12-Oct-23	NA	6	1

20231013_035402_02_2431_3B, 20231013_035553_73_2439_3B	13-Oct-23	NA	5	1
20231014_035223_83_2442_3B, 20231014_035225_91_2442_3B, 20231014_035551_22_24b5_3B	14-Oct-23	NA	8	1
20231016_035659_54_2439_3B	16-Oct-23	NA	11	1
20231017_035315_07_2442_3B, 20231017_035317_14_2442_3B, 20231017_035712_34_24c8_3B	17-Oct-23	NA	5	1
20231018_035042_11_2460_3B, 20231018_035425_56_2459_3B, 20231018_035427_67_2459_3B	18-Oct-23	NA	17	1
20231019_035529_98_2431_3B, 20231019_035532_06_2431_3B	19-Oct-23	NA	12	1
20231020_035457_15_24bc_3B, 20231020_035459_46_24bc_3B	20-Oct-23	NA	9	1
20231021_043511_92_2473_3B, 20231021_043514_00_2473_3B	21-Oct-23	NA	11	1
20231022_035536_01_24c8_3B, 20231022_043724_17_2475_3B, 20231022_043726_22_2475_3B	22-Oct-23	NA	8	4
20231023_035557_76_24c3_3B, 20231023_035600_06_24c3_3B, 20231023_043614_12_247d_3B	23-Oct-23	NA	7	1
20231024_045754_24_2402_3B, 20231024_045756_07_2402_3B, 20231025_035529_91_2431_3B	24-Oct-23	NA	10	1
20231025_035531_98_2431_3B, 20231026_035332_15_2442_3B	25-Oct-23	NA	9	1
20231026_035334_21_2442_3B, 20231026_043323_51_227a_3B, 20231026_043325_62_227a_3B	26-Oct-23	NA	11	1
20231027_035107_52_2460_3B, 20231027_035109_62_2460_3B, 20231027_043348_24_2488_3B	27-Oct-23	NA	13	1
20231028_035729_51_2439_3B, 20231028_043737_30_2498_3B, 20231028_043739_34_2498_3B	28-Oct-23	NA	9	1
20231029_035253_86_2442_3B, 20231029_035255_92_2442_3B	29-Oct-23	NA	12	1

20231030_035411_16_2459_3B, 20231030_035413_27_2459_3B	30-Oct-23	NA	17	1
20231031_035233_34_2423_3B, 20231031_035624_26_24ba_3B, 20231031_035626_54_24ba_3B	31-Oct-23	NA	14	1
20231102_035717_70_24bb_3B, 20231102_035719_97_24bb_3B	2-Nov-23	NA	13	1
20231103_043349_20_2461_3B, 20231103_043351_28_2461_3B	3-Nov-23	NA	15	1
20231104_035241_32_242b_3B, 20231104_035243_38_242b_3B, 20231104_043630_38_2477_3B	4-Nov-23	NA	14	1
20231105_035138_19_2459_3B, 20231105_035140_29_2459_3B	5-Nov-23	NA	13	1
20231108_035528_25_24b5_3B, 20231108_035530_47_24b5_3B	8-Nov-23	NA	13	1
20231109_035840_86_24c4_3B, 20231109_035843_06_24c4_3B	9-Nov-23	NA	14	1
20231110_043630_61_2446_3B, 20231110_043632_71_2446_3B	10-Nov-23	NA	12	1
20231111_043626_63_247a_3B, 20231111_043628_72_247a_3B, 20231111_043851_97_2484_3B	11-Nov-23	NA	9	1
20231112_035722_98_24c0_3B, 20231112_035725_23_24c0_3B, 20231112_035750_02_242d_3B	12-Nov-23	NA	9	1
20231113_035921_35_24cc_3B	13-Nov-23	NA	9	1
20231115_035914_78_24c9_3B	15-Nov-23	NA	9	1
20231116_035812_66_24b4_3B, 20231116_035814_85_24b4_3B	16-Nov-23	NA	9	1
20231119_044116_70_2446_3B, 20231119_044118_76_2446_3B	19-Nov-23	NA	9	1
20231120_035619_32_24c7_3B,	20-Nov-23	NA	9	1
20231122_040027_34_2429_3B	22-Nov-23	NA	11	1
20231124_043915_23_2495_3B	24-Nov-23	NA	11	1
20231125_040003_06_24cf_3B	25-Nov-23	NA	11	1

20231126_044058_65_2479_3B, 20231126_044100_70_2479	26-Nov-23	NA	11	1
20231127_035956_02_241e_3B, 20231127_043904_90_2495_3B	27-Nov-23	NA	12	1
20231130_044046_65_2473_3B, 20231130_044048_71_2473_3B	30-Nov-23	NA	6	1
20231203_045313_00_24ee_3B, 20231203_045315_31_24ee_3B	3-Dec-23	NA	12	1
20231204_035756_92_24c9_3B, 20231204_035759_09_24c9_3B	4-Dec-23	NA	10	1
20231205_044103_29_2486_3B, 20231205_044105_35_2486_3B	5-Dec-23	NA	8	1
20231206_035903_21_24c2_3B	6-Dec-23	NA	9	1
20231213_035903_47_24ba	13-Dec-23	NA	8	1
20231220_040053_47_24ce_3B	20-Dec-23	NA	9	1
20231222_044223_47_2477_3B, 20231222_044225_51_2477_3B	22-Dec-23	NA	9	1
20231224_044139_14_2475_3B	24-Dec-23	NA	10	1
20231225_043624_19_2424_3B	25-Dec-23	NA	10	1
20231226_040251_00_2465_3B	26-Dec-23	NA	10	1
20231227_035600_60_24a7_3B	27-Dec-23	NA	10	1
20231228_043937_15_2424_3B	28-Dec-23	NA	10	1
20231230_035836_55_24cc_3B, 20231230_035838_77_24cc_3B	30-Dec-23	NA	10	1
20240101_035803_30_2455_3B	1-Jan-24	NA	10	1
20240102_044145_69_24a4_3B	2-Jan-24	NA	10	1
20240103_035806_45_2459_3B	3-Jan-24	NA	10	1
20240105_035824_82_24ba_3B, 20240105_035827_06_24ba_3B	5-Jan-24	NA	10	1
20240106_035806_14_24cf_3B, 20240106_035808_38_24cf_3B	6-Jan-24	NA	10	1
20240107_035839_74_2420_3B, 20240107_044132_17_241c_3B	7-Jan-24	NA	10	1

20240108_035736_32_2415_3B, 20240108_035738_53_2415_3B	8-Jan-24	NA	9	1
20240109_043928_45_2484_3B	9-Jan-24	NA	9	1
20240110_044341_30_247c_3B, 20240110_044343_29_247c_3B	10-Jan-24	NA	9	1
20240111_035722_30_24b4_3B	11-Jan-24	NA	9	1
20240112_045236_56_24d5_3B	12-Jan-24	NA	9	1
20240115_035904_24_24cf_3B	15-Jan-24	NA	9	1
20240117_040017_53_24cc_3B, 20240117_045504_36_24e5_3B	17-Jan-24	NA	9	1
20240118_044414_49_249a_3B, 20240118_044517_76_247b_3B	18-Jan-24	NA	9	1
20240119_040056_29_24a8_3B, 20240119_040058_53_24a8_3B	19-Jan-24	NA	9	1
20240120_035753_53_2415_3B	20-Jan-24	NA	9	1
20240121_044347_28_2473_3B	21-Jan-24	NA	10	1
20240122_035626_27_24c1_3B	22-Jan-24	NA	10	1
20240123_044548_89_247a_3B, 20240123_044550_88_247a_3B	23-Jan-24	NA	10	1
20240125_035649_96_24b6_3B	25-Jan-24	NA	9	1
20240126_035749_28_24cc_3B, 20240126_035751_50_24cc_3B	26-Jan-24	NA	9	1
20240127_035805_79_2459_3B, 20240127_035807_77_2459_3B	27-Jan-24	NA	9	1
20240128_040032_68_24c7_3B, 20240128_040034_91_24c7_3B	28-Jan-24	NA	7	2
20240129_035826_59_24c3_3B, 20240129_044636_25_247b_3B	29-Jan-24	NA	9	1
20240131_044117_40_227a_3B, 20240131_045551_75_24d7_3B	31-Jan-24	NA	9	1
20240201_035934_82_242e_3B	1-Feb-24	NA	10	1
20240202_035702_40_24bf_3B, 20240202_035704_61_24bf_3B	2-Feb-24	NA	10	1
20240203_035734_36_2423_3B	3-Feb-24	NA	6	1

20240204_040113_42_2455_3B, 20240204_040115_39_2455_3B	4-Feb-24	NA	6	1
20240206_044301_31_2488_3B, 20240206_044303_30_2488_3B	6-Feb-24	NA	6	1
20240207_035813_37_24b6_3B, 20240207_044323_69_2438_3B	7-Feb-24	NA	6	1
20240209_035716_68_2459_3B, 20240209_035723_41_24b9_3B	9-Feb-24	NA	6	1
20240210_044614_04_2490_3B	10-Feb-24	NA	6	1
20240211_040441_27_2430_3B, 20240211_044431_68_2486_3B	11-Feb-24	NA	6	1
20240212_045626_38_24f2_3B, 20240212_045628_71_24f2_3B	12-Feb-24	NA	6	1
20240216_040000_17_24c2_3B, 20240216_045654_25_24fb_3B	16-Feb-24	NA	6	1
20240217_035837_71_24bb_3B	17-Feb-24	NA	6	1
20240220_044312_55_2461_3B	20-Feb-24	NA	6	1
20240223_040152_43_24c7_3B	23-Feb-24	NA	6	1
20240224_044642_84_247d_3B	24-Feb-24	NA	6	1
20240225_035905_22_24bb_3B, 20240225_035907_36_24bb_3B	25-Feb-24	NA	6	1
20240226_040840_91_2427_3B	26-Feb-24	NA	6	1
20240227_040630_49_2465_3B	27-Feb-24	NA	6	1
20240228_045350_71_24d3_3B	28-Feb-24	NA	6	1
20240229_044718_39_2498, 20240229_044720_37_2498_3B	29-Feb-24	NA	6	1
20240302_045516_68_24f2_3B	2-Mar-24	NA	6	1
20240305_040248_42_24ab_3B, 20240305_040250_53_24ab_3B, 20240305_045446_16_24e5_3B	5-Mar-24	NA	6	1
20240307_040035_95_24cf_3B, 20240307_040038_09_24cf_3B	7-Mar-24	NA	6	1
20240308_044053_93_227a_3B, 20240308_044055	8-Mar-24	NA	6	1

20240309_044329_58_241c_3B	9-Mar-24	NA	6	1
20240310_040057_26_2459_3B	10-Mar-24	NA	6	1
20240311_040134_35_24a8_3B	11-Mar-24	NA	6	1
20240313_040703_55_2465_3B, 20240313_040705_47_2465_3B	13-Mar-24	NA	6	1
20240316_044939_09_247b_3B	16-Mar-24	NA	6	1
20240317_045533_33_24ee_3B, 20240317_045559_95_24bd_3B	17-Mar-24	NA	6	1
20240318_040949_93_242d_3B, 20240318_040951_84_242d_3B	18-Mar-24	NA	6	1
20240401_040244_96_24c3_3B, 20240401_040247_12_24c3_3B, 20240401_044852_16_247c_3B	1-Apr-24	NA	6	1
20240404_044254_75_227a_3B	4-Apr-24	NA	6	1
20240405_044925_36_2486_3B, 20240405_044927_29_2486_3B	5-Apr-24	NA	6	1
20240406_045308_05_24fb_3B, 20240406_045310_30_24fb_3B	6-Apr-24	NA	6	1
20240408_045130_54_24cd_3B, 20240408_045532_05_24cb_3B	8-Apr-24	NA	7	1
20240409_035923_65_24b6_3B, 20240409_035925_83_24b6_3B	9-Apr-24	NA	7	1
20240411_040149_68_24c5_3B, 20240411_045451_27_24e6_3B	11-Apr-24	NA	7	1
20240414_040015_15_24c2_3B, 20240414_040017_33_24c2_3B	14-Apr-24	NA	7	1
20240415_040348_90_24bc_3B, 20240415_040351_09_24bc_3B	15-Apr-24	NA	7	1
20240417_040420_44_2459_3B, 20240417_045235_56_2498_3B	17-Apr-24	NA	7	1

Table S11. List of high-resolution satellite images and Digital Elevation Models (DEMs) used in the present study. DEMs were created using high-resolution satellite stereopairs.

Pre-event		
Data Source	**Resolution (m)**	**Date**
PlanetScope (4-band multispectral)	3	January 1, 2023 February 2, 2023 March 4, 2023 June 2, 2023 June 25, 2023 August 15, 2023 September 2, 2023 September 5, 2023 September 6, 2023 September 27, 2023 September 28, 2023 September 29, 2023
SkySat -C (4-band multispectral)	0.5 -0.7	January 24, 2023
SPOT 6 stereo-pairs (4-band multispectral)	1.5	December 1, 2018 December 8, 2018
SPOT 6 DEM	4	Created from stereo-pairs
Pléiades stereo-pairs (4-band multispectral)	0.7	October 18, 2022
Pléiades DEM	1	Created from stereo-pairs
Post-GLOF		
PlanetScope (4-band multispectral)	3	6 October 2023 - 17 April 2024
SkySat -C (4-band multispectral)	0.5 -0.7	October 13, 2023
Pléiades stereo-pairs (4-band multispectral)	0.7	October 24, 2023 October 29, 2023 October 31, 2023 November 5, 2023
Pléiades DEM	4	Created from stereo-pairs
Pléiades DEM	1	29 October 2023

Movie S1. Animation showing the reconstructed 3 October 2023 GLOF process chain of SLL, Sikkim, India; the animation is based on our modeling as given in section 4; Blue represents water and red shows the moraine material of the lake. All model codes and the data are made available using the Zenodo repository (*129*) (see data availability).